THE ROLE OF SOMATOSTATIN-EXPRESSING INTERNEURONS IN ANTERIOR PIRIFORM CORTEX

by

Adam M. Large

A.B. in Biology, University of Chicago, 2011

Submitted to the Graduate Faculty of the

Kenneth P. Dietrich School of Arts and Sciences in partial fulfillment

of the requirements for the degree of

Doctor of Philosophy

University of Pittsburgh

2017

UNIVERSITY OF PITTSBURGH

Dietrich School of Arts and Sciences

This dissertation was presented

by

Adam M. Large

It was defended on

April 7, 2017

and approved by

Dr. German Barrionuevo, Professor, Department of Neuroscience, University of Pittsburgh

Dr. Brent Doiron, Associate Professor, Department of Mathematics, University of Pittsburgh

Dr. Yan Dong, Professor, Department of Neuroscience, University of Pittsburgh

Dr. Sandra J. Kuhlman, Assistant Professor, Department of Biological Sciences, Carnegie Mellon University

Dr. Anne-Marie M. Oswald, Assistant Professor, Department of Neuroscience, University of Pittsburgh

Dr. Donald Wilson, Professor, Department of Child and Adolescent Psychiatry, Department of Neuroscience and Physiology, New York University

Dissertation Advisor: Dr. Nathaniel Urban, Professor and Vice Chair, Department of Neurobiology, University of Pittsburgh

THE ROLE OF SOMATOSTATIN-EXPRESSING INTERNEURONS IN ANTERIOR PIRIFORM CORTEX

Adam M. Large, PhD

University of Pittsburgh, 2017

At first approximation, the anterior piriform cortex (APC) appears to be a homogenous structure in terms of connectivity and sensory processing. Feedforward excitatory afferent input innervates the APC uniformly throughout the cortex, as does the local recurrent excitatory input. Odors are represented by a distributed ensemble of neurons spread throughout the APC, showing no obvious columnar structure or topography. Still, this supposed homogeneity belies the abundant diversity of inhibitory processes that may underlie sensory processing of the piriform cortex. Unfortunately, current understanding of inhibitory interneurons and their function is fairly coarse, limiting our ability to model olfactory processing. Our research was focused on clarifying the quality of inhibition in anterior piriform cortex, specifically focusing on Layer 3 somatostatin-expressing interneurons, which mediate recurrent, feedback inhibition. We first characterized the types of inhibition seen in the APC and their potential functions. Using electrical stimulation of APC fiber tracts, we measured the relative balance of feedforward and recurrent excitation and inhibition onto the three major classes of excitatory cells in piriform cortex to understand the relative roles for each type of input onto piriform principal cells. Then, we characterized the electrophysiological and functional properties of interneurons in APC, including somatostatin cells, to better understand the diversity of cells in olfactory cortex. Finally, we were interested in the role of inhibition in mediating principal cell activity. To do

this, we used a novel technology - Targeted Recombination of Active Populations (TRAP) - to molecularly label active neurons during exploration of a novel odor environment. We found that neurons responding to an odor are not distributed uniformly across the APC, but rather on a gradient along the rostrocaudal axis. Using optogenetics, we found a spatial bias of inhibition onto pyramidal cells that corroborated the TRAP data, as well as discovering a subclass of interneurons that receive an opposing rostrocaudal bias of inhibition - suggesting a possible role for disinhibition in sensory processing. We determined that somatostatin cells are poised to mediate asymmetric inhibition onto interneurons, and therefore asymmetric disinhibition onto pyramidal cells.

TABLE OF CONTENTS

LIST OF TABLES

LIST OF FIGURES

PREFACE

This thesis is the summation of years of work at the University of Pittsburgh Center for Neuroscience, and it reflects not only my own personal effort, but that of the community which supported me. I have the deepest gratitude for the CNUP in believing in my potential and providing me with the resources to succeed. Furthermore, the Center for the Neural Basis of Cognition has been instrumental in providing me with amazing opportunities to further my professional goals. Finally, I must thank the Achievement Rewards for College Scientists (ARCS) Foundation for the financial support during my early graduate career.

Of course, there are many individuals to thank for all of their hard work during this period. First and foremost, would be my advisor, Dr. Anne-Marie Oswald, who took a chance on a neophyte like myself, and train me in the skills necessary to be a neuroscientist.

I also thank my committee members, both past and present – including Drs. Carl Olson, Matt Smith, Marlene Cohen, Nathan Urban, German Barrioneuvo, Susan Sesack, Alison Barth, Sandy Kuhlman, Brent Doiron, and Yan Dong, as well as Dr. Donald Wilson for being my outside examiner.

And finally, I must thank my friends and family for their patience and support over the ·t six years – without which none of this would have been possible.

1.0 INTRODUCTION

As the name implies, the olfactory cortex is the region of the brain that processes olfactory information. The olfactory cortex is part of the paleocortex, a phylogenetically old region with cytoarchitecture that differs from that of neocortex. Despite this, or perhaps due to this, the basic circuitry in olfactory cortex has been seen in other, newer, brain regions. There are actually several different brain structures the make up the olfactory cortex, including the piriform cortex, anterior olfactory nucleus, and portions of the amygdala and entorhinal cortex (Neville KR and Haberly L 2004). Here, we explore the circuitry of one such region of the olfactory cortex: the piriform cortex. Specifically, we are interested in understanding the structure of the anterior piriform cortex, in hopes that it may guide our understanding of the relationship between circuitry and function.

1.1 INTRODUCTION TO NEURAL CIRCUITRY

A brain has little use for a single, solitary neuron. While an individual neuron can serve as a processing unit in itself - taking inputs and producing an output - without other neurons, it can only serve as a middle man between a sensory organ and a motor unit. What provides the brain with its unfathomably broad scope is how it organizes neurons into complex processing units. There are several possible ways neurons can influence one another. A very basic dichotomy

exists between neurons that upregulate the activity of other neurons, referred to as excitatory neurons, and neurons that downregulate the activity of other neurons, referred to as inhibitory neurons. Of course, neurons can have more subtle effects on each other, and we will discuss some of these as they come up. For purposes of our research, we will focus on comparisons between the piriform cortex and other sensory cortices. Even so, this basic distinction groups neurons along anatomical, morphological, and electrophysiological lines. Excitatory neurons in the cortex express glutamate, whereas inhibitory neurons express GABA. Projection neurons – those that send their axons to other brain regions, are often excitatory. Inhibitory neurons, meanwhile, are often classified as interneurons – they target other neurons within their cortex of residence.

1.1.1 Mechanisms of Inhibition

In the nervous system, inhibition of neurons can be accomplished by various means. There are many neurotransmitters that could be said to have inhibitory effects, but the primary inhibitory neurotransmitter in the cerebral cortex is GABA. Even with this single neurotransmitter, there are several ways for GABA to interfere neural activity. Generally, inhibition can be construed as any means by which a neuron is less inclined to fire an action potential. How that is accomplished can take many forms, which take advantage of the different aspects of neuronal electrophysiology. For example, neuronal inhibition can be accomplished by directly manipulating the voltage of the postsynaptic neuron, hyperpolarizing it and keeping it from reaching threshold. Neurons are also inhibited through shunting mechanisms, whereby the channel openings cause the synaptic reversal potential falls below threshold, preventing enough excitatory current to pass through the neuron and cause action potential generation. Importantly,

shunting inhibition could be depolarizing or hyperpolarizing, depending on the synaptic reversal potential. GABAA receptors, as ligand-gated chloride channels, fall into the hyperpolarizing/shunting camp. Activating of GABAA receptors causes an influx of chloride ions, which can either hyperpolarize or depolarize the postsynaptic neuron, depending on the reversal potential for chloride and the resting membrane potential of the postsynaptic cell. The channel "shunts" currents by way of locally reducing the membrane resistance, severely mitigating the size of nearby excitatory post-synaptic potentials. Additionally, inhibition could take the form of the manipulation of cellular machinery, such as interfering with presynaptic calcium channels, preventing the release of neurotransmitters. This would be the mechanism by which the metabotropic GABAB receptor affects neurons.

It is also important to consider where on a neuron inhibition is taking place. While inhibitory neurotransmitters may appear to fulfill the same function on a receptor-level view, where that receptor or synapse is on the neuron is incredibly important. As hinted at previously, GABA-mediated inhibition can be presynaptic, by way of GABAB receptors, or postsynaptic, through GABAA receptors. More than that, we must also remember than neurons are composed of a cell body (soma) with an input structure (dendrites) and output structure (axon), and that the location of inhibition on each of these areas can have functional significance (Miles et al. 1996; C. C. Stokes and Isaacson 2010). Perisomatic inhibition and inhibition that targets the axon initial segment are often seen to prevent action potential output, whereas dendrite-targeting inhibition dendrites is seen to be relevant in diminishing excitatory inputs (Sturgill and Isaacson 2015). Moreover, keeping the dendritic membrane potential hyperpolarized would help prevent the possibility of dendritic spiking (Leung and Peloquin 2006; C. C. A. Stokes, Teeter, and

Isaacson 2014) and would play a role in regulating spike-timing dependent plasticity (Bar-Ilan, Gidon, and Segev 2013).

So far, we have only discussed inhibition at the level of a single synapse between two neurons. But if we expand our scope to a collection of neurons in a circuit, we will be able to see the impressive diversity of functions interneurons can play in a cortical circuit. While one can assemble several complicated circuits by rearranging the basic components of excitatory and inhibitory neurons, there are four motifs we will mention now: feedforward inhibition, feedback inhibition, lateral inhibition, and disinhibition (Shepherd 2004). Of course, this list is not exhaustive nor mutually exclusive. Feedforward inhibition occurs when incoming exogenous excitatory (afferent) input synapses onto interneurons, which then synapses onto a pyramidal cell. When the afferent input also contacts the target cell, the feedforward inhibition, which delayed by an additional synapse, provides a brake on the activity of the pyramidal cell, allowing for tight temporal precision of pyramidal cell output (Buzsáki 1984). Feedback inhibition is when the inhibitory interneuron does not receive afferent input, but rather input from the pyramidal cell it targets. Here, the neurons are co-modulated, the pyramidal cell activity indirectly dampens itself. In this document, we will often refer to feedback inhibition as recurrent inhibition. Lateral inhibition, on the other hand, exists when the pyramidal cell targets interneurons that target other neighboring pyramidal cells, providing a sort of electrical competition between pyramidal cells. There are numerous implications for this circuit (Markram et al. 2004; Giridhar, Doiron, and Urban 2011; Valley and Firestein 2008; D. A. Wilson and Leon 1987; Isaacson and Scanziani 2011), but in our research, we primarily focus on feedforward and feedback inhibition as these motifs are well-established in the piriform cortex and are conceptually easier to generate hypotheses for. There is one final motif we can mention, and that is of disinhibition.

Disinhibition exists when interneurons target interneurons, providing relief of inhibition on downstream pyramidal cells. It is important to keep in mind is that it would be glib to consider the role of inhibition to be the prevention of action potentials. A more nuanced take would be that inhibition exists to dictate when actions potentials can occur in the first place. Disinhibition may prove to be very relevant in neural circuits, as it provides and "off switch" to inhibition, allowing for pyramidal cells to respond to incoming input (Ibrahim et al. 2016; Karnani et al. 2016; Xu et al. 2013; S. Lee et al. 2013; Muñoz et al. 2017) and thus may also play a role in plasticity (Yu Fu et al. 2015; Letzkus, Wolff, and Lüthi 2015). It is interesting to note that the first three circuit motifs describe where excitatory input is coming onto interneurons, whereas disinhibition is interested in where inhibitory input is coming onto interneurons. What may be causing disinhibitory circuitry to come online is a topic we will return to in our discussion.

1.1.2 Interneuron Diversity

Inhibitory neurons comprise about 10-20% of cortical neurons, but have a great deal of diversity within the group. Interneurons can be classified by electrophysiology, morphology, expression profile, and functional role (Kawaguchi and Kubota 1997; Y. Kubota and Kawaguchi 1994; Ascoli et al. 2008). And despite being a small proportion of cells in the brain, they are critical for regulating the activity of projection neurons, modulating the gain and timing of action potentials (Markram et al. 2004). A common method to characterize interneurons is by dividing them up based on the molecular expression profile (Y. Kubota and Kawaguchi 1994; Yoshiyuki Kubota et al. 2011; Yoshiyuki Kubota 2014). These include the calcium binding proteins parvalbumin (PV), calbindin (CB), calretinin (CR), along with neuromodulators such as somatostatin (SST),

vasoactive intestinal peptide (VIP), neuropeptide Y (NPY), cholecystokinin (CCK) (Y. Kubota and Kawaguchi 1994; Yoshiyuki Kubota et al. 2011; Markram et al. 2004; Ascoli et al. 2008).

1.1.3 Parvalbumin Interneurons

Parvalbumin-expressing (PV) interneurons have been one of the most studied interneuron cell types in neuroscience. This is partially due to them being the largest subpopulation of GABAergic cells in the neocortex, comprising about 40-50% of all inhibitory neurons (Rudy et al. 2011). They are also easily identified by their characteristic fast-spiking phenotype as well as the existence of robust antibodies to the parvalbumin protein (Hua Hu, Gan, and Jonas 2014). These cells are characterized by the expression of parvalbumin, a calcium binding protein. PV cells have an extremely characteristic electrophysiology: narrow action potentials and the ability to produce many action potentials in a short time period – they are fast-spiking (FS) interneurons.

While PV cells may have different morphologies across the nervous system, they do share some commonalities. PV cell dendrites sample a wide area, allowing them to sample input from several excitatory cells. PV cell axons target postsynaptic cells perisomatically. In the cortex, parvalbumin cells are often known as basket cells, named for their axonal arborizations that wrap around target soma, given them a basket-like appearance. Because PV cells target the soma of postsynaptic neurons, they are suited to produce strong inhibition that can quickly quench action potential generation.

There have been a couple of transgenic mouse lines developed to study PV cells. A common transgenic mouse line is the G42 line. This utilizes a GAD67-GFP artificial chromosome which was designed to insert into the mouse genome through homologous recombination. Due to random insertion of the genetic construct in the genome, the expression

of GAD67 is dependent on the local transcription environment. These mice express GFP exclusively in PV cells, although the label only about half of all PV cells (Chattopadhyaya et al. 2004). The other common method for genetically labeling PV cells is the use of PV-Cre mouse line. This has the benefit of breeding the mouse with a reporter gene of interest, whether it be GFP, RFP, channelrhodopsin, or whatever the experiment needs (Madisen et al. 2012). Thankfully, the PV-Cre mouse line does not seem to have too much off-target labeling of other cell types (Nassar et al. 2015).

1.1.4 Somatostatin Interneurons

Somatostatin-expressing interneurons comprise about 20-30% of GABAergic neuron in the neocortex (Rudy et al. 2011). Somatostatin (SST) interneurons are characterized by their expression of their namesake neuropeptide. However, despite this common trait, they are far from being a homogenous class of interneurons. SOM cells display a diversity of morphologies, electrophysiologies, laminar distributions, synaptic inputs and outputs, as well as they can co-express several other molecular markers.

Somatostatin cells have canonically been described as targeting the dendrites of excitatory cells (Fino and Yuste 2011; Pfeffer et al. 2013), where they play a role in diminishing the incoming input to pyramidal cells and preventing calcium spikes and burst firing of pyramidal cells (Chiu et al. 2013; Marlin and Carter 2014; S. X. Chen et al. 2015). Therefore, somatostatin cells are at the crux of a neural circuit for modulating the gain of pyramidal cell firing in response to afferent input. Moreover, there is evidence of SST cells modulating pyramidal cell output through presynaptic GABAB receptors (Urban-Ciecko, Fanselow, and Barth 2015). Somatostatin interneurons have also been shown to target parvalbumin cells

(Pfeffer et al. 2013), meaning that they can contribute to disinhibitory circuitry as well. The one cell type that SST cells do not seem to target are other SST cells (Pfeffer et al. 2013). SST cells seem to be contributing to neural circuitry in a number of possible ways. However, given the that there are many SST cell subtypes, it is possible that not every SST cell fulfills every role.

While characterizing SST cells by way of physical properties is useful in classifying the diversity of possible subtypes, it has been shown to be useful to leverage the genetic technologies found in mouse models. To that end, transgenic mouse lines have developed. Historically, the most common lines were a set of GAD67-eGFP mice: GIN, X94, X98 (Y. Ma et al. 2006; Nassar et al. 2015). These mice were designed in a similar way to the G42 line mentioned above. A subset of these GAD67-eGFP mice conveniently labeled somatostatin interneurons, although the three mouse lines label different subsets of somatostatin cells. Of these three mouse lines, GIN is probably the most studied, as it primarily labels the well-characterized Martinotti cell type. In the neocortex, Martinotti cells are mostly found in layers 2/3 and feature a regular-spiking phenotype, and send their axons into layer 1 (Y. Ma et al. 2006). However, GIN cells only make up about 35% of all SOM cells.

X94 cells, by contrast, do not label Martinotti cells, instead labelling about half of the SOM cells in layer 4 and feature a more local axonal projection pattern that targets Parvalbumin-positive cells. Moreover, X94 cells demonstrate a stuttering, fast-spiking firing property whereby they have narrow action potentials with periods of silence interspersed with periods of low inter-spike intervals (Y. Ma et al. 2006; Xu et al. 2013). They have been shown to provide inhibition to nearby PV cells and excitatory cells.

On the other hand, X98 cells also label Martinotti cells, though primarily in layers 5/6, where they send axons to layer 4, and make up about 20% of all SOM cells. X98 cells are known

for their low-threshold spiking properties, which features a rebound spike after being held at a hyperpolarized holding potential (Y. Ma et al. 2006).

In order to capture a broad range of SST cells, the SST-cre mouse line was developed (Taniguchi et al. 2011). Like the PV-cre mouse line, this line can be crossed with any LoxP-reporter gene of interest. However, unlike the PV-cre mouse line, SST-cre lines seem to have a slight issue with off-target recombination (Nassar et al. 2015; Hang Hu, Cavendish, and Agmon 2013).

1.2 STRUCTURE OF THE PIRIFORM CORTEX

1.2.1 Anatomy of the Piriform Cortex

In the mouse brain, the piriform cortex can be identified by its association with the lateral olfactory tract (LOT), which is the bundle of myelinated axon fibers arriving from the olfactory bulb, serving as the feedforward afferent input to the piriform cortex. While olfactory bulb mitral cells send their axons throughout the piriform cortex, the lateral olfactory tract is only identifiable as an anatomical structure for about half of the length of the piriform. The point at which the LOT is no longer visible is considered to be the dividing line between anterior and posterior piriform cortex (APC and PPC) (Ekstrand et al. 2001). The posterior piriform cortex still receives olfactory bulb input, but it is dwarfed by the extensive intracortical from olfactory cortical areas. The anterior piriform can be further divided into a dorsal and ventral portion. These are not simply anatomical distinctions, but rather functional subdivisions of the cortex. For example, while the olfactory bulb output cells include both mitral and tufted cells, tufted cells

project only to the ventral portion of the APC (as well as the anterior olfactory nucleus), but not to the dorsal APC or the PPC. Mitral cells, by comparison project to all three subdivisions of the piriform cortex (Lewis B. Haberly and Price 1977; Luskin and Price 1982; Scott 1981). This may be relevant, as tufted cells show shorter onset response latency across a range of odor concentrations (Igarashi et al. 2012). However, the specifics of this distinction are beyond the scope of our research here. The subdivisions of piriform cortex are also relevant for their projections to downstream brain regions. While the APC projects to higher order brain structures, the two divisions of APC form parallel pathways (Ekstrand et al. 2001). Ventral APC pyramidal cells project to the submedius nucleus of the thalamus and ventrolateral orbital cortex, whereas dorsal APC pyramidal cells project to the mediodorsal nucleus of the thalamus, the lateral orbital cortex and agranular insula.

1.2.2 Laminar Architecture of Anterior Piriform Cortex

The piriform cortex is a trilaminar cortex with a highly stereotyped architecture. The three layers are comprised of: a fiber tract layer (layer 1) and two cell body layers (layers 2 and 3). A summary of the laminar architecture can be found in Figure 1. Layer 1 (L1) is comprised of dendrites, axon fibers, and a few interneurons. It can be divided into two sublayers: Layer 1a (L1a), which contains the incoming axons of olfactory bulb M/T cells that form the LOT, and Layer 1b (L1b), which carries intracortical fibers from local neurons as well as intercortical projections from other brain structures (Price 1973). While most neurons are in layers 2 and 3, layer 1b does contain neurogliaform and horizontal interneurons. These cells receive direct LOT input and, as such, provide feed-forward inhibition onto principle neurons. Principle neurons in

the piriform cortex include excitatory pyramidal and semilunar cells. Semilunar cells are located in superficial sections of layer 2, while pyramidal cells can be found in layer 2 (superficial pyramidal cells) and layer 3 (deep pyramidal cells) (Lewis B. Haberly and Price 1978). Pyramidal cells in L2/3 send their apical dendrites to layer 1 to receive both afferent input as well as intracortical excitation. These pyramidal cell axons contact not only other pyramidal cells, but also other interneurons in order to recruit recurrent inhibition from SST and PV cells (Lewis B. Haberly and Price 1978; Suzuki and Bekkers 2010b, 2010a, 2012).

Both cell body layers are also home to a variety of interneurons. Layer 2 (L2) is predominately home to bitufted cells, but also features neurogliaform cells and interneurons mediating feedback inhibition (Ekstrand et al. 2001; Suzuki and Bekkers 2010b, 2010a; Donald A. Wilson and Sullivan 2011). Layer 3 (L3) contains multipolar cell that can exhibit fast-spiking or regular-spiking phenotypes (Ekstrand et al. 2001; Suzuki and Bekkers 2010b, 2010a). Whereas layer 1 interneurons receive projections in layer 1a, the dendrites of layer 2 and 3 interneurons typically do not reach the afferent fiber layer, and primarily receive input from association fibers in layer 1b. Because they gain input from recurrent excitatory activity, they primarily mediate feedback inhibition.

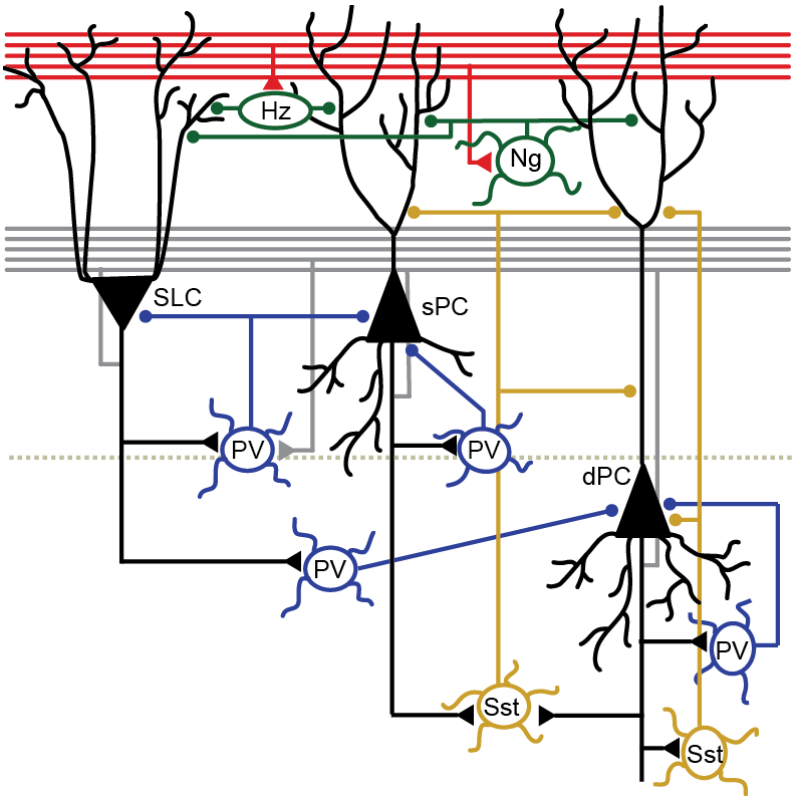

Figure 1. Consensus Circuit Diagram of Piriform Cortex.

Summary of cell types in piriform cortex, highlighting their laminar location, the inputs to each cell type, as well as their outputs. Circle synapses are inhibitory. Triangle synapses are excitatory. Hz: Horizontal cell. Ng: neurogliaform cell. SLC: Semilunar cell. sPC: superficial pyramidal cell. dPC: deep pyramidal cell. VIP: VIP-expressing interneuron. PV: parvalbumin-expressing interneuron. SST: somatostatin-expressing interneuron. FB: feedback interneuron. Adapted from (Donald A. Wilson and Sullivan 2011).

1.2.3 Interneuron Diversity

There are several different subtypes of interneurons in piriform cortex (Ekstrand et al. 2001; Suzuki and Bekkers 2010b, 2010a). These subtypes can be categorized based on molecular markers, such as calcium-binding proteins or neuropeptides, as well as their morphology and

electrophysiology. Layer 1 interneurons are predominantly horizontal or neurogliaform in morphology. They receiving direct projections from the olfactory bulb and mediate feedforward inhibition. Layer 2 is home to the bipolar interneurons, which express vasoactive intestinal peptide (VIP) as well as calretinin (CR). While not much research has been taken into VIP interneurons in piriform cortex, recently they have become of great interest to researchers in other cortical systems, as they primarily target other interneurons. The interneurons that reside in Layer 3 are fairly heterogenous. There exist a small number (bout 5% of interneurons of VIP/CR cells in layer 3 (Suzuki and Bekkers 2010a), but most of the cells in L3 are multipolar in appearance (Suzuki and Bekkers 2010a; Young and Sun 2009). These can be subdivided into the fast-spiking (FS) cells, which express Parvalbumin (PV) and Calbindin (CB), and often both. These cells target pyramidal cell somas and receive recurrent excitatory drive thus providing feedback inhibition. CB cells comprise about 40% of the interneurons in layer 3 of the APC, and PV cells are about 15% of the interneurons in layer (Suzuki and Bekkers 2010a). The other multipolar cell class express somatostatin (SST), which also provides feedback inhibition via input from recurrent excitation, but targets the dendrites of pyramidal cells. Somatostatin cells comprise about 30% of interneurons in piriform cortex (Suzuki and Bekkers 2010a). A subset of SST cells express calbindin as well (Suzuki and Bekkers 2010a). They send their axons in L1B to target pyramidal cells (Suzuki and Bekkers 2010b, 2010a), likely through dendritic inhibition. SST cells have been shown to narrow odor tuning curves via subtractive inhibition (Sturgill and Isaacson 2015), which would be appropriate, given that dendritic inhibition is would modulate the processing of incoming afferent input.

While the role of interneurons in neural circuits is of great interest, most of the research on the topic has been in neocortex (Oliva et al. 2000; Cabezas et al. 2013; Nassar et al. 2015).

Whether the characterizations of interneurons described in Section 1.1 are similar in the APC needs further research.

1.2.4 Spatial Properties of the Piriform Cortex

Unlike other primary sensory cortices, the anterior piriform cortex has no obvious columnar structure. Afferent input to the piriform cortex is homogenously distributed (Igarashi et al. 2012) and recurrent excitatory connections seem to be uniform across the cortex (Franks et al. 2011). The piriform is also characterized by broadly tuned global inhibition, and sparse, spatially distributed coding (Poo and Isaacson 2009; Stettler and Axel 2009).

It has been well-established that the olfactory bulb encodes olfactory stimuli in a spatial code, wherein a given odorant activates a stereotyped and predictable set of glomeruli across animals (Soucy et al. 2009; L. Ma et al. 2012). This spatial patterning is lost in the piriform cortex, however. The projections from a given glomerulus to the piriform cortex has been shown to be homogenous (Igarashi et al. 2012), resulting in a uniform pattern of activity in the APC, regardless of the stimulus identity. Furthermore, the targets of these projections are seemingly random – to a first approximation there is no apparent topology between glomerular activation and piriform principal cell innervation. Therefore, unlike the olfactory bulb, it is impossible to determine, based on the spatial activity pattern alone, what stimulus was presented to the animal.

Nonetheless, there is evidence that the APC has some spatial organization. Considering the size of the mouse piriform cortex, it would be surprising to see a total lack of functional subdivisions. There is so evidence that the rostrocaudal axis of the APC may be useful in stimulus representation (Sugai et al. 2005). Intrinsic signal imaging has suggested that the concentration of an odor may be represented in the APC; rostral portions of APC have a lower

odor concentration threshold than caudal portions of APC. This effectively produces a topographic map of stimulus concentration receptive fields. Ex vivo slice recordings seem to support the intrinsic signal imaging: Glutamate uncaging experiments show an increasing gradient of inhibition onto pyramidal cells along the rostrocaudal axis of the APC (Luna and Pettit 2010). Stronger afferent activity would generally be required to overcome stronger local inhibition.

An alternative, albeit not mutually exclusive, possibility is the appearance of distinct subdivisions of APC based on their projection targets. Using viral track tracing and immunohistochemistry, it seems that rostral and caudal APC do have different downstream targets (Padmanabhan et al. 2016; C.-F. F. Chen et al. 2014). Recent evidence has shown that feedback projections back to the olfactory bulb gradually decrease along the rostrocaudal axis of the APC (Padmanabhan et al. 2016). Moreover, feedforward projections are also anatomically segregated. More rostral APC neurons generally target the orbitofrontal cortex, while caudal APC neurons generally target the agranular insula (C.-F. F. Chen et al. 2014). There has even been some work in finding molecular signatures for subpopulations of piriform neurons that project to different downstream areas (Diodato et al. 2016).

1.3 SENSORY PROCESSING IN THE PIRIFORM CORTEX

1.3.1 Feedforward input from the olfactory bulb

The olfactory bulb receives sensory input from olfactory sensory neurons in the olfactory epithelium, inside the nasal cavity. Olfactory receptor neurons are remarkable in that they each

only express a particular olfactory receptor, out of the 1400 olfactory receptor genes in the mouse genome. While each olfactory receptor is a member of a GPCR family, they can vary in the structure of their binding site, altering their affinity for different odor molecules. Olfactory receptor neurons project their axons to the glomeruli, spatially segregated regions of dense neuropil, of the olfactory bulb. Glomeruli are where the axons of the olfactory receptor neurons and the dendrites of the mitral and tufted cells meet. Olfactory receptor neurons that express the same olfactory receptor project to the same glomerulus in the ipsilateral olfactory bulb (Vassar et al. 1994; Mombaerts et al. 1996; Ressler, Sullivan, and Buck 1994). Because each glomerulus represents one and only one olfactory receptor, this creates an anatomical coding scheme, also known as a labeled line code, whereby a stimulus can be decoded based on observing which glomeruli are active during the stimulus presentation. In mice, the locations of glomeruli are anatomically stereotyped, providing an anatomical code that is conserved across animals (Soucy et al. 2009; L. Ma et al. 2012). This would mean that a stimulus that generates a pattern of glomerular activity in one mouse would result in the same pattern of glomerular activity in another mouse.

Mitral and tufted cells of the olfactory bulb then project their axons into the olfactory cortex. To the best of our abilities, these projections are seemingly homogenous across the piriform cortex (Igarashi et al. 2012). That the afferent input to the piriform cortex is uniform – a rostral APC pyramidal cell is as likely to receive input from a given mitral cell as a caudal APC pyramidal cell would. The functional purpose of switching from a labeled line code to a distributed code has been the subject of much discussion (Miura, Mainen, and Uchida 2012; Illig and Haberly 2003; Donald A. Wilson and Sullivan 2011).

1.3.2 Representation of stimuli through a distributed population code

One of the major challenges in neuroscience is in understanding the mapping between neural activity and thought. Rather than trying to study such an abstract relationship, many have taken to studying how neurons may represent sensory stimuli. Seeing that sensory stimuli can be manipulated in the physical world; it allows the researcher to control one side of this mapping while studying the other. It has been well-established that neurons respond to stimuli through a change in membrane voltage, which often results in the firing of action potentials, also known as "spikes." Neurons can produce a series of spikes with characteristic shapes, timing, and patterns, and neuroscience research is currently focused on the relevant parameters of spike properties in relation to the representation of a stimulus. To make matters difficult, there are many possible way neurons may encode a stimulus, and different cortical areas may be using different coding schemes for different stimuli. One dimension to neural encoding stems from the amount of action potentials produces. Rate coding schemes are specifically interested in the average number of spikes within a time window, irrespective of their pattern. Conversely, temporal coding may exist when the precise spike timing is relevant for the neuron. Along with the temporal properties of action potentials, the spatial properties may also be very relevant. Many cortical areas are thought to represent stimuli through a population code, whereby a stimulus is represented by the relative degree of activity of each neuron in a population. This has been shown to be a coding scheme in the medial temporal cortex, which responds to movement direction. On the other hand, one may see a sparse coding scheme, whereby a stimulus is represented by a strong response in a subset of neurons. In an extreme case of sparse coding, you have such phenomena as "grandmother" cells, with a specific neuron that responds exclusively to an image of the viewer's grandmother.

Sparse coding is of interest in models of memory, where is associated with the idea of neural ensembles or assemblies. Sparse coding schemes would leverage a population of neurons to magnify memory storage (Földiak 2002; Wixted et al. 2014; Olshausen and Field 2004; Miura, Mainen, and Uchida 2012). In contrast to population codes, a sparse coding scheme would allow a stimulus to be represented by only a small fraction of possible neurons and any given neuron would respond to only a few stimuli. This is further leveraged by associative learning mechanisms. Strengthening connections between neurons that represent a particular stimulus would produce a neural assembly, with neurons in that assembly co-firing to that stimulus. A given neuron may be part of more than one assembly, improving memory capacity – although the number of assemblies a neuron belongs in is likely to be somewhat low. Neural assemblies have an additional benefit beyond increasing memory capacity. Given that neurons within an assembly have stronger connectivity than the average connection strength in the area, when the subject is presented with a weak or degraded version of a stimulus, a portion of the assembly will be active and bring up the activity of the rest of the assembly (Donald A. Wilson 2009).

The piriform cortex, as part of the olfactory cortex, is proposed to be responsible for the encoding, storage, and retrieval of odor memories. Unlike most primary sensory cortices, which feature a topographic, columnar architecture, odor information in the piriform cortex is encoded as a distributed network of neuronal activity. It has been proposed that in lieu of a topographic code, piriform cortex utilizes a precise, sparse spatiotemporal code in order to represent stimuli (Poo and Isaacson 2009), much like other association cortices such as the hippocampus and the inferotemporal cortex (Donald A. Wilson and Sullivan 2011; Donald A. Wilson and Rennaker 2010). In piriform cortex, individual odors activate specific subsets of neurons, known as odor

assemblies. Repeated odor experiences help shape and refine the assembly, forming an exclusive collection of neurons that represents that odor (Poo and Isaacson 2009; Choi et al. 2011; Shakhawat, Harley, and Yuan 2014). It is hypothesized that plasticity leads to strong connections between neurons within an odor assembly (Neville KR and Haberly L 2004; L. B. Haberly and Bower 1989). These strong connections allow the assembly to be reactivated and the odor "memory" to be recalled even when the odor is degraded or encountered in a different context. Piriform principal cells have complex receptive fields (Donald A. Wilson 2001) that respond to a complex combination of glomerular activity and features strong recurrent circuitry (Isaacson and Scanziani 2011). The two main objectives of the piriform cortex are pattern completion – recognizing a learned odor from a degraded or noisy input – and pattern separation – distinguishing two overlapping odors (Chapuis and Wilson 2012). The structure of the piriform cortex is well-equipped to handle these tasks. Because of its extensive intrinsic connectivity between principle neurons, pattern completion can be accomplished when a large enough portion of the neural assembly is activated by a degraded or noisy input. Along the same lines, the piriform cortex is capable of performing pattern separation by use of maintaining distinct neural assemblies for odors.

2.0 BALANCED FEEDFORWARD INHIBITION AND DOMINANT RECURRENT INHIBITION IN OLFACTORY CORTEX.

2.1 INTRODUCTION

The recruitment of inhibition is an essential feature of cortical processing. Feedforward and recurrent inhibitory circuits have been implicated in controlling the timing, strength and tuning of cortical responses (for review see (Isaacson and Scanziani 2011)). In sensory cortices, including olfactory cortex, neural responses to sensory stimuli depend on the relative balance of inhibition with respect to excitation in both feedforward and recurrent pathways (Gabernet et al. 2005; Poo and Isaacson 2009, 2011; Schummers, Sharma, and Sur 2005; Yang et al. 2013; Y. Zhao et al. 2015). Moreover, numerous theoretical studies have suggested that balanced cortical networks underlie the selectivity, sparseness and correlations of cortical activity (Graupner and Reyes 2013; Hansel and Vreeswijk 2012; Litwin-Kumar and Doiron 2012; Litwin-Kumar et al. 2011; Murphy and Miller 2009; Ozeki et al. 2009; Pehlevan and Sompolinsky 2014; Rubin, Van Hooser, and Miller 2015). These studies highlight the importance of quantifying the relationship between excitation and inhibition in cortical networks. However, isolating the contributions of feedforward versus recurrently evoked inhibition to cortical responses is difficult because these circuits are often co-active and frequently share interneurons (Neske, Patrick, and Connors 2015; Porter et al. 1999; Swadlow 2003). The piriform cortex is an ideal system to address this issue because the interneurons responsible for feedforward and recurrent inhibition differ by class and laminar location and thus, are differentially recruited by afferent

and intracortical excitation (Gavrilovici, D'Alfonso, and Poulter 2010; Suzuki and Bekkers 2010b, 2010a; Young and Sun 2009).

The piriform cortex is a trilaminar cortex responsible for processing olfactory stimuli. Principal excitatory neurons are found in layer (L)2/3 and send dendrites to L1 where they receive odor-related excitation directly from the olfactory bulb via the lateral olfactory tract (LOT) (Lewis B. Haberly and Price 1977). LOT afferents also drive horizontal and neurogliaform inhibitory interneurons within L1 yielding feedforward inhibition of principal neurons (Suzuki and Bekkers 2012). Within the cortex, principal neurons send axon collaterals throughout L2/3 and to an intracortical fiber tract in L1b (Lewis B. Haberly and Price 1978; Johnson et al. 2000). Intracortical excitation recruits a number of interneuron classes within L2/3 that, in turn, provide recurrent inhibition to principal neurons (Suzuki and Bekkers 2010b, 2012; Sheridan et al. 2014; C. C. Stokes and Isaacson 2010). Stimulation of the LOT evokes short-latency feed-forward inhibition that targets principal neuron dendrites as well as long-latency, recurrent inhibition that is somatic (Suzuki and Bekkers 2012; C. C. Stokes and Isaacson 2010; Kapur et al. 1997). These findings are consistent with the different laminar locations of inhibitory interneurons mediating feed-forward and recurrent inhibition respectively.

Previous studies have shown that electrical stimulation of the LOT as well as odors recruit mixed feedforward and recurrent inhibition in vivo (Poo and Isaacson 2009, 2011, Biedenbach and Stevens 1966, 1969). However, in vivo and in vitro studies focusing on different principal neuron classes have lead to conflicting reports of the relative contributions of feedforward and feedback inhibition during afferent odor processing (Poo and Isaacson 2009; Suzuki and Bekkers 2012; Sheridan et al. 2014; C. C. Stokes and Isaacson 2010; Luna and Schoppa 2008). Furthermore, due to the disynaptic nature of inhibition, estimates of feedforward

or recurrent inhibitory strength depend on the quality of afferent and intracortical excitatory recruitment, which varies with the different stimulation protocols utilized in each study. Here, we resolve these discrepancies by comparing feedforward and recurrent inhibition evoked by direct optical activation of interneurons that express channelrhodopsin (ChR2) (S. Zhao et al. 2011) as well as electrical stimulation of excitatory pathways in all three classes of principal neuron in the anterior piriform cortex (APC).

In the APC, principal excitatory neuron classes differ in laminar location and in the proportion of afferent versus intracortical excitatory input received (L. Haberly and Behan 1983; Hagiwara et al. 2012; Suzuki and Bekkers 2011; Wiegand et al. 2011). Within L2, semilunar cells (SLCs) receive predominantly afferent excitation while superficial pyramidal cells (sPCs) receive weaker afferent and stronger intracortical excitatory drive. In L3, deep pyramidal cells (dPCs) receive minimal afferent but substantial intracortical excitation. Given these differences in excitatory drive, we hypothesized that inhibition mediated by feedforward and recurrent inhibitory circuits also differs between principal neuron classes. In this study, we find principal neuron classes are weakly inhibited by L1 interneurons that mediate feedforward inhibition compared to L2/3 interneurons that provide strong recurrent inhibition. As predicted, feedforward inhibitory strength varies in manner consistent with the amount of afferent excitation received by each class of principal neuron. In contrast, intracortical stimulation of L3 evokes strong recurrent inhibition that dominates excitation in all classes. Moreover, excitatory and inhibitory profiles differ between SLCs, sPCs and dPCs. Taken together, our results demonstrate that inhibitory circuits in piriform cortex provide both balanced feedforward inhibition and dominant recurrent inhibition, as well as segregate principal excitatory neuron classes during cortical processing.

2.2 MATERIALS AND METHODS

2.2.1 Slice Preparation

Brain slices of anterior piriform cortex were prepared from transgenic vGAT-ChR2 mice that express channelrhodopsin (ChR2) and yellow fluorescent protein (YFP) in interneurons under the promoter for vesicular GABA transporter (S. Zhao et al. 2011) (Jax Mice, Jackson Laboratories). ChR2(-) littermates were used in electrical stimulation paradigms. Experimental animals (P18-30) were of either sex. All surgical procedures were approved by the University of Pittsburgh IACUC. The mice were anesthetized with isoflurane and decapitated. The brain was removed from the skull and immersed in ice cold oxygenated (95% O2-5% CO2) ACSF (in mM: 125 NaCl, 2.5 KCl, 25 NaHCO3, 1.25 NaH2PO4, 1.0 MgCl2, 25 Dextrose, 2.5 CaCl2) (all chemicals from Sigma, USA unless otherwise stated). Parasagittal slices (300 µm) were made using a vibratome (Leica Biosystems, IL) in ice cold ACSF. The slices were transferred to warm ACSF (37°C) for 30 min and then rested at 20-22°C for 1 hour prior to recording (31-35°C).

Electrophysiology: Whole cell, voltage and current clamp recordings were performed using a MultiClamp 700B amplifier (Molecular Devices, Union City, CA). Data were low pass filtered (4 kHz) and digitized at 10 kHz using an ITC-18 (Instrutech) controlled by custom software (Recording Artist, R. Gerkin) written in IgorPro (Wavemetrics). Recording pipettes were pulled from borosilicate glass (1.5 mm, outer diameter) on a Flaming/Brown micropipette puller (Sutter Instruments) to a resistance of 4-12 MΩ (mean 6.4 MΩ). The series resistance was 10-22 MΩ and was not corrected. The intracellular solution consisted of (in mM) 130 K-gluconate, 5 KCl, 2 MgCl2, 4 ATP-Mg, 0.3 GTP, 10 HEPES, and 10 phosphocreatine, 4.5 µM QX-314, 0.05% biocytin. In a small number of cells (n=11) a Cs-Gluconate internal solution was used to enhance

dendritic clamp (100 Gluconic Acid, 5 MgCl2, 0.2 EGTA, 40 HEPES, 2 ATP-Mg, 0.3 GTP, QX-314, 0.05% biocytin, titrated to pH 7.2 with 50% Cs-OH). Recordings were obtained from L2 principal neurons- semilunar cells (SLCs) and superficial pyramidal cells (sPCs) as well as deep pyramidal cells (dPCs) in L3. Neurons were visualized using infrared-differential interference contrast microscopy (IR-DIC, Olympus). Cell classes were confirmed using intrinsic properties and post hoc anatomical reconstruction (Neurolucida, ~85% of reported neurons were recovered, Figure 2Figure 2A). The input resistance (R_n) and time constant (τ_m), of the neurons were assessed in current clamp using a series of hyperpolarizing and depolarizing current steps (-50 pA to 800 pA, 1 s duration). SLCs had significantly higher R_n (403 ± 30 MΩ, $p<0.01$) and τ_m (31 ± 3 ms, $p<0.05$) than sPCs (206 ± 29 MΩ, 21 ± 2 ms) and dPCs (145 ± 11 MΩ, 19 ± 2 ms). L2 and L3 PCs did not differ in Rn or τ_m. Resting membrane potentials (V_m) did not differ between classes (SL: 71 ± 2 mV; sPCs: 71 ± 2 mV; dPCs: -73 ± 2 mV). With respect to interneurons, FS and RS cells differed in τ_m (FS: 7 ± 0.5 ms; RS: 13 ± 2 ms, p:0.004) and Sag (FS: 0.5 ± 0.1 mV; RS: 2.0 ± 0.5 mV; p:0.01). Although R_n (FS: 125 ± 14 MΩ; RS: 129 ± 14 MΩ, p:0.83), Vm (FS: -72 ± 2 mV; RS: -65 ± 3 mV; p: 0.09), rheobase (FS: 158 ± 23 pA; RS: 92 ± 20 pA; p: 0.06) and max firing rates (FS: 190 ± 30 Hz; RS: 130 ± 9 Hz: p:0.09) did not differ between FS and RS cells, these values were consistent with FS and RS classifications in previous studies (Suzuki and Bekkers 2010b; Young and Sun 2009).

2.2.2 Light Stimulation

Blue light (λ=460-488 nm, GFP block, Olympus) for optical stimulation was provided by metal halide lamp (200W, Prior Scientific) passed through the microscope objective (60x, immersion, Olympus). The light spot was restricted to a ~70 μm diameter (0.5 mW) using the minimum

aperture. To obtain the spatial profile of inhibition, interneurons were focally activated in a 5x4 grid pattern while IPSCs were recorded in SLCs or sPCs (L2) or dPCs (superficial L3). The horizontal axis of the grid was centered on the recorded neuron with stimulation sites ranging from -300 µm (rostral) to +300 µm (caudal) at 150 µm increments. The vertical axis ranged L1 to L3 in 125 µm increments corresponding to different lamina. Each grid site was stimulated with 2 light pulses (20 ms duration, 100 ms interpulse interval, 15 s between trials). Light pulses were controlled using a mechanical shutter (Sutter Instruments) driven by TTL output. The 20 ms duration was chosen to reliably evoke least one spike and rarely 2 spikes in response to a single pulse of direct somatic stimulation using the 70 µ spot at 0.5 mW (Figure 2). Grids were repeated 3-5 times per neuron and each grid site was stimulated once every 6 min.

2.2.3 Electrical Stimulation

Electrical stimulation of the LOT and L2/3 border was delivered through concentric bipolar electrodes (FHC). Electrodes were placed at a distance of 300-400 µm on the rostral (LOT) and caudal (L2/3) sides of the recorded cells. Evoked postsynaptic currents (PSCs) were recorded in principal neurons that were alternately held at the measured reversal potential for excitation, 0 to +10 mV (IPSCs) and at the measured reversal potential for inhibition, -40 to -50 mV (EPSCs). Under these conditions the driving forces for excitation and inhibition were approximately matched (50 V). Stimuli consisted of single pulses (100 µs) delivered from a stimulus isolation unit (AMPI). The initial stimulation intensity was set for each neuron as the minimum required to evoke a PSC (2-7V). Stimulus intensity was then increased in 1V increments up to +5V.

2.2.4 Analysis

Electrophysiology traces are presented as the average across trials for individual neurons. Analyses across neurons are presented as the mean ± standard error (SE). For optogenetic stimulation, IPSC strength was taken as the area (pA·s) under the first IPSC. Comparisons of EPSC and IPSC strength were based on peak amplitude within 10 ms of PSC onset. Average PSCs with minimum amplitude of 10 pA were included for analyses; smaller PSCs were not distinguishable from noise (~5-10 pA).

Unless otherwise stated, all statistical comparisons were made using paired and unpaired Student's t-tests with Bonferroni correction for multiple comparisons as needed. Pearson's correlation was used to for significance of linear fits

2.3 RESULTS

We investigated the strength of inhibition onto principal excitatory neurons (Figure 2A) in sagittal slices of APC from transgenic mice that express ChR2 in the majority of interneurons under the vGAT promoter (S. Zhao et al. 2011). For each principal neuron, we obtained the spatial profile of inhibition based on the laminar locations of interneuron somas. Briefly, interneuron somas were focally activated using light spots (see methods) in a 5x4 grid pattern surrounding the principal neuron (Figure 2B). Focal light stimuli reliably recruited action potentials when centered on interneurons (1.76 ± 0.38 spks/trial, two light pulses per trial) but not at off-soma locations >150 µm from the soma (0.44 ± 0.09 spks/trial, p: 1.8E-06, n=14, Figure 2C,D). Since interneuron classes could differentially to respond to optogenetic activation,

we classified the interneurons as FS (n=6) and RS (n=6) based on intrinsic membrane and spiking properties (see methods). Two interneurons were not categorized. Spike responses did not differ between RS and FS cells for on-soma (p: 0.38) or off-soma (p: 0.07) optogenetic stimulation. In all cells, spikes were evoked within 8.6 ± 1.9 ms of the onset of the first light pulse (98 ± 18% of trials) but failed on the second pulse in ~20% of trials (Figure 1E). For this reason, only IPSCs evoked by the first light pulse were analyzed.

Evoked inhibitory postsynaptic currents (IPSCs) were recorded in SLCs, sPCs or dPCs that were voltage clamped near 0 mV (Figure 2F). IPSCs were abolished in the presence of the sodium channel antagonist, tetrodotoxin (1 µm, TTX) and the potassium channel agonist, 4-aminopyradine (100 µm, 4-AP) for light intensities up to 1mW (n=4) suggesting that direct terminal release does not contribute substantially to our results (Figure 2F). Thus, the spatial profiles of inhibitory currents reflect the somatic locations of the interneurons rather than synaptic locations on the principal neurons. Near rest (-70 mV) IPSCs were outward currents that reversed between -50 and -40 mV (n=8, Figure 2G).

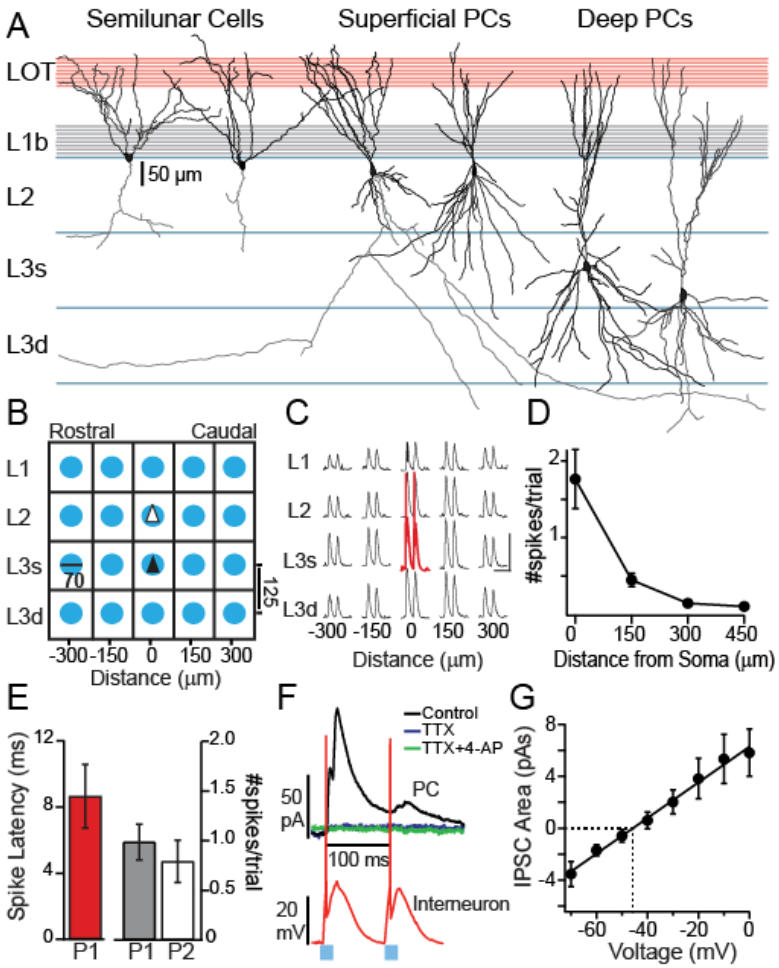

Figure 2. Experimental Design.

A) Schematic of laminar locations of recorded neurons. Neurolucida reconstructions corresponding to semilunar cells superficial and deep pyramidal cells. Scale bar: 50 µm (for traces only). B) Schematic of stimulation grid for light spots (70 µm diameter) directed at locations in layers (L) 1, 2, and superficial (s) and deep (d) L3 (125 µm between sites) as well as along the rostral-caudal axis (150 µm between sites). Recording sites are indicated by triangles for SLCs & sPCs (white) and dPCs (black). C) Response of a representative interneuron to light activation of grid locations. Neuron only spiked in response to light directed at soma (red trace), spikes truncated. Scale bars: vertical: 20 mV, horizontal: 200 ms. D) Number of spikes per trial versus stimulation distance from soma (n=14 interneurons). E) Left: Average latency to first spike relative to light onset at soma. Right: Average number of spikes on the first and second light pulses. F) Representative traces from interneuron (red, spikes) and L3 dPC (black, IPSC) aligned to light onset (neurons were not recorded simultaneously). In the same dPC, light evoked IPSCs were lost in the

presence of TTX and could not be recovered by the addition of 4-AP. G) Average IPSC strength (Area, pA·s) at different holding potentials in response to light directed at the soma. On average, IPSCs reversed at ~-45 mV (dashed lines).

In Figure 3A, IPSCs recorded during grid stimulation are shown for a representative SLC, sPC and dPC. Similar results have been previously obtained using glutamate uncaging (Luna and Pettit 2010). Since IPSCs likely reflect population responses, the strength of inhibition was quantified as the area (pA·s) under the first peak of the trial-averaged IPSC evoked at each location. For each cell class, these values were averaged across neurons at each grid location and presented as a heat map (Figure 3B). To obtain laminar averages, inhibition was averaged across rostral-caudal position for each layer and then averaged across neurons within class (Figure 3D).

Comparison of the inhibitory spatial profiles of the principal neuron classes yielded three striking findings. First, the majority cells (60% SLCs (n=13), 64% sPCs (n=14), 88% dPCs (n=14)) received the maximal inhibition from a location in L3 (black stars, Figure 2B). In the case of SLCs and sPCs, this meant that interneurons nearest to the soma did not necessarily provide the strongest inhibition. Second, inhibitory strength recorded at the location of maximal inhibition did not differ between SLCs and sPCs (SLCs: 3.6 ± 0.69 pA·s; sPCs 3.6 ± 0.69 pA·s, p: 0.46) but was significantly stronger in dPCs (8.6 ± 0.84 pA·s, **, p: 9.0E-4, Figure 3C). Likewise, the average laminar inhibition did not differ between SLCs and sPCs, but dPCs received significantly stronger inhibition from all layers compared to L2 neurons (+: $p<0.05$; ++: $p<0.01$, Figure 2D). Finally, in all cell classes, light activation of L1 sites produced the weakest IPSCs compared to L2 and L3 sites (**<0.01, Figure 3D). All of these findings suggest that, at the soma, recurrent inhibition provided by L2/3 is stronger than feedforward inhibition from L1.

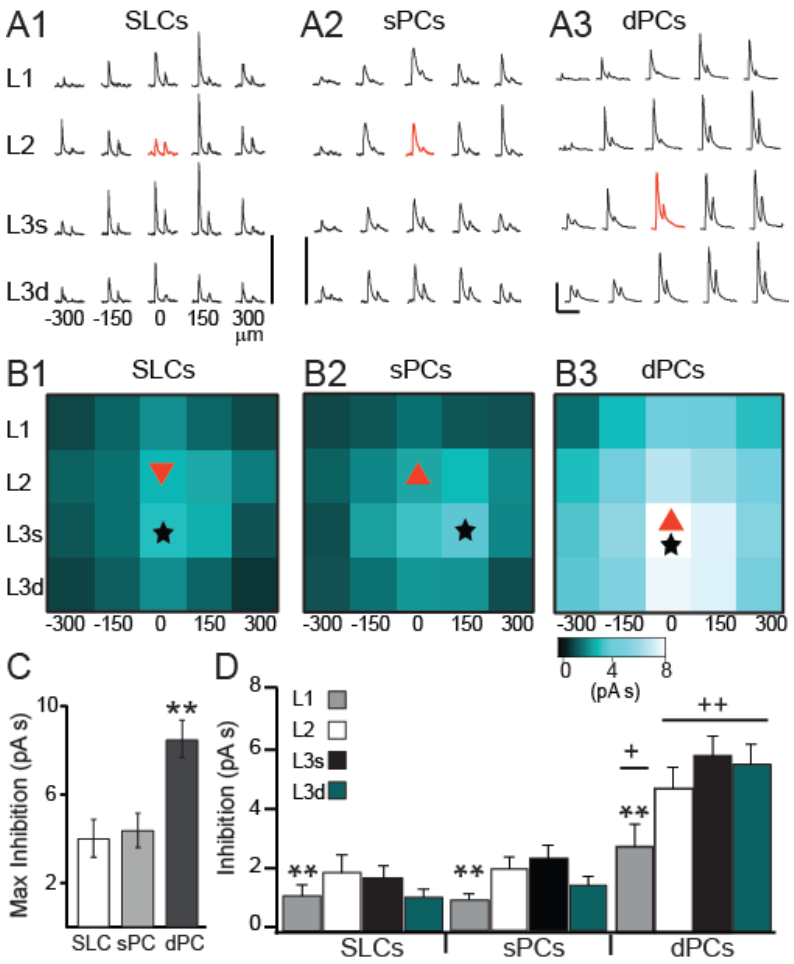

Figure 3. Spatial profiles of inhibition differ between principal neuron classes.

A) IPSCs in response to grid stimulation for a representative neuron from each class (A1: SLCs, A2: sPCs, A3: dPCs). Red traces indicate responses when light was centered on the soma. Scale bars: vertical: 100 pA, horizontal: 200 ms. B) The strength of inhibition (Area, pA·s) from each grid location averaged across neurons of the same class (B1: SLCs, B2: sPCs, B3: dPCs). Location of recorded neuron indicated by red triangle. Location of strongest average inhibition indicated by black star. C) The average maximum inhibition for each class regardless of grid location. (**: $p<0.01$). D) The average inhibition across all sites in a layer, averaged across all neurons of the class. In all classes, inhibition from L1 was significantly less than L2 or L3s: ** $p<0.01$. dPCs received significantly stronger inhibition in all layers than SLCs or sPCs: +<0.05, ++<0.01 (unpaired, two tailed, t-tests)

2.3.1 Analysis of feedforward and recurrent excitation and inhibition

Optical activation of interneurons suggests that afferent excitation from the LOT (L1a) drives weak feedforward inhibition through L1 interneurons compared to the recruitment of recurrent inhibition by intracortical excitation. To investigate the relationship between excitation and inhibition in feedforward and recurrent circuits, we electrically stimulated the LOT or L2/3 respectively to compare evoked excitation and inhibition in the three cell classes. In all cases, stimulation strength was set at the threshold voltage (T) required to reliably elicit a PSC (either excitatory or inhibitory). To obtain an intensity-response curve, the stimulus voltage was then increased from T in 1V increments (Figure 4A). Unless otherwise stated, all measurements and statistical tests were taken at the midpoint of these curves.

For LOT stimulation, T was significantly lower in SLCs (2.8 ± 0.36V, $p<0.05$) than sPCs (4.5 ± 0.48V) or dPCs (4.6 ± 0.60 V). Since electrical and optogenetic stimulation regimes differ we compared the area (pA·s) of evoked IPSCs during maximal LOT stimulation (T+4V) and the average light evoked inhibition (area, pA·s) across L1 sites. IPSC strength did not differ between LOT and optogenetic stimulation (L1) in SLCs (LOT: 0.91 ± 0.14, L1: 1.15 ± 0.36), sPCs (LOT: 1.1 ± 0.29; L1: 0.94 ± 0.18) or dPCs (LOT: 1.8 ± 0.38; L1: 2.8 ± 0.73; $p>0.05$, t-test). This suggests that L1 mediated inhibition evoked in light activated and electrical regimes is comparable.

This relatively weak electrical stimulation regime was chosen to minimize polysynaptic activity and contamination of afferent responses by intracortical recruitment. To further reduce the possibility of analyzing polysynaptic responses during electrical stimulation, the peak amplitudes (rather than area) of the shortest latency PSCs were used to compare EPSC and IPSC strength. In all neuron classes, IPSC onsets (in ms, SLCs: 3.1 ± 0.46; sPCs: 4.3 ± 0.56; dPCs: 4.7

± 0.79) followed EPSC onsets (in ms, SLCs: 2.0 ± 0.13; sPCs: 2.2 ± 0.22; dPCs: 2.4 ± 0.19) with a short delay (1-2 ms) indicative of disynaptic feedforward inhibition.

In total, 9/9 SLCs and 12/12 sPCs, but only 9/14 dPCs (64%) received excitation during LOT stimulation. At threshold, SLCs received significantly stronger excitation (31± 9 pA) than SPCs (12 ± 3 pA, p: 0.02) or dPCs (14 ± 3 pA, p: 0.04) consistent with previous reports [36, 39]. However, the midpoint excitatory strength did not differ between SLCs (60 ± 9 pA), sPCs (41 ± 9 pA) and dPCs (44 ± 11 pA, p>0.05), (Figure 3A). We next compared the strength of EPSCs and IPSCs in each class of principal neuron (Figure 4A,B). In SLCs and sPCs, inhibitory strength approximately matched excitation at most stimulation intensities (Figure 4A). The midpoint IPSC strength (SLCs: 68 ± 17 pA, p: 0.22; sPCs: 46 ± 24 pA, p: 0.64) did not differ from excitation (above). In dPCs, inhibition was significantly weaker than excitation at the midpoint (28 ± 10 pA; p: 0.05), but did not differ at other stimulation intensities. The correlation between EPSC and IPSC strength was assessed for all individual EPSC-IPSC pairs in each neuron (Figure 4B, blue circles) as well as for the average PSC strengths across neurons (black triangles). In all cases, the correlations were close to 1 for individual pairs (SLCs: 0.76 ± 0.12, r: 0.75, p:1E-5; sPCs 1.0 ± 0.1, r: 0.8, p:1E-5; dPCs 0.69 ± 0.09, r: 0.738, p:1E-5) and average strengths (SLCs: 0.79 ± 0.06, r: 0.75, p:3E-3; sPCs 1.3 ± 0.20, r: 0.96, p: 0.009, dPCs: 1.1 ± 0.11, r: 0.98, p: 0.003). These results suggest that feedforward excitation and inhibition are approximately balanced at low stimulation intensities.

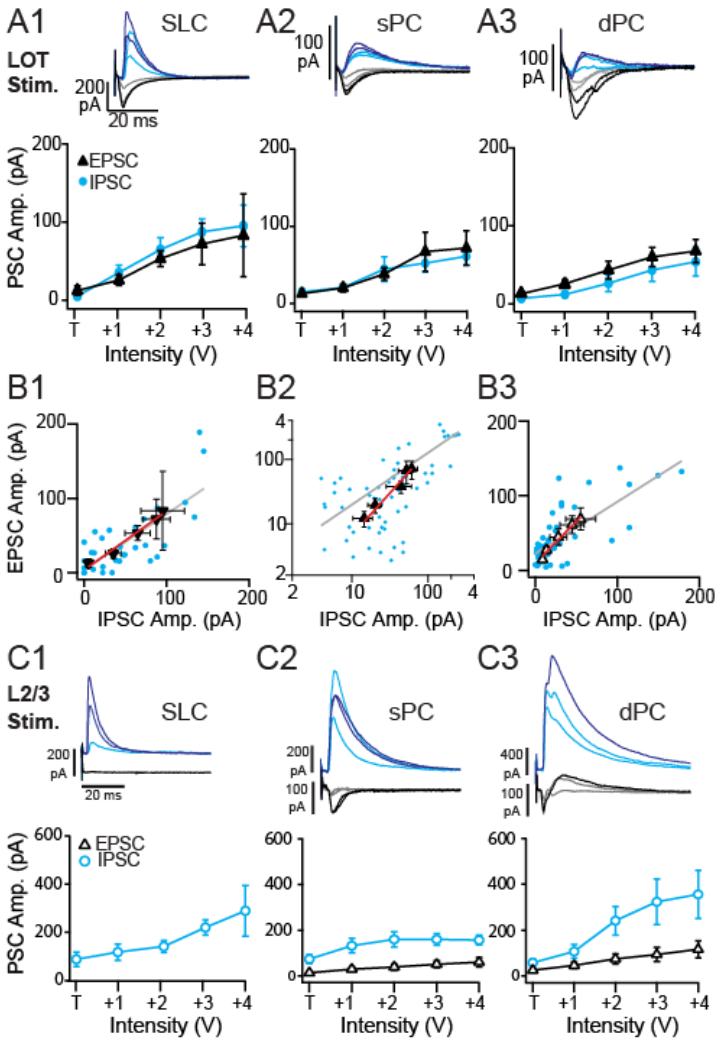

Figure 4. Feedforward and recurrent excitation and inhibition.

A) Analysis of synaptic currents in principal neurons in response to electrical stimulation of the LOT for intensities that increase in 1V increments from threshold (T) for evoking a PSC. Upper: EPSCs (grey to black) and IPSCs (light to dark blue) in response to increasing intensity for an SLC (A1), sPC (A2) and dPC (A3). Lower: Average EPSC (black triangles) and IPSC (blue circles) amplitudes for increasing stimulation intensity in SLCs (A1, n=9), sPCs (A2, n=12); and dPCs (A3, n=9). B) EPSC amplitude versus IPSC amplitude for individual neurons at various stimulation intensities (blue circles), linear fit (gray line). Average PSC amplitudes and linear fit are plotted as well (black triangles, red line). C) Analysis of synaptic currents in principal neurons in response to L2/3 electrical stimulation for intensities that increase in 1V increments from threshold (T) for evoking a PSC. Upper: EPSCs (grey to black) and IPSCs (light to dark blue) in response to increasing intensity for an SLC (C1), sPC (C2) and dPC (C3). Note differences in

scale bars for excitation and inhibition. Lower: Average EPSC (black triangles) and IPSC (blue circles) amplitudes across SLCs (B1, n=8), sPCs (B2, n=12); and dPCs (B3, n=14).

Previous studies used higher LOT stimulation intensities or multiple pulses that evoke spike responses in excitatory neurons and recruit recurrent inhibition from L2/3 interneurons (Sheridan et al. 2014; C. C. Stokes and Isaacson 2010). To investigate excitation and inhibition recruited by intracortical circuits in the absence of afferent drive, we electrically stimulated (ES) the border of L2/3. Inhibition (area, pA·s) during ES was again comparable to the average light (LS) evoked inhibition from superficial L3 in SLCs (ES: 2.5 ± 0.74, LS: 1.74 ± 0.36), sPCs (ES: 3.5 ± 0.72; LS: 2.18 ± 0.41) and dPCs (ES: 6.4 ± 3.1; LS: 5.8 ± 0.66). Intensity-response curves were generated with thresholds between (5-7V) that did not differ between classes. All sPCs and dPCs recorded received both excitation and inhibition. However, in all 8/8 SLCs, excitation could not be discerned. Consistent with disynaptic recruitment of inhibition, EPSCs (in ms, sPCs: 2.6 ± 0.4; dPCs: 3.4 ± 0.5) significantly preceded IPSCs (in ms, sPCs: 3.7 ± 0.4; dPCs: 4.8 ± 0.4; $p<0.05$). In SLCs, IPSC latencies were 3.6 ± 0.4 ms.

In all neuron classes, inhibition was significantly stronger than excitation in response to L2/3 stimulation (Figure 4C). Despite the absence of L2/3 excitation, SLCs received robust inhibition (198 ± 42 pA) (Figure 4C1). Further, IPSCs were significantly stronger than EPSCs in both sPCs (IPSC: 159 ± 32 pA, EPSC: 39 ± 13 pA, p: 0.004) and dPCs (IPSC: 323 ± 98 pA, EPSC: 75 ± 21 pA, p: 0.02) (Figure 3C2,3). Finally, in SLCs, sPCs and dPCs, inhibition evoked by L2/3 stimulation was significantly greater than that evoked by LOT stimulation (comparison of midpoints; SLCs, p: 0.03; SPCs, p: 0.007; dPCs: p: 0.015).

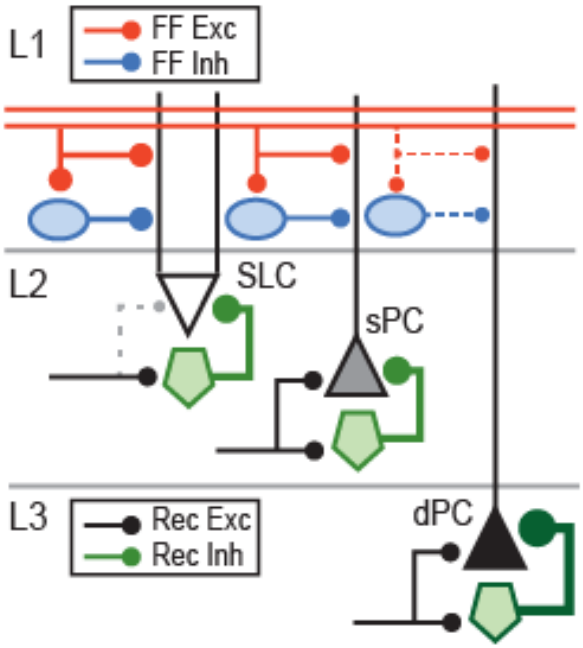

Figure 5. Feedforward and recurrent circuits in APC principal neurons.

The results of this study are summarized schematically. Afferent inputs from the olfactory bulb arrive via the lateral olfactory tracts (LOT) in L1a. Feedforward excitation (red) and disynaptic inhibition via L1 interneurons (blue) is weak and balanced in SLCs (white inverted triangle) and sPCs (grey triangle). Feedforward inputs to dPCs (black triangle) were rare and weak (dashed lines). Recurrent inhibition mediated by L2/3 interneurons (green) is significantly stronger than recurrent excitation (black) in all cell classes. SLCs did not receive L2/3 excitation in the present study (dashed). dPCs received the strongest recurrent inhibition from L2/3 (thick green line).

Notably, LOT-evoked currents may appear weaker (or even absent in dPCs) due to dendritic filtering compared to somatic synapses from L2/3 inhibition. A subset of our recordings in sPCs (n=5/13) and dPCs (n=6/14) were performed with Cs-gluconate internal solution (see methods) to enhance dendritic space clamp. EPSC and IPSC amplitudes evoked by LOT or L3 stimulation did not significantly differ at any intensity in either cell class compared to recordings with K-gluconate solution (Figure 6). Further, the reliability of LOT input to dPCs was

comparable in both solutions (Cs+: 4/6 (66%) neurons, K+: 5/8 (63%) neurons). These results are consistent with previous findings that pyramidal cell dendrites in piriform cortex minimally filter inputs (Bathellier, Margrie, and Larkum 2009). Nonetheless, in Cs+ recordings, LOT-evoked excitation and inhibition were balanced, while L2/3-evoked inhibition was substantially stronger than L2/3 excitation and L1 inhibition (Figure 6). Thus, balanced feedforward excitation and inhibition from L1 likely plays a prominent role in dendritic integration of afferent input in all cell classes but contributes weakly to spike regulation at the soma. Alternately, recurrent circuits within L2/3 provide strong, dominant inhibition that controls somatic activity.

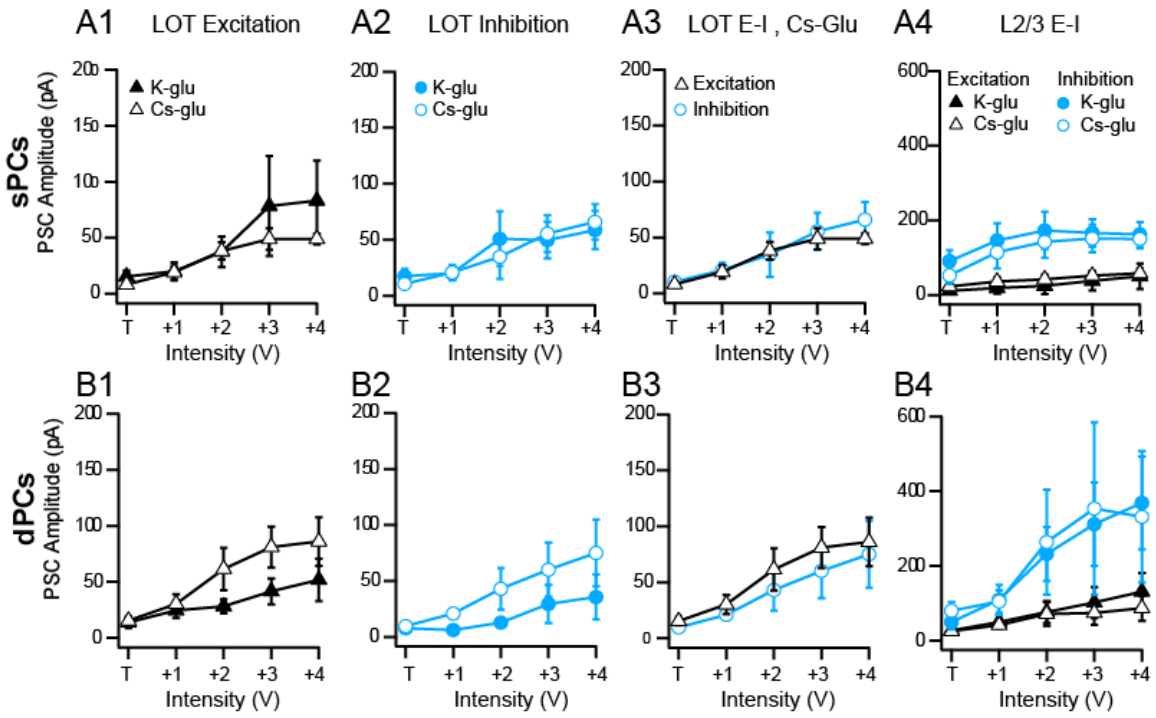

Figure 6. Comparison of PSC amplitudes recorded using different intracellular solutions.

A1-4) Recordings from sPCs. A1) EPSC amplitudes recorded in K+-gluconate (solid triangles, n=8) and Cs-gluconate (open triangles, n=5) in response to LOT stimulation of increasing intensity. A2) IPSC amplitudes recorded in K+-gluconate (solid circles, n=8) and Cs-gluconate (open circles, n=5) for LOT stimulation. A3) EPSCs and IPSCs recorded in Cs-gluconate are balanced during LOT stimulation. A4)

EPSC and IPSCs recorded in response to L2/3 stimulation with increasing intensity (symbols as in A1, A2). Inhibition dominates excitation in both solutions. B1-4) Recordings from dPCs (description as in A1-4). Sample sizes were n=4 (Cs+) and n=5 (K+) for LOT stimulation and n=4 (Cs+) and n=10 (K+) for L2/3 stimulation. In both sPCs and dPCs, PSC amplitudes did not significantly differ between K-gluconate and Cs-gluconate solutions, p: 0.21-0.52 Mann Whitney U-test. Mean±SE.

2.4 DISCUSSION

In this study we investigated inhibition onto three classes of principal neurons in the APC-semilunar cells (SLCs), superficial (sPCs) and deep pyramidal cells (dPCs). We present three main findings. First, feedforward inhibition from L1 interneurons is balanced by afferent excitation in all principal neuron classes. Second, recurrent inhibition from L2/3 interneurons dominates intracortical excitation in all cell classes. Finally, SLCs, sPCs and dPCs, differ in their recruitment and inhibition and by afferent versus recurrent circuits. These findings have important implications for the interpretation of previous studies and ultimately, cortical processing of olfactory information.

2.4.1 Afferent versus intracortical recruitment in principal neuron classes.

In Figure 5, we schematize the differential recruitment and inhibition of principal neurons by afferent versus recurrent pathways. We, and others, have found that SLCs have the lowest thresholds for afferent recruitment and strong EPSCs that depress during ongoing stimulation (Suzuki and Bekkers 2011; Oswald and Urban 2012; Suzuki and Bekkers 2006). SLCs did not receive recurrent excitation (dashed lines, Figure 5) from L2/3 consistent with a lack of basal

dendrites (Figure 2) and synapses (L. Haberly and Behan 1983) in regions corresponding to intracortical projections (L1b, L2/3). Conversely, sPCs and dPCs have higher thresholds for afferent excitation, EPSCs that facilitate and receive intracortical excitation (Suzuki and Bekkers 2011; Oswald and Urban 2012; Suzuki and Bekkers 2006). However, in contrast to SLCs and sPCs, one third of dPCs did not receive afferent input (dashed lines Figure 5). It is possible that longer dendrites in dPCs filter afferent EPSCs and IPSCs to undetectable levels when recorded at the soma. However, this also implies that substantial afferent input alone, or in combination with intracortical drive, is required for L1 inputs to affect somatic responses in dPCs. Alternatively, current source density analyses show that L3 responds to afferent drive with considerable delay (Ketchum and Haberly 1993) suggestive of dominant disynaptic intracortical activity. In all classes, feedforward inhibition is weak but balanced with respect to afferent excitation. In addition, all classes receive recurrent inhibition, though SLCs and sPCs receive significantly less recurrent inhibition than dPCs. Altogether, these results suggest that SLCs and sPC play sequential roles in afferent processing of olfactory bulb input (Suzuki and Bekkers 2011) but support a more prominent role for dPCs in intracortical and feedback processing (Wiegand et al. 2011).

2.4.2 Feed-forward Inhibition

There have been conflicting descriptions of the contributions of feed-forward and recurrent inhibition to odor processing (Poo and Isaacson 2009; Suzuki and Bekkers 2012; Sheridan et al. 2014; C. C. Stokes and Isaacson 2010; Luna and Schoppa 2008). For example, it has been suggested that feedforward inhibition is broadly tuned in vivo (Poo and Isaacson 2009). However in vitro studies suggest that SLCs receive feedforward inhibition (Suzuki and Bekkers

2012) while pyramidal cells receive mainly recurrent inhibition (Sheridan et al. 2014; C. C. Stokes and Isaacson 2010). These discrepancies likely arise because each study focused on a different cell class and used different stimulation regimes. By selectively activating interneurons with light in the absence of afferent excitation, we find that all principal neuron classes are inhibited by L1 interneurons. Using weak LOT stimulation, we find short latency, feedforward inhibition in all cell classes. Since feedforward inhibition is significantly weaker than that from L2/3 interneurons for both optogenetic and electrical stimulation, it is conceivable that feedforward inhibition is obscured by recurrent inhibition in strong stimulation regimes of previous studies. A key finding of our study is that afferent excitation and feedforward inhibition are balanced in principal neurons. This contrasts with in vivo recordings that show selective, odor-evoked excitation but broadly tuned inhibition (Poo and Isaacson 2009). It is possible that weak LOT stimulation evokes subthreshold EPSCs and IPSCs that are balanced but not apparent in stronger, odor-evoked responses that recruit recurrent inhibition (Poo and Isaacson 2011; Sheridan et al. 2014; C. C. Stokes and Isaacson 2010). Finally, in vivo recordings may include deep pyramidal neurons, which we find receive less reliable LOT input, but robust broadly tuned, recurrent inhibition. Finally, Thus, our results do not preclude the interpretation that feedforward inhibition is broadly tuned, but the relationship with respect to excitation could change with stimulation regime.

Nonetheless, feedforward inhibition likely plays an important role in dendritic integration. Here we show that at low stimulus intensities, feedforward inhibition is weak and balances afferent excitation. This suggests that sparse, subthreshold excitatory inputs could be effectively modulated by balanced feedforward inhibition. However, since feedforward inhibition is delayed, and depresses with bursts of input (C. C. Stokes and Isaacson 2010) these

circuit parameters may also permit supralinear responses at intermediate levels of excitation (Murphy and Miller 2009; Ozeki et al. 2009) provided they are subthreshold for recruiting dominant feedback/recurrent inhibition (Suzuki and Bekkers 2012; Sheridan et al. 2014; C. C. Stokes and Isaacson 2010). For example, short-term facilitation of afferent excitation by presynaptic bursts (Oswald and Urban 2012; Suzuki and Bekkers 2006) or increases in the number or correlation of olfactory bulb inputs (Davison and Ehlers 2011) could outpace feedforward inhibition and enhance cortical responses to weak but potentially relevant olfactory stimuli.

2.4.3 Recurrent Inhibition

Odor driven synaptic responses suggest that recurrent excitation of pyramidal cells is stronger and more broadly tuned than afferent drive (Poo and Isaacson 2009, 2011). Likewise, we find that optogenetic and electrical stimulation of recurrent circuits provide significantly stronger inhibition to all principal neuron classes than feedforward circuits. We also find that recurrent inhibition that is substantially stronger than excitation in all cell classes. Similar results have been shown for L2 pyramidal cells (PCs) in APC (Franks et al. 2011). Importantly, although inhibition is dominant, it co-varies with excitation in PCs (Franks et al. 2011). Both PCs and interneurons in L2/3 are driven by local and long-range intracortical excitation (Suzuki and Bekkers 2010b; Franks et al. 2011). In turn, L2/3 interneurons provide feedback and recurrent inhibition to SLCs and PCs (Suzuki and Bekkers 2012; Sheridan et al. 2014). Thus, strong inhibition from L2/3 serves two important roles: 1) feedback inhibition that further limits afferent and intracortical integration windows (Suzuki and Bekkers 2012; Sheridan et al. 2014; Luna and Schoppa 2008) and 2) stabilization of the recurrent excitatory network (Franks et al.

2011). In the former case, SLCs provide excitatory drive to fast-spiking interneurons (Suzuki and Bekkers 2012), which provide delayed feedback inhibition to SLCs and sPCs (Suzuki and Bekkers 2012; Sheridan et al. 2014; C. C. Stokes and Isaacson 2010). In the latter case, odors evoke strong, broadly tuned, intracortical excitation (Poo and Isaacson 2011). The recruitment of strong feedback inhibition under these conditions could function to prevent runaway excitation and stabilize the network resulting in sublinear or normalization of cortical responses (Rubin, Van Hooser, and Miller 2015; Franks et al. 2011). Consistent with this idea, disinhibition of the piriform cortex leads to epileptic activity (Birjandian, Narla, and Poulter 2013; Demir, Haberly, and Jackson 1998, 2001; Gavrilovici et al. 2006). Altogether, these feedforward and recurrent circuit features likely promote sparse responses (McCollum et al. 1991; Miura, Mainen, and Uchida 2012; Rennaker et al. 2007; Stettler and Axel 2009; Zhan and Luo 2010) and low correlations (Graupner and Reyes 2013; Litwin-Kumar et al. 2011; Miura, Mainen, and Uchida 2012) during odor processing.

2.4.4 Summary

The ability to separate afferent and recurrent inhibitory circuits in piriform cortex provides insight to the relative contributions of these circuits to neural responses. Here we show that at low stimulus intensities, feedforward inhibition balances afferent excitation. Higher stimulation intensities likely recruit intracortical excitation and ultimately dominant L2/3 recurrent inhibition. These circuit features are consistent with balanced and inhibition stabilized network models (Murphy and Miller 2009; Ozeki et al. 2009; Rubin, Van Hooser, and Miller 2015) that replicate supra- and sublinear computations in visual and auditory cortex (Schummers, Sharma,

and Sur 2005; Y. Zhao et al. 2015). Thus, feedforward and recurrent inhibition in the piriform cortex could represent global mechanisms for sensory processing throughout the brain.

3.0 INHIBITION BY SOMATOSTATIN INTERNEURONS IN OLFACTORY CORTEX

3.1 INTRODUCTION

Throughout the cortex, inhibitory interneurons that express somatostatin (SST) have been implicated in numerous aspects of sensory processing including gain control and/or tuning (Adesnik et al. 2012; N. R. Wilson et al. 2012; Stryker 2014; Seybold et al. 2015; Sturgill and Isaacson 2015). Somatostatin interneurons inhibit excitatory pyramidal cells (Fino and Yuste 2011; Pfeffer et al. 2013) as well as inhibitory interneurons, including parvalbumin (PV) cells (Pfeffer et al. 2013; Jiang et al. 2015; Xu et al. 2013). Thus, SST-cells can both directly inhibit and indirectly disinhibit pyramidal cells (Cottam, Smith, and Häusser 2013; Xu et al. 2013). With respect to direct inhibition, SST-cells primarily inhibit pyramidal cell dendrites and regulate postsynaptic Ca2+ signals, spike bursts, spine and synapse dynamics (Chiu et al. 2013; Marlin and Carter 2014; S. X. Chen et al. 2015). In addition, ongoing SST-cell activity can also modulate excitatory transmission through GABAergic activation of presynaptic GABAB receptors (Urban-Ciecko, Fanselow, and Barth 2015). In contrast to extensive analysis of SST-mediated inhibition in neocortex, little is known about the circuitry of SST-cells in piriform cortex. In this study, we investigate SST-cell properties and inhibitory connectivity in the piriform cortex to gain insight into the roles these interneurons play in olfactory processing.

The anterior piriform cortex (APC) is a trilaminar paleocortex responsible for processing olfactory information (Donald A. Wilson and Sullivan 2011; Bekkers and Suzuki 2013). Pyramidal cells (PCs) are found in layer (L)2/3 and project apical dendrites to L1 to receive direct input from the olfactory bulb (L1A) as well as intracortical excitation (L1B). In addition, PCs project axons throughout L2/3 to recruit feedback or recurrent inhibition from a number of interneuron classes including SST-cells and parvalbumin (PV) neurons(Lewis B. Haberly and Price 1978; Suzuki and Bekkers 2010b, 2010a, 2012). SST-expressing interneurons account for ~30% of interneurons in piriform cortex (Suzuki and Bekkers 2010a). SST-cells have been shown to extend axons to L1B as well as make synaptic connections with pyramidal cells (Suzuki and Bekkers 2010b, 2010a), although direct dendritic inhibition has not been verified. This suggests that SST-interneurons are poised to regulate dendritic excitability as in neocortical circuits. More recently, optogenetic inactivation of SST-cells revealed that SST-interneuron activity narrows odor-tuning curves through subtractive inhibition (Sturgill and Isaacson 2015). However, it is unclear whether the mechanism involves direct inhibition of pyramidal cells, inhibitory interneurons, or both. These studies highlight the importance of understanding how SST-interneurons participate in APC circuits to affect the activity of both pyramidal cell and inhibitory interneurons.

In this study we characterized the expression patterns, intrinsic physiology and inhibitory connectivity of SST-interneurons in the APC. We used commercially available transgenic mouse lines that target either SST cells (SST-cre and GIN) or PV-cells (PV-cre and G42). These lines are commonly crossed to express GFP in target postsynaptic cells (GIN, G42, (Oliva et al. 2000; Chattopadhyaya et al. 2007, 67) and channelrhodopsin (ChR2) in presynaptic cells (cre-lines, (Madisen et al. 2012). However, we find that the densities and electrophysiological

properties of GIN and G42 cells are not representative of the majority of SST and PV interneurons in APC ruling out this strategy. Instead we expressed ChR2 in SST-cre animals and used a clustering algorithm to differentiate postsynaptic interneurons based on intrinsic properties. As expected from neocortical studies, we found that SST-interneurons broadly inhibited a variety of interneuron classes, including putative PV cells. However, in contrast to neocortex (Pfeffer et al. 2013), we also found that SST-cells can strongly inhibit each other. Further, we confirm that SST-cells inhibit the distal dendritic and perisomatic regions of pyramidal cells. Finally, we discuss potential limitations of these findings due to the expression strategies utilized. Altogether, we provide new information about the distributions and intrinsic properties of SST-cell subtypes in commonly used transgenic lines as well as the inhibitory connectivity of SST-cells in APC circuits. These findings are first step toward understanding the roles SST-interneurons play in odor processing in piriform cortex.

3.2 MATERIALS AND METHODS

3.2.1 Mice

We used six commercially available transgenic mouse lines in this study obtained from Jackson Laboratories. GIN (FVB-Tg(GadGFP)45704Swn/J) and G42(CB6-Tg(Gad1-EGFP)G42Zjh/J) mice express green fluorescent protein (GFP) in subsets of Somatostatin (SST) and Parvalbumin (PV) interneurons respectively. SST-cre (SSTtm2.1(cre)Zjh/J) and PV-cre (Pvalbtm1(cre)Arbr/J) mice express cre-recombinase under the promoters for somatostatin and parvalbumin respectively. We crossed these cre mice with Ai14 (B6;129S6-

Gt(ROSA)26Sortm14(CAG-tdTomato)Hze/J) or Ai32 (B6.Cg-Gt(ROSA)26Sortm32(CAG-COP4*H134R/EYFP)Hze/J) mice to produce offspring that express tdTomato (SST-tdTom, PV-tdTom) or channelrhodopsin (SST-ChR2) respectively. Mice of both sexes were used in all experiments. The University of Pittsburgh IACUC approved all procedures.

3.2.2 Anatomy

GIN, G42, SST-tdTom or PV-TdTom mice (P200-300) were given an overdose (500 µl) of ketamine (100mg/kg) and xylazine (10 mg/kg) cocktail then transcardially perfused with ice cold phosphate buffered saline (PBS) followed by 4% paraformaldehyde (PFA). Brains were removed and post-fixed for 24h in 4% PFA then sunk in 30% sucrose solution overnight. Coronal sections (50 µm) were cut on a freezing microtome and maintained in phosphate buffer prior to immunochemistry or mounting. Every other section was mounted using fluoromount to protect fluorescence and minimize background. Sections were imaged on a Nikon Eclipse-Ci microscope at 4x-20x magnifications. Illumination was provided by a mercury lamp (Nikon Intensilight) and delivered through appropriate filter blocks for GFP (495 nm) and tdTomato (585 nm). Light intensity and exposure duration (100-400 ms) were optimized for the first section in a series using automated software (Nikon Elements), then maintained for ensuing sections. Sections were photographed using a CCD HD color camera (Nikon DsFi2). Cell counts were obtained using automated software (Nikon Elements, see below).

3.2.3 Immunochemistry

To minimize background fluorescence and fading, GFP(+) GIN and G42 cells were stained using anti-GFP immunochemistry (1°: rabbit anti-GFP, #A11122 Life Technologies, 1:10,000 dilution, 24 hours, 20°C; 2°: donkey anti-rabbit Biotin-SP Affinipure # 711-065-0152, Jackson Immunoresearch Laboratories, 1:100 dilution, 1 hr, 20°C) followed by avidin-biotin-peroxidase reaction (Elite Kit, Vector Laboratories) using 3,3'-diaminobenzidine (DAB). Parvalbumin expressing cells were immunostained using rabbit anti-parvalbumin (1°: PV27, Swant, 1:1000, 48 hrs, 4°C; 2°: donkey anti-rabbit Alexa-fluor-488, #A21206 Life Technologies, 1:500, 3 hrs, 20°C). Somatostatin expressing cells were immunostained using rabbit anti-somatostatin (1°: Ab20067 Immunostar, 1:500, 48 hrs, 4°C; 2°: donkey anti-rabbit Alexa-fluor-488, #A21206 Life Technologies, 1:500, 3 hrs, 20°C). Prior to staining, tissue was blocked in 10% normal donkey serum (1 hour). Specificity controls for the secondary antibodies were performed by excluding the 1° antibody in a small number of sections (n=4). Only faint neuropil fluorescence was visible and no cell bodies were stained.

3.2.4 In vitro slice preparation

Brain slices of anterior piriform cortex (APC) were prepared from mice aged P18-30. The mice were anesthetized with isoflurane and decapitated. The brain was removed from the skull and immersed in ice cold oxygenated (95% O2-5% CO2) ACSF (in mM: 125 NaCl, 2.5 KCl, 25 NaHCO3, 1.25 NaH2PO4, 1.0 MgCl2, 25 Dextrose, 2.5 CaCl2) (all chemicals from Sigma, USA unless otherwise stated). Parasagittal slices (300 µm) were made using a vibratome (Leica

Biosystems) in ice cold ACSF. The slices were transferred to warm ACSF (37°C) for 30 min and then rested at 20-22°C for 1 hour prior to recording (31-35°C).

3.2.5 Electrophysiology

Whole cell, voltage and current clamp recordings were performed using a MultiClamp 700B amplifier (Molecular Devices, Union City, CA). Data were low pass filtered (4 kHz) and digitized at 10 kHz using an ITC-18 (Instrutech) controlled by custom software (Recording Artist, https://bitbucket.org/rgerkin/recording-artist) written in IgorPro (Wavemetrics). Recording pipettes (4-10 MΩ) were pulled from borosilicate glass (1.5 mm, outer diameter) on a Flaming/Brown micropipette puller (Sutter Instruments). The series resistance (<22 MΩ) was not corrected. The intracellular solution consisted of (in mM) 130 K-gluconate, 5 KCl, 2 MgCl2, 4 ATP-Mg, 0.3 GTP, 10 HEPES, and 10 phosphocreatine, 0.05% biocytin. In a subset of pyramidal cells, a Cs-gluconate internal solution was used (100 Gluconic Acid, 5 MgCl2, 0.2 EGTA, 40 HEPES, 2 ATP-Mg, 0.3 GTP, 0.05% biocytin, titrated to pH 7.2 with 50% Cs-OH). When IPSCs were recorded, 4.5 µM QX-314 was also added to the internal solution. Recordings were obtained from L2/3 pyramidal cells (PCs) as well as interneurons in lower L2 and L3. Neurons were visualized using infrared-differential interference contrast microscopy (IR-DIC, Olympus). PCs were identified using intrinsic properties and post hoc anatomical reconstruction (Neurolucida). In transgenic mice, interneurons were targeted using red (tdTom) or green (GFP) fluorescence. For studies involving ChR2 stimulation, neurons were targeted based on the absence of yellow fluorescent protein (YFP) fluorescence. In the absence of fluorescence, neural identification was based on intrinsic properties. In all neurons, the input resistance (R_{in}), time constant (τ_m), and sag due to I_h current, were assessed in current clamp using a series of

hyperpolarizing and depolarizing current steps (-50 pA to 50 pA, 1 s duration). Input resistance was the slope of a linear fit of the relationship between the change in voltage and current amplitude for steps between (-50 and 50 pA in 10 pA increments). Membrane time constant was determined based on the monoexponential fit of the falling phase of the voltage response to a -50 pA current injection. Sag was measured as the difference in voltage between the onset (first 50 ms) and last 100 ms of a -50 pA step. To assess spike responses a series of depolarizing steps (1 s duration, 0-1000 pA, 100 pA stepsize) was used. Rheobase was taken as the minimum current to elicit spike responses. Spike width was assessed at rheobase and taken as the average full-width at spike half-height. Interspike interval (ISI) analyses (adaptation ratio and CV) were conducted on spike responses to current injection 100 pA above rheobase. Adaptation ratio corresponded to the last ISI divided by the first ISI, while the CV of the ISI was the standard deviation of the ISI divided by the mean ISI.

3.2.6 Light stimulation

Blue light (λ=460-488 nm, GFP block, Olympus) for full-field optical stimulation was provided by metal halide lamp (200W, Prior Scientific) passed through the microscope objective (60x, immersion, Olympus). Based on our measurements, the light intensity at the tissue is estimated to be ~3-4 mW. Light pulses were controlled using a mechanical shutter (Sutter Instruments). Light intensity and duration (20 ms) was chosen to reliably evoke at least one spike in SST-cells although multiple spikes were frequently observed. This was advantageous because weak synapses that undergo short-term potentiation are more likely to be observed. Since these are inhibitory neurons and there is no evidence of depolarizing inhibition at threshold membrane potentials, polysynaptic responses are unlikely under these recording conditions.

3.2.7 Drug Application

The $GABA_A$ receptor antagonist, Gabazine (GZ, 40 µM in ACSF) was loaded into a regular patch pipette and locally applied using a gentle positive pressure (<1-5 s duration) from a 1 cc syringe by hand. GZ was applied within 20 µm of the soma of the recorded cell or in L1B directly above the recorded cell or at both locations simultaneously. Pressure was sufficient to minimally distort tissue in a region ~50 µm around the injection site but did not alter recordings in the absence of GZ. Slices were oriented such that bath flow was perpendicular to the somatodendritic axis of the pyramidal cell to minimize diffusion between somatic and dendritic application sites.

3.2.8 Data Analysis

All summary data is presented as the mean ± standard error (SE) apart from medians and quartiles (Q_1, Q_3) where noted in the text.

Cell counts: Neural densities were quantified as number of cells per mm^2 in regions of interest (ROI) within the ventral anterior piriform cortex (vAPC). Every other coronal section was analyzed spanning 600-1000 µm along the rostral-caudal extent of the APC. For each mouse, densities were averaged across 6-10 sections. To obtain total cell density, ROIs extended from L1A to the anterior commissure encompassing L1B, L2, L3, and when present, endopiriform (EP) areas. For laminar densities, ROIs corresponded to the entirety of each layer within vAPC. In sections from both SST-tdTom and PV-tdTom mice, the neuropil was sufficiently fluorescent to visualize L2 as densely packed dark voids corresponding to unlabeled neurons. These dark voids were more diffuse in L3. Endopiriform areas were difficult to

distinguish. In SST-tdTom mice, the L3/EP edge was defined by the transition from larger multipolar cells to smaller elongated tdTom(+) somas (Kowianski et al., 2004). This edge could not be discerned in PV-tdTom mice so counts in EP were not explicitly performed and L3 counts include EP. Counts were made in a single focus plane for each section at 4x magnification chosen to maximize the number of cells in focus (but see exception below). For fluorescent markers (tdTom or GFP) automated cell counts within a region of interest (ROI) were obtained based on fluorescence intensity and circularity using Elements Software (Nikon). Neurons that were immunostained and/or double-labeled (tdTom+GFP) cells were counted by hand within defined ROIs. Compared to PV immunostaining, somatostatin immunostaining was weaker, punctate and did not always fill the soma. For this reason, cell counts were performed at 20x magnification across a 20-30 µm z-stack (1 µm intervals, 2-3 ROIs per section). Two researchers independently verified all counts.

Cluster Analysis: Neurons were grouped on the basis of subthreshold and/or suprathreshold intrinsic properties using hierarchical clustering algorithm using Ward's method implemented in R (Free Statistics Software, Wessa.net (Wessa et al. 2011). Prior to clustering, all data was standardized to obtain z-values. For sequential clustering, defined groups of neurons were removed to enhance differentiation of remaining clusters. In these cases, z-values were recalculated using the remaining data set.

Analysis of inhibition: Electrophysiology traces of IPSCs are presented as the average across trials for individual neurons. IPSC strength was taken as the area (pA·s) under the IPSC. Average PSCs with minimum amplitude of 10 pA were included for analyses; smaller PSCs were not distinguishable from noise.

Statistics: Due to the nature of the data we used a number of statistical tests. Here we provide a justification for cases in which the conditions for Student's t-test or ANOVA are not met. For small sample sizes (<10) non-parametric Mann-Whitney U-tests (MWU) and Wilcoxon Signed Ranks tests (WSR) were used for unpaired and paired data respectively. For equal variances and multiple comparisons, we used ANOVA with post-hoc Tukey Test (ANOVA-Tukey). For multiple comparisons with unequal variance we used Welch's ANOVA (ANOVA-Welch). For groups with unequal variance and sample sizes, multiple comparisons of the distributions were made using the non-parametric, Kruskal-Wallis test (KW-test). The remaining statistical comparisons were made using parametric paired or unpaired Student's t-tests or ANOVA without correction. All statistical tests are indicated in the main text.

3.3 RESULTS

We used transgenic mouse lines to target either SST interneurons (GIN and SST-cre) or PV interneurons (G42, or PV-cre). Our initial goal was to cross SST-cre mice with G42 mice to investigate the inhibitory connectivity between SST and PV interneurons. However, these transgenic lines have not been previously characterized in piriform cortex, so we first investigated the anatomical distributions and electrophysiological properties of interneurons targeted in these lines. SST-cre or PV-cre lines were crossed with Ai14 mice to express the red fluorescent protein, tdTomato, in SST and PV- cells (denoted: SST-tdTom and PV-tdTom). The GIN and G42 lines express GFP in SST and PV cells respectively. To minimize background

fluorescence and fading we used anti-GFP immunochemistry to stain GFP(+) cells in tissue from GIN and G42 mice (see methods).

3.3.1 Distribution of SST and PV interneurons in piriform cortex

First we investigated the total density (across layers) as well as laminar densities of tdTom(+) cells in SST-tdTom mice. We focused on the region of ventral anterior piriform cortex (APC) that contains the lateral olfactory tract (L1A). As expected based on immunohistochemistry studies (Suzuki and Bekkers, 2010b), we found a high density (100 ± 5.83 cells/mm2, n=6 mice) of SST-tdTom cells in APC (Figure 7A). Co-labeling with an antibody to somatostatin revealed that the majority, 75 ± 3% of SST-tdTom cells express somatostatin (SST(+)) consistent with previous findings (Nassar et al., 2015) (Figure 1B, n=7 ROIs, from 2 mice see methods). It should be noted that somatostatin immunolabeling varied in intensity across cells and may underestimate true co-labeling. The highest densities of SST-tdTom (n=4 mice, Figure 7A,C1, E) and SST(+) co-labeled cells (84 ± 2%) were found in L3 and endopiriform (EP). A number of other patterns were also apparent. First, a small number of SST-tdTom cells lined the border between L1A and L1B (Figure 7A). Second, apart from a cluster of cells at the dorsal edge of the LOT near the rhinal fissure (asterisks, Figure 7A, C1), the density of SST-tdTom cells was relatively low. Further, the percentage of SST(+) co-labeled cells was lowest in L2 (41± 5%). And finally, there was strongly fluorescent neuropil in L1B and L2/3 consistent with dendritic and/or axonal and terminal projections from SST-tdTom cells (Figure 7C2, D). It has been suggested that SST-cells primarily inhibit dendrites while PV-cells inhibit somas. Since L1B is the location of the proximal apical dendrites of pyramidal cells, we compared the intensity of this fluorescence between SST-tdTom and PV-tdTom mice. To control for variations in fluorescence

across sections and animals, average intensity over a small area (140 μm2) in L1B was normalized by the average intensity of a comparable area in the L1A. Only tissue from animals with low background fluorescence in L1A was used (SST-tdTom: n=3 mice, PV-tdTom: n=2 mice). Normalized intensity values (6-8 sections per animal) were compared between all animals. We found that L1B fluorescence did not significantly differ within SST-tdTom or PV-tdTom groups but was significantly higher in SST-tdTom mice compared to PV-tdTom mice (* $p<0.05$, ** $p<0.01$; ANOVA-Welch Figure 7F) These findings suggest SST-cells are poised to mediate dendritic inhibition of pyramidal cells in L1B.

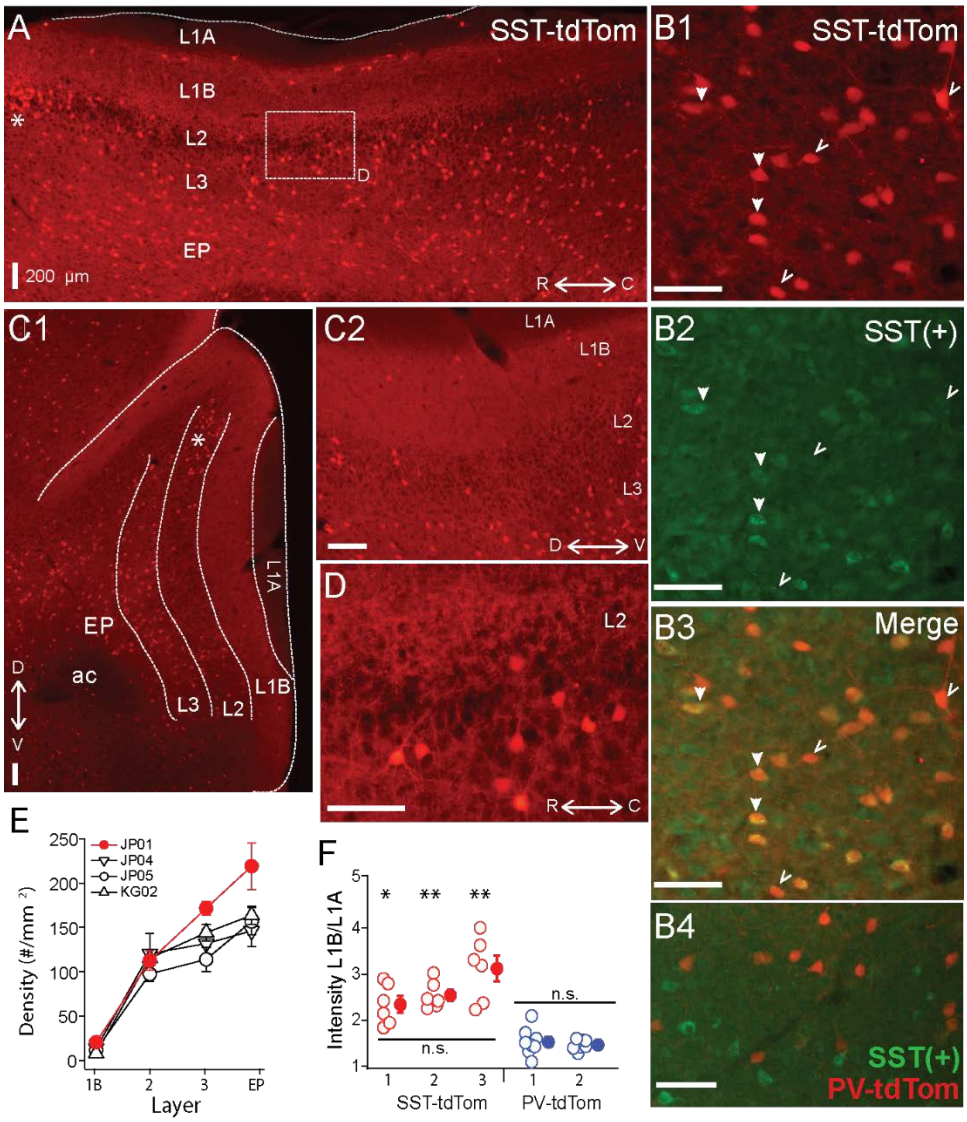

Figure 7. Distributions of SST-cre cells in anterior piriform cortex.

(A) Sagittal section of anterior piriform cortex from an SST-tdTom mouse (mouse #JP01). Lamina are labeled (L1A, L1B, L2, L3, EP), asterisk (*) corresponds to dorsal/rostral L2 density of SST-cre cells. 4x magnification, Scale bar: 200 µm. (B) Co-expression of SST-tdTom cells with anti-somatostatin immunolabeling (SST(+), green). SST(+) cells are shown with filled arrows while SST(-) cells are labeled with open arrows (20x, scale bars 100 µm) (B1) SST-tdTom expression (red) (B2) SST-immunolabeling (green) (B3) Merge of B1, B2 showing co-expression (yellow). (B4) Minimal overlap of PV-tdTom (red, mouse KM04) and SST(+) cells (green). (C1) Coronal section from opposite hemisphere of mouse #JP01 shown in (A). Labels as in A, 4x magnification, Scale bar: 200 µm. (C2) Enlarged (10x) area of B1

showing tdTom fluorescence in L1B corresponding to projections from SST-cells. Scale bar: 200 µm. (D) Enlarged (20x) area of box shown in A. Scale bar: 100 µm. (E) Average density of SST-cells in each layer for four different mice from two different litters (denoted JP, KG). Points shown in red correspond to data from mouse #JP01 shown in panels A and B1-3. (F) Ratio of fluorescence in L1B:L1A for three SST-tdTom mice and two PV-tdTom mice. Each point corresponds to one coronal section. The fluorescence ratio did not significantly differ between SST-tdTom mice but was significantly higher in individual SST-tdTom versus PV-tdTom mice (* $p<0.05$; ** $p<0.01$, ANOVA-Welch). Abbreviations: ac: anterior commissure

In neocortex, GIN mice express GFP in a few subtypes of SST-cells including dendrite targeting Martinotti cells in superficial L2/3 (Ma et al., 2006; McGarry et al., 2010). When we analyzed the distributions of GIN cells in piriform cortex (n=4 mice) we found an exceptionally low density of GFP(+) GIN cells (6.21 ± 2.23 cells/mm2) compared to SST-tdTom cells in piriform cortex (100 ± 5.83 cells/mm2) or GIN cell density in neocortical somatosensory cortex (31.4 ± 9.51 cells/mm2, Figure 8A,D). We crossed a heterozygous SST-tdTom mouse with a GIN mouse to quantify double labeling between SST-tdTom and GIN cells. While GIN cells co-localized with SST-tdTom cells, double labeling was sparse in APC, typically only 1-4 cells per section or (1%) of SST- tdTom cells (n=2 mice, Figure 8B,E). Double labeling was much higher in neocortex (9%) (Figure 8C, E). These overlap percentages were lower than expected based on raw counts of GIN and SST-tdTom cells in APC (~6%) or previous reports in neocortex (15-20%, (Ma et al., 2006)). The most likely explanation is that the raw GFP fluorescence in GIN cells was weak and difficult to distinguish from background compared to DAB stained tissue. Nonetheless, these findings suggest that SST-cells labeled in the GIN line (i.e. Martinotti cells) are only a very small subset of all SST-cells in APC.

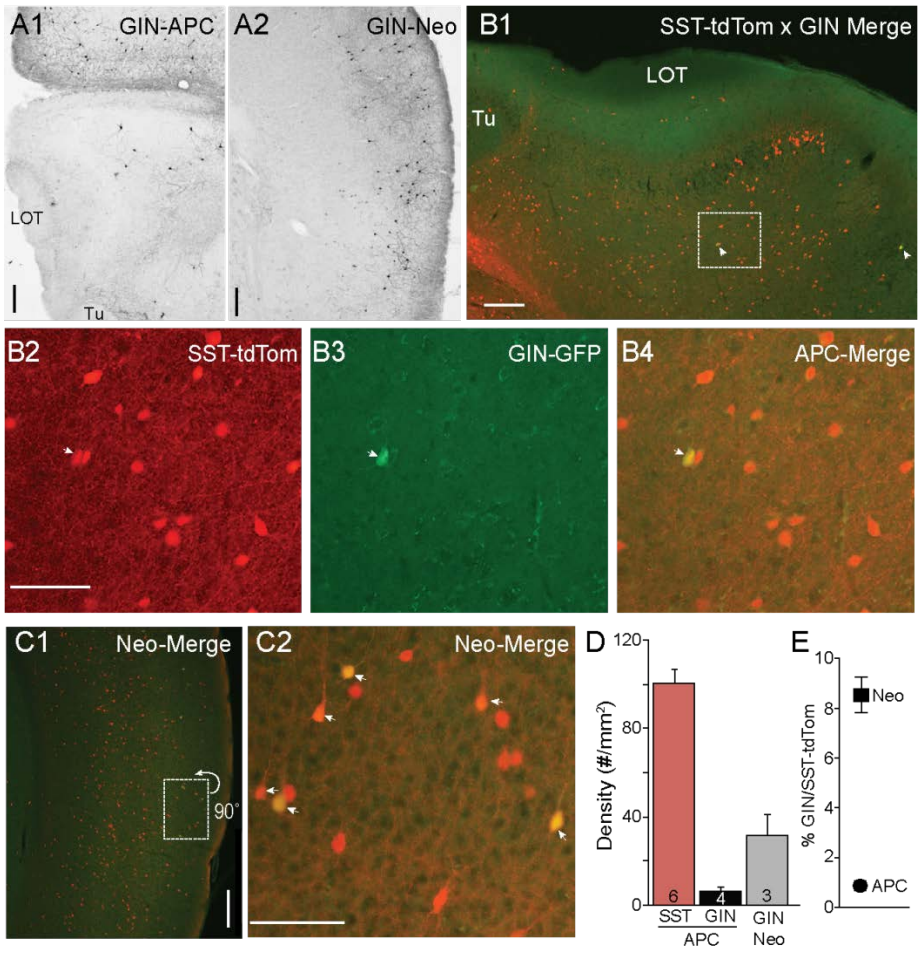

Figure 8. Minimal co-expression of GFP and tdTom in GIN and SST-cre lines.

(A) GFP (+) cells using anti-GFP antibodies and DAB (see methods) in the sections of anterior piriform cortex (A1) and neocortex (A2) from a GIN mouse. 4x magnification, Scale bar: 200 µm. B) Merged tdTom (SST-cre) and GFP (GIN) fluorescence in APC from an SST-tdTom-GIN mouse. White arrows indicate co-labeled cells. (B1) 4x magnification, Scale bar: 200 µm. (B2-B4) Region shown in B1 enlarged (20x, scale bar 100 µm) in for SST-tdtom cells (red B2), GIN cells (GFP, B3) and merged (B4) to show double labeled cells (yellow). Very few SST-tdtom cells double label with GIN cells in APC. (C1) Merged tdTom (SST-cre) and GFP (GIN) fluorescence in neocortex from the same SST-tdTom-GIN mouse as in B. (C2) Region shown in C1, enlarged (20x, scale bar 100 µm) showing a higher proportion of SST-tdTom cells co-label with GFP(+) GIN cells (yellow, arrows) in neocortex. Scale bars as in B. (D) Summary plots showing the average density of SST-tdTom cells in APC compared to GIN cells in APC

and Neocortex. (E) Percent overlap between SST-tdTom and GIN cells in APC and neocortex. Abbreviations: Tu: olfactory tubercle

Next we turned our attention to transgenic lines targeting parvalbumin interneurons. In PV-tdTom mice (n=5) the densities and laminar distributions of tdTom(+) cells were also consistent with previous reports (Gavrilovici, D'Alfonso, and Poulter 2010; Suzuki and Bekkers 2010a). Overall, the average density of PV-tdTom (48.2 ± 2.96 cells/mm2, n=5 mice) cells was significantly lower than SST-tdTom cells (100 ± 5.83 cells/mm2, n=6 mice p:0.008, MWU-test). The majority of PV-tdTom somas were found at the L2/3 border and extended to deep L3. A small number of tdTom(+) cells were also consistently found at the L1A/B border (Figure 9A,B, n=4 mice). Diffuse fluorescence corresponding to axons and dendrites was most prominent L2/3 (Figure 3A1,2). Within L2/3, punctate labeling was visible surrounding darker voids (unlabeled somas) consistent with basket-like synapses (Figure 9A3). Finally, PV-tdTom cells sent fewer axonal projections to L1B than SST-cells (Figure 7D, 3A1-3).

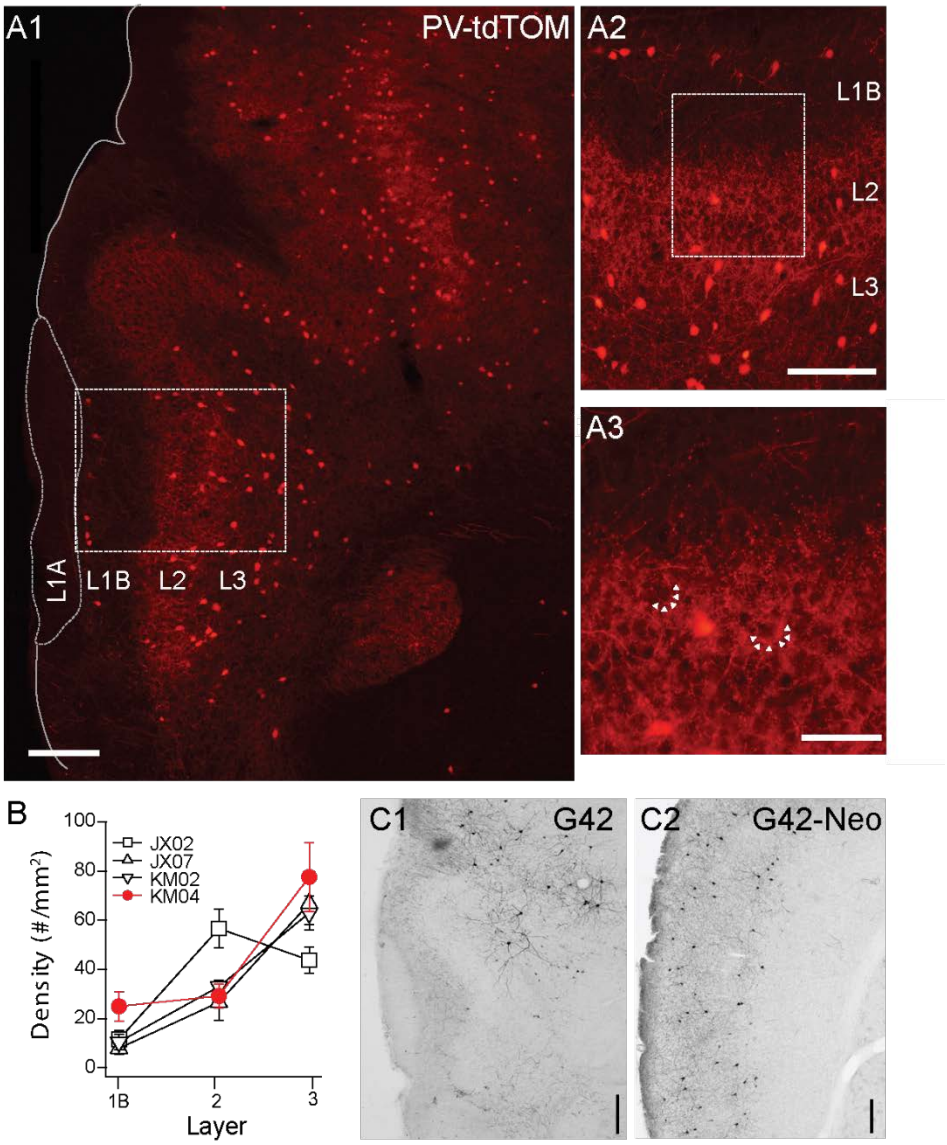

Figure 9. Distributions of PV-cre cells in anterior piriform cortex.

(A1) Coronal section from a PV-tdTom mouse (KM04). 4x magnification, Scale bar: 200 µm. (A2) Enlarged (10x) area of A1 showing a lack tdTom fluorescence in L1B but strong fluorescence in L2. Scale bar: 100 µm. A3) Enlarged (20x) area of box shown in A2. Note punctate tdTom fluorescence outlining dark voids (arrows) suggestive of baskets. Scale bar: 50 µm. B) Average density of PV-cells in each layer for four different mice from two different litters (denoted JX, KM). Points shown in red correspond to data from mouse KM04 shown in panels A1-3. (C) Sparse anti-GFP labeling in coronal sections from a G42 mouse (C1) APC (C2) neocortex. 4x magnification, Scale bar: 200 µm.

Surprisingly, GFP(+) neurons in the G42 line differed in nearly every aspect from cells in the PV-cre line. First, the density of GFP(+) G42 cells was very low in piriform cortex (11.34 cells/mm2, n=1 mouse, Figure 9C1) compared to PV-tdTom cells (48.2 ± 2.96 cells/mm2, n=5 mice, Figure 3A) or G42 cells in neocortex (35.67 cells/mm2, Figure 9C2). Second, the majority of G42 cells were located deep in L3 or endopiriform areas. This was true both in histological sections and for GFP(+) neurons recorded from G42 mice (data not shown). Since G42 mice are heterozygous, there is low probability of obtaining a triple transgenic mouse (approximately <1/litter) from crosses of G42 and PV-tdTom mice. Thus, we were unable ascertain the overlap between G42 cells and PV-tdTom populations. However, given the sparseness and location of G42 cells we expect that G42 cells represent a very small subpopulation of PV cells in piriform cortex.

Recent studies have suggested that the SST-cre transgenic line is vulnerable to off-target recombination and that approximately 6-14% of neurons express parvalbumin rather than somatostatin (Hu et al., 2013; Pfeffer et al., 2013; Nassar et al., 2015). We analyzed anti-parvalbumin immunostaining (PV(+)) in tissue from one PV-tdTom mouse (KM04 Figure 10A) and two SST-tdTom mice (JP04, Figure 4A, and IY05) to quantify co-labeling between tdTom(+) and PV(+) cells in the two cre-lines. In KM04 and JP04, the average densities of PV(+) cells (42.1 ± 7.72, 39.5 ± 4.75 cells/mm2) were comparable to the average density of PV-tdTom cells reported above, but there were fewer PV(+) cells in IY05 (19.8 ± 3.08) (Figure 4C). As expected for the PV-cre line, 95 ± 3% of tdTom(+) cells were PV(+) in APC of PV-tdTom mice (KM04, Figure 10A,D). In the SST-tdTom animals, 6 ± 1% (IY05) and 16 ± 2% (JP04) of

tdTom(+) cells were PV(+) (Figure 10B, D). Since a majority of recorded interneurons were in deep L2 and L3, we also investigated co-expression by layer in SST-cre mice (Figure 10E). Co-expression was variable in L1 (IY05: 18 ± 2%, JP04: 47 ± 9%) likely due to the low densities of SST and PV interneurons in this layer. The percentages of PV(+), SST-tdTom cells in L2 (IY05: 4 ± 1%, JP04: 10 ± 3%), L3 (IY05: 10 ± 1%, JP04: 15 ± 2%), and EP (IY05: 10 ± 2%, JP04: 15 ± 3%) were comparable to values reported for L4 of neocortex (Hang Hu, Cavendish, and Agmon 2013). Given the lower densities of PV cells in APC, a higher average proportion of PV(+) cells co-expressed tdTom in SST-cre animals (IY05: 57 ± 5%, JP04: 55 ± 4%) and co-expression varied across layers (Figure 10F). We also investigated whether PV-tdTom cells co-express somatostatin using anti-somatostatin immunolabeling. We found 6 ± 1% of PV-tdTom cells were SST(+) (Figure 7B4, n=3 sections from KM04). Altogether, these findings suggest the potential for off-target recombination in PV-cells in the SST-cre line in APC is comparable to other cortical areas. In the following sections, we will discuss variable degrees of influence off-target recombination may have on our results.

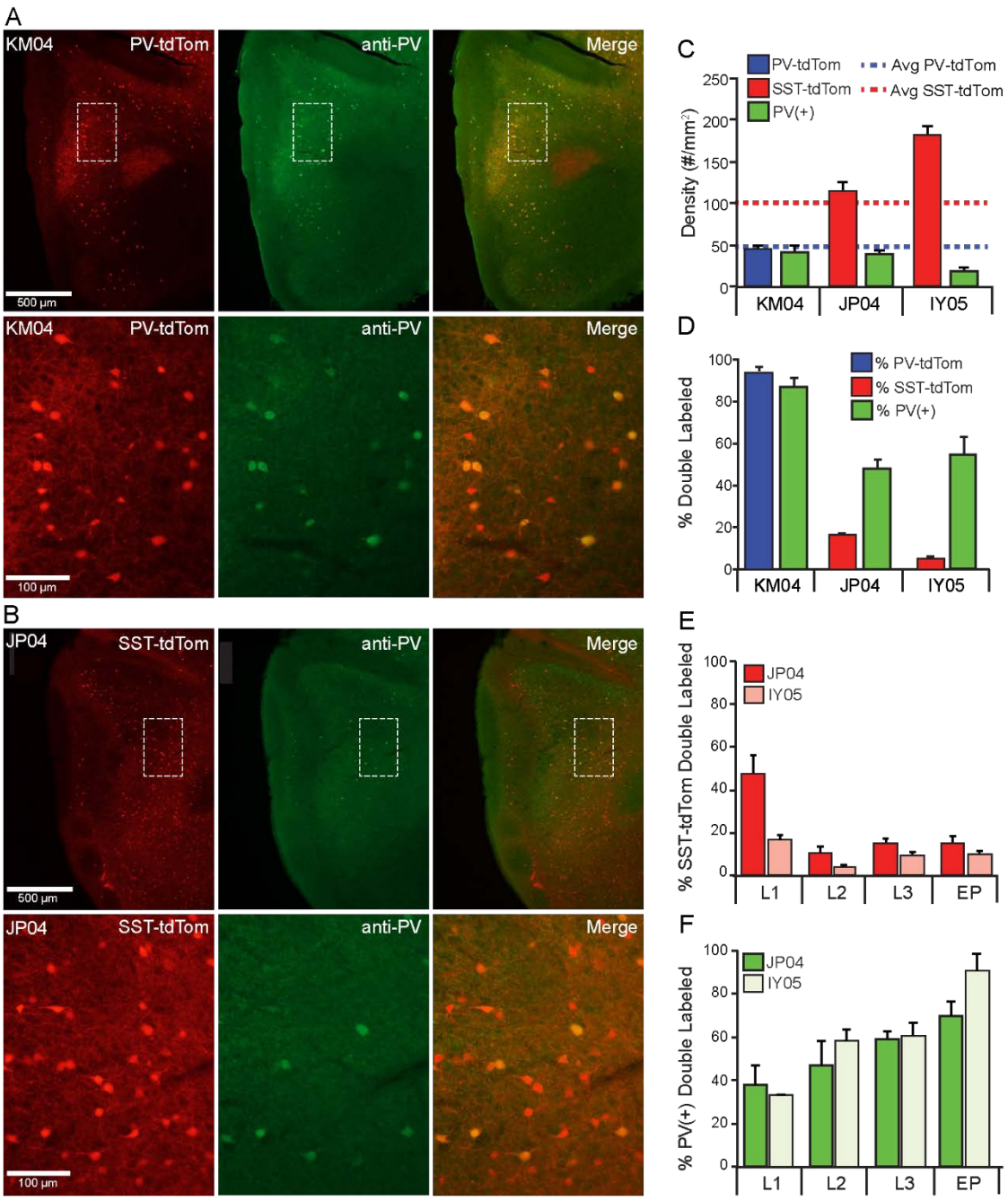

Figure 10. Co-expression of parvalbumin and tdTomato in PV-Cre and SST-Cre lines.

Anti-parvalbumin immunostaining in (A) PV-tdTom mouse (KM04) and (B) SST-tdTom mouse (JP04). Sections from both animals were stained in the same experiment. Upper panels show the APC (4x magnification), lower panels show area indicated by dashed box at higher magnification (20x) Left panels: tdTom(+) neurons (red) in the PV-tdTom (A) or SST-tdTom (B) animals; middle panels: PV(+) interneurons labeled with GFP (green); and right panels: co-expression tdTom(+) and PV(+) cells (yellow).

(C) Density of tdTom(+) cells in the PV-tdTom (KM04, blue) and two SST-tdTom (JP04, red; IY05, pink) mice. Dashed lines correspond to average densities of tdTom(+) cells reported for all SST-tdTom (red) and PV-tdTom (blue) mice. The green bars correspond to the density of PV(+) cells in each mouse. (D) Co-expression of PV(+) and tdTom(+) as a percentage of tdTom(+) cells in PV-tdTom (blue) or SST-tdTom (red, pink) mice or as a percentage of PV(+) cells (green) in each mouse. (E) Co-expression of PV(+) and tdTom(+) as a percentage of tdTom(+) cells in SST-tdTom mice (JP04 red, IY05 pink) by layer. F) Co-expression of PV(+) and tdTom(+) as a percentage of PV(+) cells in SST-tdTom tissue (JP04 dark green, IY05 light green) by layer.

3.3.2 Electrophysiological properties of interneurons in piriform cortex.

SST interneurons are commonly described as regular spiking (RS) or low-threshold spiking (LTS) while PV-interneurons are typically fast spiking (FS). However, a variety of spiking phenotypes, including FS, have been described for SST-cells (Y. Ma et al. 2006; McGarry et al. 2010; Nassar et al. 2015). We endeavored to classify SST-cre cells in piriform cortex based on intrinsic subthreshold and suprathreshold electrophysiology. We used a hierarchical clustering algorithm to classify interneurons recorded in L3 from SST-cre, PV-cre, GIN and G42 lines.

Eight parameters were used for clustering- input resistance (Rin), membrane time constant (τm), sag, rheobase, spike width, max firing rate, adaptation ratio (AR) and coefficient of variation of the interspike interval (CVISI) (see Methods, Figure 11A). Initial statistical analysis of the intrinsic properties between the four cell classes (ANOVA-Tukey, Figure 5A) revealed that GIN and G42 cells differed from cells recorded in the cre-lines but did not distinguish between SST-cre and PV-cre cells. Following this, the interneurons were divided into two main branches and four clusters (Labeled 1-4, Figure 11B) using Ward's clustering algorithm. The first branch consisted of PV-cre cells and a majority of SST-cre interneurons while GIN and G42 neurons

comprised the second branch (Figure 11B). SST-cre neurons showed the greatest diversity of responses and were found in all four clusters. G42 cells were the most homogeneous and all-but-one neuron comprised a single cluster (#4). Thus, we performed additional clustering analyses the three clusters (#1-3) that encompassed the majority of SST-cre cells and excluded G42 cells. For each additional clustering analysis, z-scores were recalculated with respect to the members involved. In clustering analyses that included both the full data set (Figure 5B) and the three selected clusters (Figure 11C), a subset of SST-cre neurons consistently clustered with GIN cells. Like GIN cells, these neurons could be classified as regular spiking (RS, Figure 11E) and had intrinsic properties that, except for spike width, did not significantly differ from GIN cells (Table 1). Since these neurons also significantly differed from the remaining SST-cre cells, we denoted these cells as RS SST-cre cells and removed them, along with GIN cells from additional clustering analyses. The electrophysiological responses of the remaining 13/19 SST-cre cells were indistinguishable "by eye" from those of PV-cre cells (Figure 11F,G). Both classes showed fast-spiking (FS) responses to depolarizing steps and had maximum firing rates near 200 Hz. However, direct statistical comparison of intrinsic properties between FS SST-cre cells and PV-cre cells revealed significant differences between these classes (Table 1). Further, cluster analysis based on the 8 parameters produced two clusters with minimal misclassification (n=5/25, Figure 11D, left). Neurons clustered in the predominantly PV group (including SST-cre cells) were more likely to exhibit stuttering or irregular FS bursts characterized by a significantly greater CVISI (1.3 ± 0.3) than the SST group (0.13 ± 0.03, p: 0.002, t-test) which exhibit tonic-FS responses. Finally, we performed one final cluster analysis using just subthreshold parameters (Rin, τm and sag) that are available under conditions when spiking is blocked. Surprisingly, three parameters were sufficient to produce two clusters corresponding to

PV and SST cells, with just 2 misclassified SST-cre cells (Figure 11D, right). Sag was the factor that differed most significantly between SST-cre (0.48 ± 0.08 mV) and PV-cre (0.10 ± 0.02 mV, p:0.0002, unpaired t-test) interneurons.

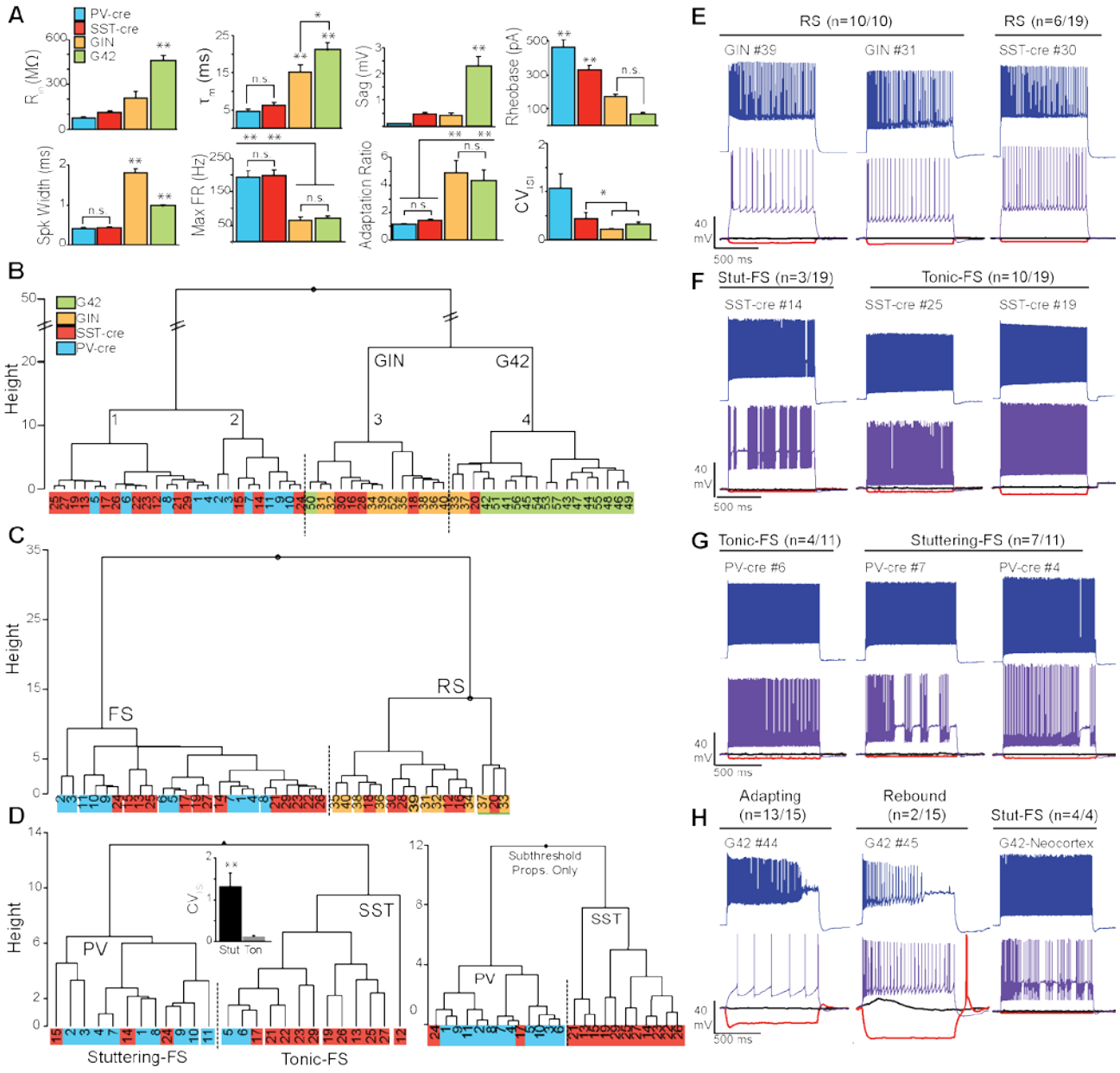

Figure 11. Electrophysiological properties SST and PV cells in Cre, GIN and G42 lines.

(A) Comparisons of subthreshold (Rin: input resistance; τm: time constant; Sag) and suprathreshold electrophysiological properties (Rheobase, spike width, maximum firing rate, adaptation ratio, and CVISI: coefficient of variation of the interspike interval) in target neurons from anterior piriform cortex in SST-cre (red), PV-cre (blue), GIN (yellow) and G42 (green) mice. Statistical significance assessed using ANOVA-Tukey for multiple comparisons (* $p<0.05$; ** $p<0.01$, n.s.: not significant). (B) Clustering of all interneurons using the 8 electrophysiological parameters in A. (C) Clustering of SST-cre cells (red) as fast

spiking (FS) with PV-cre (blue) or regular spiking (RS) with GIN (yellow) cells using 8 parameters, in the absence of G42 cells. (D) In the absence of RS cells, FS cells cluster as either PV-cre or SST-cre with minimal error (5 cells) using 8 parameters (left). CVISI (inset) significantly differs between stuttering FS-cells (mainly PV) and tonic FS cells (mainly SST) ($p<0.01$, unpaired t-test). SST-cre and PV-cre cells cluster with even less error (right, 2 cells) when only 3 subthreshold properties (Rin, τm and Sag) are used. (E) Examples of RS SST cells in SST-cre and GIN mice. Numbers correspond to individual cells in clustering diagrams B-D. (F) Examples of FS SST-cre exhibiting both stuttering (Stut-FS) and tonic-FS responses. (G) Examples of FS PV-cre cells exhibiting both stuttering (Stut-FS) and tonic-FS responses. (H) Left: Examples of G42 cells recorded in APC showing unusual adapting and/or rebound responses. Right: Example of G42 cell recorded in neocortex showing classic stuttering-FS response.

Table 1. Intrinsic properties of identified interneurons in SST-Cre, PV-Cre, GIN, and G42 transgenic lines.

SST-cre interneurons were separated according to whether they clustered with regular spiking (RS) GIN cells or fast spiking (FS) PV-cre cells. Statistical comparisons of the mean +/- SE were made between SST-cre cells and GIN cells in the RS cluster and between SST-cre cells and PV cells in the FS cluster. Significant differences at a $p<0.05$ level are indicated in bold and $p<0.01$ are bold-italicized (unpaired t-tests). The mean +/- SE values are also listed for G42 cells in anterior piriform cortex (APC) and G42 cells in neocortex but not statistically compared due to the low sample size of neocortical cells. Abbreviations and units: R_{in}: input resistance (MΩ), τ_m: time constant (ms), Sag (mV), Rheo: rheobase (pA), SW: Spike width (ms), Max FR: maximum firing rate (Hz), AR: adaptation ratio, and CV_{ISI}: coefficient of variation of interspike intervals.

Cluster	Type	N	R_{in}	τ_m	Sag	Rheo	SW	MaxFR	AR	CV_{ISI}
RS	SST-cre	6	174± 47.5	12.± 2.01	0.49± 0.16	200 ± 51.6	1.14± 0.19	72.0± 21.5	4.33± 1.03	0.56± 0.22
	GIN	10	206± 46.1	15.1± 2.13	0.41± 0.13	170± 21.3	1.80± 0.13	65.3± 6.96	4.86± 0.99	0.21± 0.03
FS	SST-cre	13	113± 11.3	6.22± 0.59	0.48± 0.08	330± 28.6	4.22± 0.02	199± 16.9	1.44± 0.10	0.43± 0.16
	PV-cre	11	74.0± 7.93	4.65± 0.39	0.10± 0.02	463± 40.9	0.40± 0.02	193± 19.5	1.17± 0.07	1.06± 0.39
G42	G42 APC	17	456± 39.1	21.3± 1.93	2.31± 0.36	70.6± 11.7	1.00± 0.05	71.8± 10.0	4.33± 0.93	0.31± 0.06
	G42 Neo	4	63.8± 3.83	4.25± 0.48	0.16± 0.12	566± 33.3	0.36± 0.07	224± 19.2	1.33± 0.15	0.46± 0.34

Could misclassified SST-cre cells be due to off-target recombination in PV(+) cells? The percentage of misclassified SST-cre cells is ~10-16% (~2-3 cells of 19, Figure 5D). Given that we randomly targeted SST-tdTom cells in L3, the chance of selecting a PV(+) cell is expected to be ~6-16% (Figure 4D). Thus, it is possible that these 'misclassified' cells may indeed be PV-cells.

To summarize, these findings demonstrate that somatostatin neurons in piriform cortex can exhibit RS responses (n=6/19) similar to GIN cells as well as FS-tonic (n=10/19) and FS-stuttering (n=3/19) responses like PV cells. Moreover, FS SST-cells are more frequently recorded (~70%) than RS cells (~30%) in piriform cortex. The similarity between FS SST cells and PV interneuron responses can make these classes difficult to distinguish in the absence of fluorescent markers. The prevalence of stuttering-FS responses in PV-cells over tonic-FS patterns in SST-cells suggests that firing pattern may be useful in this regard. However, given that SST-cells are far more likely to exhibit sag responses that are greater than 0.25 mV, this criterion may be a better indicator of SST-cells.

For completeness, we also evaluated the intrinsic properties of G42 cells in piriform/endopiriform areas. Intriguingly, despite the premise that these cells express PV, the intrinsic properties differed significantly from other cell classes in APC (PV-cre, SST-cre, GIN) as well as G42 cells recorded in neocortex of the same slices (Figure 11H). These G42 neurons are characterized by exceptionally high input resistance (Rin: 456 ± 39 MΩ), time constant (τm: 21 ± 2.0 ms), Sag (2.3 ± 0.4 mV) and spike frequency adaptation (AR: 4.3 ± 0.9) (Figure 11A,H, Table 1). This suggests that G42 neurons form a cluster that is highly distinct from PV-cre cells

in APC that are characterized by low Rin (75 ± 8.0 MΩ); τm (4.7 ± 0.4 ms); Sag (0.1 ± 0.02 mV) and AR (1.2 ± 0.07). Further, we did not record any PV-cre cells in L2/3 of APC with properties resembling G42 cells. These findings suggest that G42 cells represent a small, highly unique subgroup that are not representative of the majority of PV cells in APC. Thus, we abandoned crosses of G42 and SST-cre lines as a method to assess inhibition of PV-interneurons by SST-cells.

3.3.3 SST-cells broadly inhibit L2/3 interneurons

To investigate inhibition mediated by SST-cells, we crossed SST-cre mice with Ai32 mice to express ChR2 and yellow fluorescent protein (YFP) in SST cells (SST-ChR2). We used brief flashes of blue light (see Methods) to evoke action potentials in SST-cells while recording IPSCs in postsynaptic YFP(-) interneurons in lower L2 and L3. To investigate whether SST-mediated inhibition differs between interneuron subtypes in piriform cortex, we clustered YFP(-) interneurons based on the intrinsic properties available (Rin, τm and Sag) in the presence of the sodium channel blocker, QX-314. We also included PV-cre cells (n=9) recorded with QX-314 as benchmark neurons in the clustering analysis.

Clustering analysis produced two main branches. The first branch consisted of two clusters of interneurons with low Rin (<200 MΩ) and Sag (<0.30 mV) values (Group 1 (G1), G2; Table 2, Figure 12A, B). Since nearly all of the benchmark PV-cre cells were found in G1, we putatively identified interneurons in this cluster as PV-cells (pPV). Moreover, G1 neurons differed significantly from G3-5 interneurons in many intrinsic properties (Figure 12B1-B3) suggestive of a distinct subclass. However, one PV-cre cell was found in G2 and the distributions of intrinsic properties of G2 did not significantly differ from G1 ($p>0.05$, KW test, Table 2).

Thus, we cannot rule out the possibility G2 also contains some PV cells. The second branch had 3 possible clusters (G3, G4, G5) consisting of interneurons with higher Rin (>200 MΩ) and/or Sag (>1.0 mV) values than G1 or G2 (Table 2, Figure 11A,B). Although we cannot definitively identify these clusters as distinct subtypes of interneurons, Groups 3-5 appear to be distinguished by unique combinations of low or high Rin, τm and Sag.

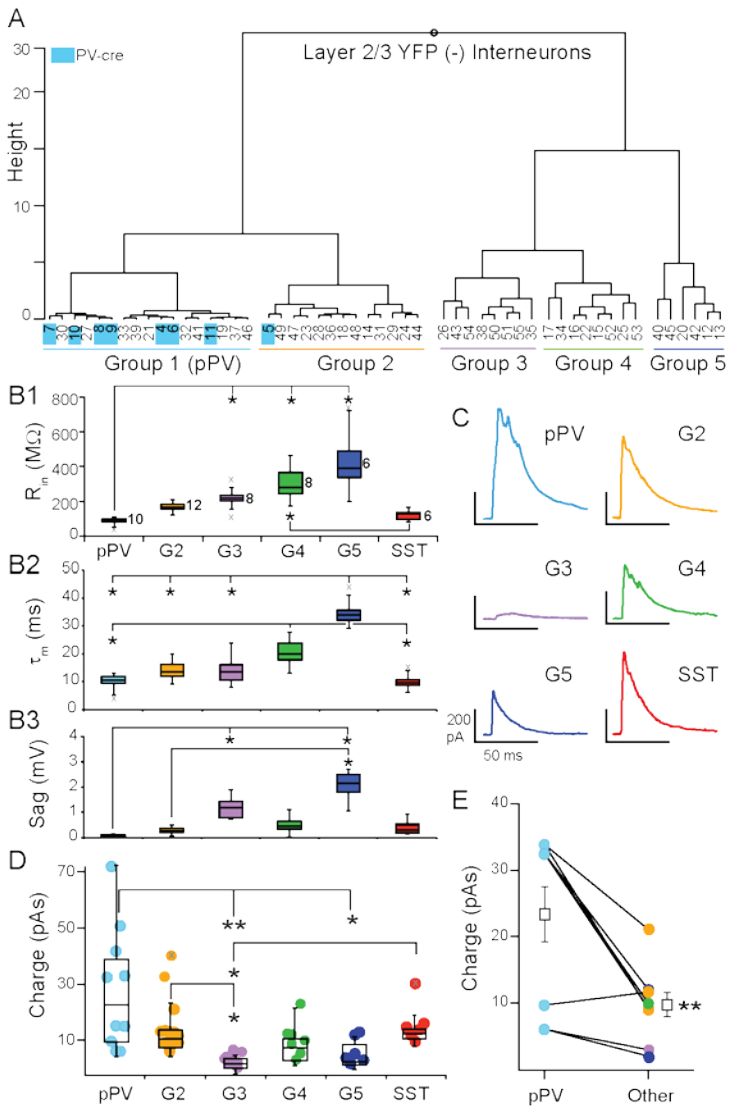

Figure 12. SST-mediated inhibition of L2/3 interneurons.

(A) YFP(-) interneurons were clustered according to subthreshold intrinsic properties into 5 groups (G1-5). Identified PV-cre cells (indicated in blue) were included as benchmark neurons and clustered almost exclusively with G1. Thus, we denote G1 interneurons as pPV (blue). (B) Comparisons of subthreshold property distributions presented as median and quartiles (Q1, Q3) between groups (pPV, G2-G5, and SST) (* $p<0.05$, KW-test) (B1) input resistance (Rin), (B2) time constant (τm) and (B3) Sag. Gray x's indicate outliers. (C) Representative IPSCs recorded in interneurons from each group. (D) Comparison of the distributions (median, Q1, Q3) of IPSC strength taken as the area under the IPSC (Charge, pA·s) across groups (* $p<0.05$, ** $p<0.01$, KW-test). (E) Mean IPSC strength was significantly greater in pPV cells compared to other interneurons (G2-G5) recorded in the same slice ($p<0.01$, WSR test).

Table 2 Intrinsic properties of interneurons that receive SST-mediated inhibition.

The mean +/-SE values for subthreshold intrinsic properties and IPSC strengths recorded in interneurons grouped according to the clusters shown Figure 5. Abbreviations and units as listed for Table 1.

Cluster	N	R_{in}	τ_m	Sag	IPSC (pA·s)
PV-cre	8	100 ± 13.7	7.38 ± 0.96	0.15 ± 0.03	N/A
G1 (pPV)	10	87.8 ± 6.52	9.90 ± 0.91	0.07 ± 0.02	28.2 ± 6.92
G2	12	166 ± 7.89	14.3 ± 1.01	0.28 ± 0.04	15.6 ± 3.16
G3	8	228 ± 20.2	22.5 ± 2.90	0.43 ± 0.118	12.7 ± 4.07
G4	8	218 ± 20.8	14.0 ± 1.81	1.18 ± 0.15	3.73 ± 0.80
G5	6	427 ± 75.4	34.8 ± 2.09	2.06 ± 0.25	6.39 ± 1.96
SST	6	120 ± 11.4	10.2 ± 1.08	0.56 ± 0.20	16.0 ± 2.97

Next we analyzed IPSC strength with respect to the groups of interneurons defined by cluster analysis (pPV, G2, G3, G4, G5) as well as identified SST-cells. Nearly all YFP(-) interneurons received inhibition (n=43, 95%) from SST-cells. In addition, we recorded IPSCs in a small number of YFP(+) SST-ChR2 cells (n=6/6). This latter finding was surprising because it has been previously reported that SST-cells do not inhibit each other in neocortex (Pfeffer et al. 2013). Representative IPSCs for each group are shown in Figure 12C. Since the IPSCs correspond to the inhibitory inputs from population of SST interneurons, strength was taken as the area (pA·s) of the IPSC (Figure 12D, Table 2). IPSC strengths were highly variable in pPV cells (G1) but showed reduced variability in the other interneuron groups. The distributions of IPSC strengths differed significantly between pPV cells (median (M) 23.8; quartiles (Q1) 11.0; Q3 39.8 pA·s) and G3 (M 3.73; Q1 2.66; Q3 5.66 pA·s, $p<0.01$ KW- test) and G5 interneurons (M 4.66; Q1 3.11; Q3 10.6 pA·s, $p<0.05$ KW- test). IPSC distributions also differed between G3 and G2 (M 12.3; Q1 9.10; Q3 15.3 pA·s, $p<0.05$ KW- test) and SST interneurons (M 14.3; Q1 12.4; Q3 15.6 pA·s, $p<0.05$ KW- test). Finally, the mean inhibitory strength differed significantly between G2 (15.7 ± 3.2 pA·s) and G3 (3.7 ± 0.8, p: 0.028, ANOVA-Welch), while the differences in means between G3 and pPV cells (28.3 ± 6.92 pA·s, p:0.051) and SST cells (16.4 ± 3.0, p:0.053) were barely insignificant. These findings suggest that the mean and variability of inhibitory strength mediated by SST-cells may depend on the target interneuron.

We explored other explanations for correlations between interneuron groups and IPSC strength. We tested the possibility that IPSC strength was correlated with input resistance regardless of interneuron group (Figure 13A). There was a weak, but significant, negative correlation (R=-0.36, p: 0.022, Pearson) between Rin and IPSC strength across all neurons. However, sequential removal of individual interneuron groups revealed this correlation was

strongly biased by pPV cells that have the lowest Rin and the highest IPSCs values. In the absence of pPV cells, there is no correlation between Rin and IPSC strength (r=-0.29, p: 0.107). To investigate whether trends in the data may be attributed to animal or litter we plotted IPSC strength chronologically by animal and litter (Figure 13B). We also plotted the mean strength (± 1SD) for all IPSCs (14.3 ± 14.1 pA·s). Altogether we recorded IPSCs in 49 interneurons in 28 slices from 18 animals from 8 litters over the course of 1 year. Nearly all IPSCs regardless of animal or litter fell within one SD of the mean IPSC strength. Of the outliers, 5/7 were recorded in pPV cells and did not depend on litter or animal. Further, the mean IPSC strength calculated without the values for any one litter did not differ from the overall mean (Figure 13C). Thus, there did not appear to be any significant trend in IPSC strength attributable to animal or litter.

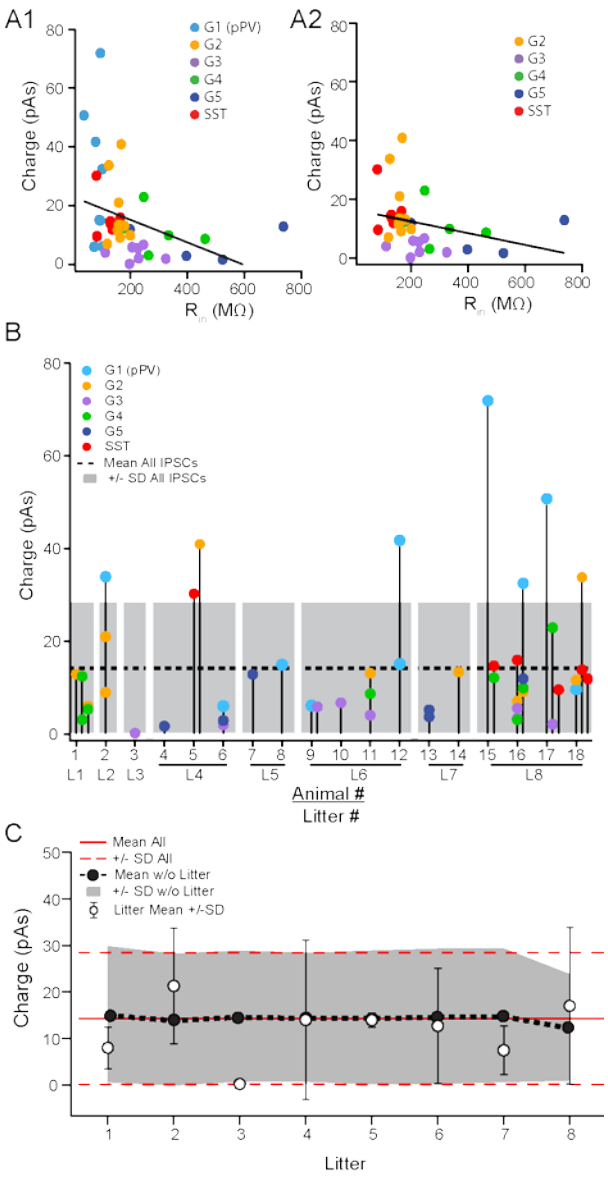

Figure 13. Other factors that could underlie differential inhibition by SST-interneurons.

A) IPSC strength is plotted against input resistance for each interneuron. The weak negative correlation is significant (R=-0.36, p: 0.022, Pearson) if pPV cells are included (A1) but not in their absence (A2, r=-0.29, p:0.107). B) IPSC amplitudes are plotted with respect to interneuron group (colored circles, See Fig. 6 main text), for recordings in the same slice (vertical connecting lines) or animal (numbered) or litter (L). Also plotted is the mean IPSC strength (dashed horizontal line) +/- one SD (shaded). C) The mean IPSC strength +/-SD for each litter (white circles). Black circles and shaded area correspond to mean IPSC

amplitude +/- SD calculated in the absence of the denoted litter. The overall mean +/- SD is also plotted (red lines). Removal of any one litter did not affect the overall mean or variance of the IPSCs.

All of our findings suggest that pPV cells are differentially inhibited by SST-cells. In 10/18 mice, multiple interneuron classes were recorded in a single animal. When pPV cells were one of the classes (n=6/10 animals), pPV cells received the strongest inhibition in 5/6 cases. In the remaining 4 animals, G2 neurons, which are the most similar to pPV interneurons, received the strongest inhibition. Within slice comparisons revealed that pPV cells received significantly stronger inhibition (23.3 ± 4.17 pA·s) than other classes (9.69 ± 1.84 pA·s, p: 0.01, WSR-test; 4 slices, n=8 comparisons, Figure 12E). While these findings are intriguing, they may be the most susceptible to off-target recombination in PV-cells, given that ~50% of PV(+) cells co-express tdTom in SST-tdTom mice (Figure 10F). Neocortical PV-cells can strongly inhibit each other but minimally inhibit other interneuron classes (Pfeffer et al. 2013). Although it is unlikely that the entirety of the inhibition received by pPV cells is mediated by PV-cell inhibition, it is possible that the additive effects of this inhibition could differentially contribute to the strength and variability of the population IPSCs. We attempted to quantify PV-to-PV cell inhibition but were unable evoke enough ChR2 current to elicit spike responses in PV-cells in slices from transgenic crosses (PV-cre x Ai32) or PV-ChR2 mice (S. Zhao et al. 2011). Thus, it would be important to verify these findings in the future using viral expression methodologies.

Nonetheless, we show that SST-cells provide inhibition to a majority of L3 interneurons and a variety of different interneuron classes in APC consistent with reports from other neocortical areas (Pfeffer et al. 2013; Jiang et al. 2015). Further, we find that SST-cells can

inhibit each other in APC. These findings suggest that SST-cells play an important role in regulating network inhibition during olfactory processing in piriform cortex.

3.3.4 SST-mediated inhibition of pyramidal cells

Finally, we investigated the SST-mediated inhibition of L2/3 pyramidal cells in SST-ChR2 mice. All pyramidal cells recorded (n=21) received inhibition from SST-cells. IPSCs were recorded at 0 mV using either K+-gluconate (n=11) or Cs+-gluconate (n=10) internal solutions. IPSCs were significantly stronger when using Cs+-gluconate (59.8 ± 8.59 pA·s) than K+-gluconate (15.5 ± 4.98 pA·s, p:0.0003, unpaired t-test; Figure 14A). Since Cs+-gluconate solutions improve space clamp, we use this solution in the remaining experiments.

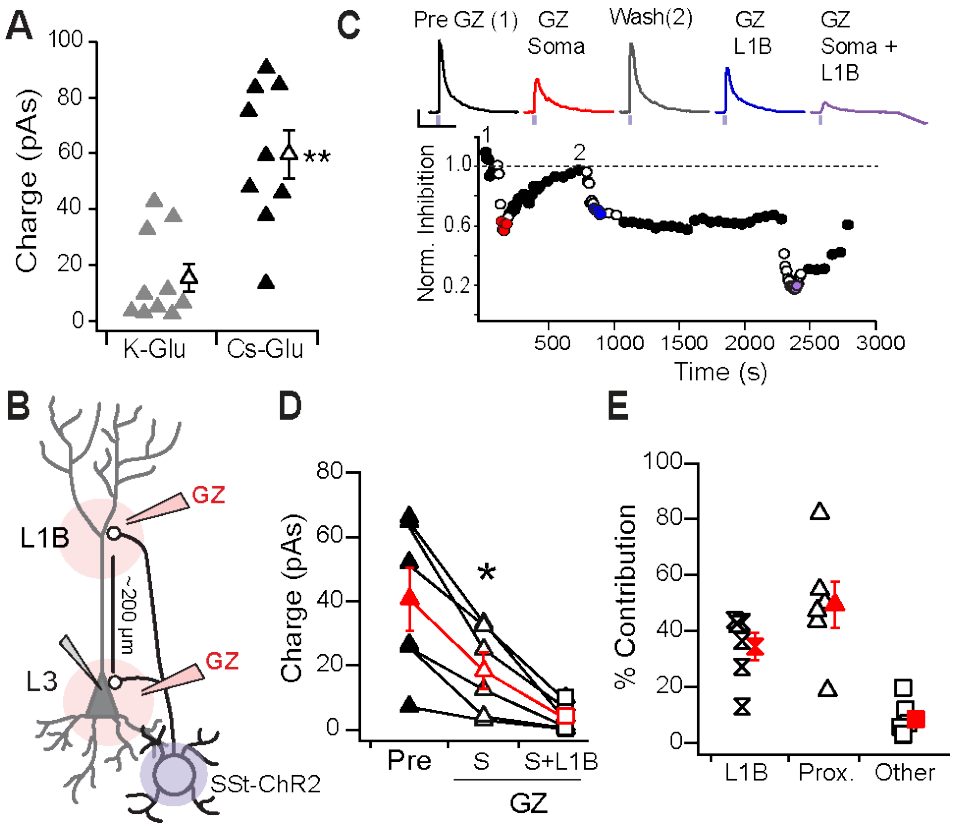

Figure 14. SST mediated inhibition of L3 pyramidal cells.

(A) Mean IPSC strength significantly differed recorded in pyramidal cells with K-Gluconate (gray) versus Cs-Gluconate (black) internal solutions (**p<0.01, unpaired t-test). (B) Schematic of locations for distal (L1B) versus proximal (L3, soma) gabazine (GZ) application. (C) Time course of IPSCs recorded in response to somatic and distal application of GZ in an example cell. IPSC strength was normalized to the average pre-GZ strength (black circles, 1). Open circles indicate GZ applications. IPSC responses to GZ application (top) correspond to average of colored circles (Red: GZ soma; Blue: GZ L1B; Purple: GZ L1B+Soma). IPSC amplitudes recovered between somatic and L1B applications (Wash, 2) but not following L1B. (D) IPSC strength in response to somatic GZ application (open triangles) significantly differs from pre-GZ baseline (filled triangles) and somatic+L1B application (squares) (p<0.05, WSR test). (D) The percent contribution of distal (L1B) and proximal (somatic) inhibition to the total inhibition recorded at baseline. 'Other' corresponds to the percent of inhibition that remained during GZ application at both the soma and L1B.

In a subset of L3 pyramidal cells (n=6), we investigated SST-mediated inhibition of perisomatic regions versus dendrites in L1B. Both regions have highly fluorescent neuropil in SST-tdTom mice indicative of projections from SST-cells (Figure 7). We locally applied the GABAA receptor antagonist, Gabazine (GZ, 40 μM, see Methods) to the soma, to L1B, then to both sites simultaneously while recording light-evoked IPSCs in L3 PCs (schematic, Figure 14B). We chose L3 PCs because the somas and L1B were 221 ± 23.9 μm apart and offered better isolation of proximal versus distal inhibition. Proximal inhibition was blocked by GZ application at the soma, while distal inhibition was blocked by GZ in L1B. Typically 10 min recovery time was allotted between applications at somatic and L1B sites. However, only two cells demonstrated sufficient recovery from GZ application at the soma to separately assess the contribution proximal inhibition by blockade of L1B (Figure 14C). None of the cells recorded showed sufficient recovery from L1B application in the time allotted (as seen in Figure 14C). Finally, GZ was simultaneously applied at both the soma and L1B. This blocked greater than 90% of the total inhibition in all cells.

Somatic GZ application significantly reduced inhibition from 40.6 ± 9.82 pA·s to 18.4 ± 5.59 pA·s (p: 0.025 WSR test, Figure 14D) suggesting that the remaining inhibition (~45%) is attributed to dendritic synapses. Simultaneous somatic and L1B GZ application further reduced IPSC strength (4.07 ± 1.64 pA·s, p: 0.025, WSR test). Since approximately 8 ± 3% of inhibition remained following simultaneous GZ application at both sites, we subtracted this value in our estimates of the percent contributions of somatic and dendritic inhibition. Overall, we find that distal L1B inhibitory synapses account for at least 39 ± 7% of the inhibition received by PCs while proximal somatic synapses provide 43 ± 7% (Figure 14E). These values did not

significantly differ ($p>0.05$, WRS test). Thus, in addition to dendritic inhibition, our findings suggest that SST-cells also contribute to perisomatic inhibition of PCs. However, given that some PV-cells express ChR2 in SST-cre animals, further experiments are required to fully isolate the role of SST-cells in somatic inhibition. It is highly unlikely that off-target recombination in PV-cells contributes significantly to dendritic inhibition in L1B of PCs because PV-cells minimally project to this layer (Figure 7D, 2). Thus, these findings do confirm that SST-mediated inhibition regulates distal dendritic processing of afferent (L1A) and recurrent inputs (L1B) as predicted by anatomical projections.

3.4 DISCUSSION

The development of transgenic lines that selectively target SST-cells (SST-cre, GIN) or PV-cells (PV-cre and G42) has been highly beneficial with respect to understanding the roles of these interneurons classes in cortical processing. The target neurons in these lines have been described with respect to anatomical distribution, SST or PV expression, and intrinsic neuronal properties in a number of neocortical sensory areas including visual, somatosensory and auditory cortex (Chattopadhyaya et al. 2004; Y. Ma et al. 2006; Kuhlman and Huang 2008; Oswald and Reyes 2011; Hang Hu, Cavendish, and Agmon 2013). However, despite their utility, few studies have characterized these transgenic lines outside of neocortex (Oliva et al. 2000; Cabezas et al. 2013; Nassar et al. 2015). In this study, we describe several important and novel findings with respect to the distributions, physiology and connectivity of SST cells in piriform cortex.

3.4.1 Distributions and electrophysiological properties of SST interneurons

We started with the simple assumption that the distributions and properties of interneurons selectively labeled in SST-cre, PV-cre, GIN and G42 mice are comparable across sensory cortical areas regardless of paleocortical or neocortical location. The anatomical distributions of SST-cre and PV-cre cell somas and neuropil are consistent with immunohistochemical studies in olfactory cortex (Gavrilovici, D'Alfonso, and Poulter 2010; Suzuki and Bekkers 2010a; Kay and Brunjes 2014). Specifically, the density of SST-cre cells is greater than PV-cre cells and the somas of both classes are predominantly located in deep layers of the APC. Further, SST-cre cells project to L1B and L2/3 while PV-cre cells project mainly to L2/3. However, SST and PV cells in the GIN and G42 lines respectively, are sparse in piriform cortex. Although GIN and SST-cre cell populations overlap in APC, GIN cells account for only 2-6% of all SST-cells. G42 cells are located in deep L3 of APC and endopiriform cortex and have the strikingly different electrophysiological properties compared to PV-cre cells. Thus, while cre-lines encompass of the majority of SST and PV cells in piriform cortex, GIN and G42 lines only represent small subsets of SST or PV cell types. Thus, we caution against using GIN and G42 lines as the sole markers of SST or PV cells in piriform cortex.

In the absence of fluorescent markers, neocortical SST cells have been distinguished by broad spike widths and regular (RS) or low threshold (LTS) spiking patterns while PV cells are fast spiking (FS) and have narrow spike widths (Kawaguchi and Kubota 1996, 1997; Yoshiyuki Kubota and Kawaguchi 2000; Nowak et al. 2003; Casale et al. 2015). These distinctions have been the basis for both in vitro and in vivo characterization of these classes. However, we find that approximately 70% of SST-cre cells in piriform cortex have FS responses and narrow spike widths that are superficially indistinguishable from PV-cre cells. Nonetheless, we show that SST

and PV cells with FS properties can be differentiated with relatively low error using clustering algorithms and a number of suprathreshold (i.e. CV_{ISI}) and/or subthreshold (i.e. Sag) properties.

At least three classes of SST-cells have been described based on selective GFP labeling in GIN, X98 and X94 transgenic lines (Y. Ma et al. 2006; Nassar et al. 2015). Interneurons in the X94 line have FS and/or stuttering properties similar to PV cells (Y. Ma et al. 2006; Xu et al. 2013). Neocortical X94 cells do not project to L1 but provide substantial inhibition to PV cells as well as excitatory cells located in the same or nearby layers (Y. Ma et al. 2006; Xu et al. 2013). Our findings suggest that FS SST-cells in piriform cortex are similar to X94 cells and could locally inhibit PV and pyramidal cells in L2/3. Conversely, interneurons in the GIN and X98 lines exhibit RS responses and project axons to L1 (Y. Ma et al. 2006). While the properties of RS cells in piriform cortex were more consistent with neocortical GIN cells than X98 cells, RS neurons were sampled more often (30%) than predicted by the sparseness of GIN cells (<5% of SST cells) suggesting they may be akin to X98 cells. Nonetheless, the RS SST-cre cells we recorded are likely the same class of interneurons as SST(+), regular-spiking multipolar (rMP) cells that project to L1 of piriform cortex (Suzuki and Bekkers 2010b). Taken together, our findings suggest at least two classes of SST cells exist in APC that are consistent with X94 and GIN/X98 classifications.

3.4.2 SST-interneuron mediated inhibition

SST-cells are a major source of inhibition to pyramidal cells and a wide variety of interneurons in neocortex (Fino and Yuste 2011; Pfeffer et al. 2013; Xu et al. 2013; Jiang et al. 2015). We find that SST-cells inhibited nearly all recorded neurons in APC, including PCs, SST cells, pPV cells and 4 other unidentified types of inhibitory interneuron found in L2/3. With respect to PCs,

we find that SST-cells strongly inhibit distal dendritic regions in L1B and likely, perisomatic regions. However, the latter could be contaminated in this study by off-target recombination in PV-cells. Nonetheless, our findings confirm a role for SST-cells in mediating dendritic inhibition in L1 and thus, regulating the flow of information from afferent (L1A) and recurrent (L1B) networks. An interesting possibility is that distal versus proximal inhibition is mediated by RS (GIN/X98) versus FS (X94-like) SST cells.

In contrast to previous findings that SST cells do not inhibit each other in neocortex (Pfeffer et al. 2013), we find that SST cells inhibit other SST cells in piriform cortex. Further, postsynaptic SST cells had subthreshold properties consistent with FS rather than RS SST-cells. This finding further supports the notion that different SST classes may play different functional roles in piriform cortex. We were unable to fully investigate the diversity or proportion of SST-interneurons inhibited because of ChR2 contamination. However, it is unlikely these findings are due to off-target expression in PV-cells. The rate of finding these cells was too high (6/6) given the low percentage (14%) of PV SST-tdTom cells that are PV(+). Moreover, PV cells rarely and only weakly inhibit SST-cells (Pfeffer et al. 2013).

Finally, SST cells inhibited the majority of interneurons recorded in L2/3 of piriform cortex as previously shown in neocortex (Pfeffer et al. 2013; Jiang et al. 2015). Although electrophysiological traits are not entirely indicative of neural class, we were able to cluster YFP(-) interneurons into 5 groups using the three subthreshold parameters (Rin, τm, and Sag). In particular, putative PV (pPV) interneurons clustered with identified PV-cre cells recorded under the same conditions. Interestingly, the distributions IPSC strengths co-varied with these interneuron groups. The strongest and most variable IPSC strengths were recorded pPV, Group 2 (G2), and SST interneurons. These groups were most similar with respect to Rn, τm, and Sag.

Group 3 and 5 interneurons, tended toward higher Rn, τm and Sag values, and received weaker, less variable inhibition. Group 3 interneurons in particular routinely received weaker inhibition when compared with other interneuron types in the same slice or animal.

Since we did not know the interneuron groups in advance, multiple comparisons between groups were required, which greatly reduced overall statistical power. However, our findings suggest refined hypotheses are possible provided interneuron classes are identified. For example, when we used vasoactive intestinal peptide expressing interneurons (VIP-cre) as benchmark neurons (data not shown), these clustered with G3 interneurons. In other cortical areas, VIP interneurons preferentially target SST and PV cells over PCs (S. Lee et al. 2013; Pfeffer et al. 2013; Pi et al. 2013; Y. Fu et al. 2014). Conversely, calbindin (CB) expressing interneurons have the highest density in APC and CB is frequently co-expressed in PV cells (Suzuki and Bekkers 2010a). We speculate that G2 interneurons are CB-interneurons. A potential hypothesis is that SST cells provide stronger inhibition to PC-targeting interneurons (i.e. PV, CB, SST) versus interneuron targeting interneurons (i.e. VIP cells). It is clear that additional and very different experiments are required to investigate these possibilities.

3.4.3 Potential caveats

Expression patterns can differ between techniques that involve crossbreeding cre-mice with reporter or optogenetic lines like Ai14 or Ai32 versus viral expression techniques. Using crossbreeding, we find consistent expression of tdTom as well as ChR2 evoked IPSC amplitudes across animals and litters. Further, there is more uniform spatial expression within animals. This is advantageous with respect to capturing weak or spatially dependent responses that would be susceptible to variable expression using viral techniques. However, a potential drawback of

crossbreeding is off-target recombination in neurons that transiently express SST during development (Hang Hu, Cavendish, and Agmon 2013). We find that ~75-85% of SST-tdTom cells in APC express somatostatin (SST(+)) but this may be an underestimate given the variability of SST immunolabeling across cells. We also found that 6-15% of SST-tdTom cells express parvalbumin (PV(+)). It is unlikely that PV(+) labeling in SST-tdTom tissue is due to non-specific staining given the ~95% overlap of PV(+) and tdTom(+) cells in PV-tdTom animals. Finally, although interneurons that co-express PV and SST have been reported in L3 of rats (Cummings and Neuropeptide 1997), we find that only 6% of PV-tdTom cells are SST(+). Thus, we cannot rule out off-target recombination as a factor in our experiments. Nonetheless, we expect that our main findings are not qualitatively affected by off-target recombination since most SST-cre cells are indeed SST(+) and only a small number are PV(+). However, we have highlighted results throughout that may be quantitatively susceptible. Going forward, it would be useful to verify the findings of this study using viral transfections in older animals that minimize the potential for developmentally regulated off-target recombination.

3.4.4 Conclusions

In summary, we report several findings with respect to SST and PV interneurons in piriform cortex. First, GIN and G42 transgenic lines only represent a small subset of the SST and PV cell populations in piriform cortex. Second, only one-third of SST cells are classically RS and the remaining SST cells exhibit FS properties similar to PV cells suggesting at least two classes of SST-cells in piriform cortex. Third, SST cells inhibit distal dendritic and likely perisomatic regions of PCs. Fourth, SST cells provide broad inhibition to nearly all interneuron classes

recorded, including SST and pPV cells. And fifth, SST cells may differentially inhibit interneuron classes such as PV cells. Our findings suggest that SST cells are poised to function in a number of different inhibitory circuits including dendritic regulation of afferent and recurrent excitation in PCs, inhibition of interneurons, and potentially disinhibition of PCs through SST-Interneuron-PC circuits. Overall, these findings suggest that SST-cells play a prominent role in regulating network excitation and inhibition during olfactory processing.

4.0 SOMATOSTATIN-MEDIATED INHIBITION MEDIATE ACTIVITY GRADIENTS IN PIRIFORM CORTEX

4.1 INTRODUCTION

It is well established that the spatial organization of sensory information plays an important role in neocortical sensory processing. The retinotopic, tonotopic and somatotopic maps established at the periphery form the basis of stimulus representation in primary visual, auditory and somatosensory cortices (Merzenich, Kaas, and Roth 1976; Tootell et al. 1982; York and Steinberg 2011). This spatial organization is perhaps the oldest and best understood feature of sensory codes.

In the olfactory system, odor components are encoded by individual olfactory receptor neurons (ORNs) that express a single receptor gene. All ORNs expressing the same receptor project axons to one of two target glomeruli in the olfactory bulb (OB) (Ressler, Sullivan, and Buck 1994; Vassar et al. 1994; Mombaerts et al. 1996). Within the OB, mitral/tufted (M/T) cells extend apical dendrites to a single glomerulus and M/T cells receiving different glomerular inputs interact solely through connections with inhibitory interneurons. This extreme connection specificity produces a discrete spatial organization of odor component information within the OB (Soucy et al. 2009; L. Ma et al. 2012). However, just one synapse away in the anterior piriform cortex (APC), any semblance of spatial representation for odors is lost.

The piriform cortex is a trilaminar cortex that extends along the rostral-caudal (RC) axis of the ventral rodent brain. The two main subdivisions, anterior (APC) and posterior (PPC) piriform cortex, differ with respect to afferent and efferent projections (Lewis B. Haberly and Price 1977; Luskin and Price 1982; Scott 1981; Ekstrand et al. 2001) as well as functional roles in olfactory processing (Neville and Haberly 2004; Gottfried, Winston, and Dolan 2006). However, even though each region comprises ~2 mm of the RC axis, odor processing within APC or PPC has been considered spatially homogenous. The APC is delineated by the presence of the lateral olfactory tract (LOT) that delivers odor information directly from the OB. Single M/T cell axons branch extensively along the LOT (Sosulski et al. 2011; Rennaker et al. 2007; Stettler and Axel 2009; Lewis B. Haberly and Price 1977; Price 1973; Luskin and Price 1982) resulting in diffuse pattern of afferent excitation. Likewise, recurrent connections between principal neurons within APC extend over millimeter distances (Franks). Consistent with this distributed excitatory architecture, there is no apparent topography of odor identity in APC. Neurons responsive to a single odor are sparsely distributed along the RC-axis of the APC (Rennaker et al. 2007; Stettler and Axel 2009) and nearby neurons respond to different odors (Stettler and Axel 2009; Bekkers and Suzuki 2013). The absence of an "odortopic" map, suggests that, unlike sensory neocortex, space is not a dimension for odor coding in APC.

Nonetheless, there is evidence that odor evoked responses in APC can vary along the rostral-caudal axis. For example, odor evoked activity at rostral sites is denser (ref), has lower concentration thresholds (Sugai et al. 2005), and has earlier response times (Igarashi et al. 2012) versus caudal sites. Further, in contrast to excitation, intracortical inhibition of pyramidal cells shows RC asymmetry (Luna and Pettit 2010). Finally, rostral APC projects more strongly to the OB and orbitofrontal cortex (OFC) while caudal APC and PPC project to agranular insula (AI)

(Ekstrand et al. 2001; C.-F. F. Chen et al. 2014). These findings suggest that, contrary to preconceived notions, space may be relevant dimension for olfactory processing in APC. However, a central challenge is elucidating the circuit mechanisms and functional roles of rostral-caudal spatial patterning in APC.

Here we provide evidence that rostral-caudal asymmetry in inhibition matches the spatial scale of neural activity in APC, particularly when the mouse explores a novel odor context. More specifically, we find that inhibition increases along the rostral-caudal axis commensurate with a decrease activated neurons. We further show that a disinhibitory circuit, mediated by Somatostatin (SST) interneurons supports RC patterning of inhibition and modulating SST-cell activity neutralizes the RC spatial profile of inhibition. Altogether, our findings suggest a model in which rostral-caudal patterning of inhibition can be gated through SST-interneuron activity to influence the spatial patterns of neural activity, and subsequently cortical output in different odor contexts.

4.2 MATERIALS AND METHODS

4.2.1 Animals

Several transgenic mouse lines and crosses were used in this study. The VGAT-ChR2 mice (VGAT-Chr2: B6.Cg-Tg(Slc32a1-COP4*H134R/EYFP)8Gfng/J) express channelrhodopsin in all interneurons (ref). The SOM-Cre (B6:Sst<tm2.1(cre)Zjh>/J) mice were crossed with Ai32 mice (B6:129S-Gt(ROSA)26Sortm32(CAG-COP4*H134R/EYFP)Hze/J) or DREADDi mice (B6N.129-Gt(ROSA)26Sortm1(CAG-CHRM4*,-mCitrine)Ute/J) to express channelrhodopsin

(Madisen et al. 2012) or the inhibitory DREADD, hM4Di (Zhu et al. 2016). Finally, TRAP mice (TRAP-fos: (B6.129(Cg)-Fos(tm1.1(cre/ERT2)Luo/J) were crossed with Ai14 (B6.Cg-Gt(ROSA)26Sortm14 (CAG-tdTomato)Hze/J) to conditionally express tdtomato (Guenthner et al. 2013). All mice are Jax mice from Jackson Laboratories. Mice were housed in groups of 2-5 animals on a 10:14 light/dark cycle unless otherwise stated. All experiments involved mice of both sexes and age ranges from P20-P300 as indicated.

4.2.2 Slice preparation

Brain slices of anterior piriform cortex (APC) were prepared from mice aged P19-35. The mice were anesthetized with isoflurane and decapitated. The brain was removed from the skull and immersed in ice cold oxygenated (95% O2-5% CO2) ACSF (in mM: 125 NaCl, 2.5 KCl, 25 NaHCO3, 1.25 NaH2PO4, 1.0 MgCl2, 25 Dextrose, 2.5 CaCl2) (all chemicals from Sigma, USA unless otherwise stated). Parasagittal slices (300 μm) were made using a vibratome (Leica Biosystems) in ice cold ACSF. The slices were transferred to warm ACSF (37°C) for 30 min and then rested at 20-22°C for 1 hour prior to recording (31-35°C). All surgical procedures were approved by the University of Pittsburgh IACUC.

4.2.3 Electrophysiology

Whole cell, voltage and current clamp recordings were performed using a MultiClamp 700B amplifier (Molecular Devices, Union City, CA). Data were low pass filtered (4 kHz) and digitized at 10 kHz using an ITC-18 (Instrutech) controlled by custom software (Recording Artist, https://bitbucket.org/rgerkin/recording-artist) written in IgorPro (Wavemetrics).

Recording pipettes (4-10 MΩ) were pulled from borosilicate glass (1.5 mm, outer diameter) on a Flaming/Brown micropipette puller (Sutter Instruments). The series resistance (<20 MΩ) was not corrected. The intracellular solution consisted of (in mM) 130 K-gluconate, 5 KCl, 2 MgCl2, 4 ATP-Mg, 0.3 GTP, 10 HEPES, and 10 phosphocreatine, 0.05% biocytin, 4.5 µM QX-314. Recordings were obtained from L2/3 pyramidal cells (PCs) as well as interneurons in L3. Neurons were visualized using infrared-differential interference contrast microscopy (IR-DIC, Olympus). When possible, interneurons were targeted using yellow (YFP) fluorescence and PCs as the absence of fluorescence in transgenic mice. For all neurons, intrinsic subthreshold properties such as input resistance, and time constant were assessed using a series of hyperpolarizing and depolarizing current steps (-50 pA to 50 pA, 1 s duration). Neural identity was confirmed post hoc using intrinsic properties and anatomical analysis of biocytin fills.

4.2.4 Light stimulation

Blue light (λ=460-488 nm, GFP block, Olympus) for full-field optical stimulation was provided by metal halide lamp (200W, Prior Scientific) passed through the microscope objective (60x, immersion, Olympus). Light pulses were controlled using a mechanical shutter (Sutter Instruments). The light spot was restricted to a ~70 µm diameter (0.5 mW) using the minimum aperture. To obtain the spatial profile of inhibition, interneurons were focally activated in a 5x4 grid pattern while IPSCs were recorded in interneurons or PCs. The horizontal axis of the grid was centered on the recorded neuron with stimulation sites ranging from -300 µm (rostral) to +300 µm (caudal) at 150 µm increments. The vertical axis ranged L1 to L3 in 125 µm increments corresponding to different lamina. Each grid site was stimulated with 2 light pulses (20 ms duration, 100 ms interpulse interval, 15 s between trials). The 20 ms duration was chosen

to reliably evoke least one spike and rarely 2 spikes in response to a single pulse of direct somatic stimulation using the 70 µ spot at 0.5 mW (Large et. al 2016). Grids were repeated 3-5 times per neuron and each grid site was stimulated once every 6 min. Since inhibitory neurons are activated and there is little evidence of depolarizing inhibition, polysynaptic responses are unlikely under these recording conditions.

4.2.5 Drug Application

Stock solutions of the DREADD agonist, Clozapine-N-oxide (CNO, 10 mM, 13.8% DMSO in 0.9% Saline) were freshly made for each cohort of animals, aliquoted and stored at -20°C for up to 2 weeks. On the day of experiment, CNO stock was diluted (20 µM in ACSF) and bath applied.

4.2.6 Analysis of inhibition

Electrophysiology traces of IPSCs are presented as the average across trials for individual neurons. IPSC strength was taken as the area (pA·s) under the IPSC. Average PSCs with minimum amplitude of 10 pA were included for analyses; smaller PSCs were not distinguishable from noise. Unless otherwise stated, all results are presented as the mean ± standard error (SE). To compare the spatial profiles of inhibition across animals IPSC amplitudes were normalized to the strength of the maximum IPSC regardless of location in the grid. The rostral-caudal bias was taken as the average normalized inhibition from the caudal sites minus the average inhibition of the rostral sites, divided by the summed inhibition from both sides. The bias metric ranges from -

1 (rostral bias) to +1 (caudal bias). Since L1 inhibition was typically weak (Large et al., 2016) these sites were excluded from the bias metric.

4.2.7 Tamoxifen Injection and Odor Exposure

We chose the breakdown product of tamoxifen, 4-hydroxytamoxifen (4-OHT) (Sigma) because the time window for activation was faster and narrower than tamoxifen (Guenthner et al. 2013). Doses of 4-OHT were freshly made on the day of injection. Briefly, 15 mg was dissolved in in 200µl of 100% ethanol by sonication at 37°C (~1 hr). Then 1.5 ml of peanut oil (Sigma) was added. The solution was then vortexed 10 s, and ethanol was then removed via centrifugation (15 min) and vacuum evaporation (1-2 hrs). The final solution was filtered (0.2 µm). The 4-OHT was administered by intraperitoneal injection at 50mg/kg (~150-200 µl per animal) 30 min before odor exposure.

There were three groups of mice (P90-300): home cage animals (HC), home cage plus odor (HCO) and novel environment plus odor (NEO). Experiments were done serially, with 4 mice per cohort. In each cohort, there was at least one mouse per condition. However, there were losses due to death (n=2), poor perfusion (n=2) and insufficient tamoxifen dosage (n=3). Whenever possible, mice from the same litter were used for each cohort or nearly age-matched litters (± 1 week) were used. Mice were housed 12:12 light/dark cycle and all testing was done ±1 hr from the onset of the dark cycle. Mice were singly housed and food restricted (90% body weight) as well as handled and weighed daily for 4 days prior to 4-OHT injection and odor (HCO, NEO) exposure. Odor stimuli were a 1:100 dilution of isoamyl acetate or ethyl butyrate in mineral oil. For HCO animals, 100µl odor was applied to a cotton ball in an open tube that was placed in the cage for 30 min. For NEO mice, 1x0.5 mm filter paper was saturated with odor and

then buried in a paper cup filled with clean bedding. To encourage exploration, the cup of odorized bedding was placed at the end of one arm of a divided arena (20x10 inches) and a blank cup of bedding in the other arm (, Figure 5A2). The NEO animals explored both the odorized and non-odorized arms as well as the center (C) of the arena (Figure 19A3). The mice spent nearly equivalent time per visit in the odorized (8.1 ± 3.5 s) and non-odorized (9.8 ± 3.5 s) arms, but tended to make more visits to the non-odorized arm (49 ± 33) versus the odorized arm (25 ± 14, n=4). Since animals were not pre-adapted to the arena, neural activity in NEO animals likely reflects the composite response to novel odors and context, rather than solely a response to the odorized cup. Following tamoxifen injection and testing, animals were undisturbed in their home cages in the dark for 10-12 hours. Mice were sacrificed 5 days post tamoxifen and neural activity in each context was quantified as the density of tagged, tdTom(+) neurons in L2 and L3 of APC.

4.2.8 Anatomy

Mice were given an overdose of ketamine-xylazine. Mice were then perfused transcardially (20 ml/min) with 0.1 M sodium phosphate buffer (PB), followed by 200 ml of 4% paraformaldehyde (PFA) in 0.2M PB. Brains were removed and fixed in 4% PFA overnight at 4°C, then transferred to a sucrose solution. Coronal slices (50 µm) were cut using a freezing microtome maintained in phosphate buffer prior to immunochemistry (anti-PV or anti-CB staining) and/or mounting. Parvalbumin (PV) cells were immunostained using rabbit anti-parvalbumin (PV27, Swant, 1:1000). Calbindin cells were immunostained using rabbit anti-calbindin D-28K (CB38, Swant, 1:1000). In both cases, the secondary was donkey anti-rabbit Alexa-fluor-488 (#A21206 Life Technologies, 1:500). Every other section was mounted using fluoromount to protect fluorescence and minimize background. Sections were imaged on a Nikon Eclipse-Ci

microscope at 4x-20x magnifications. Illumination was provided by a mercury lamp (Nikon Intensilight) and delivered through appropriate filter blocks for GFP (495 nm) and tdTomato (585 nm). Light intensity and exposure duration (100-400 ms) were optimized for the first section in a series using automated software (Nikon Elements), then maintained for ensuing sections. Sections were photographed using a CCD HD color camera (Nikon DsFi2).

4.2.9 Cell counts

Neural densities were quantified as number of cells per mm2 in laminar regions of interest (ROI) within the ventral anterior piriform cortex (APC). Counts were made in a single focus plane (4x magnification) for each section chosen to maximize the number of cells in focus. Automated counts of somas were obtained based on fluorescence intensity and circularity using Elements Software (Nikon). Two researchers independently verified all counts with at least one blind to condition. In the event of discrepancy, a third individual, blind to condition, counted the sections. Every other coronal section (8-15 sections per animal) was analyzed spanning 1-1.5 mm along the rostral-caudal extent of the APC. The average density was taken across all sections in each animal. The assess rostral-caudal spatial patterning, densities in each section were normalized to the most rostral section taken at ~2.46 mm from Bregma (Paxinos). For each animal, a least-squares fit to a linear regression was used to determine the slope of the relationship between normalized density and distance along the rostral caudal axis.

4.2.10 Statistics

Statistical tests were performed using one and two sample, paired and unpaired Student's t-test as appropriate. In cased of small sample sizes (<10) non-parametric Mann-Whitney U-tests (MWU) were used for unpaired data while Wilcoxon Signed Ranks tests (WSR) for paired data. For equal variances and multiple comparisons, we used ANOVA with post hoc Tukey Test (ANOVA-Tukey). For groups with small sample sizes multiple comparisons of the distributions were made using non-parametric, Kruskal-Wallis tests (KW-test). All statistical tests are indicated in the main text.

4.3 RESULTS

4.3.1 Asymmetric inhibitory circuitry in APC

Spatially asymmetric inhibition of pyramidal cells in APC (Luna and Pettit 2010) has been previously demonstrated using glutamate uncaging. Specifically, light evoked uncaging at caudal stimulation sites yielded stronger inhibition of PCs compared to rostral sites. These findings are seemingly at odds with the spatial profiles of afferent and recurrent excitation (Sosulski et al. 2011; Igarashi et al. 2012; Franks et al. 2011; Yang et al. 2013) and odor-evoked responses (Stettler and Axel 2009; Bekkers and Suzuki 2013)) that do appear to vary with space. This led us to question, "How and why do inhibitory spatial asymmetries exist in APC?"

Since previous un-caging methods could activate both excitatory and inhibitory neurons, we first investigated whether inhibitory circuits alone are sufficient to reproduce inhibitory

asymmetries. We selectively activated interneurons using Channelrhodopsin (ChR2-YFP) under the vesicular GABA transporter (vGAT) promoter (VGAT-ChR2) (S. Zhao et al. 2011). Briefly, whole cell recordings were made from L2 principal excitatory neurons, namely semilunar cells (SL) and superficial pyramidal cells (sPC) as well as deep pyramidal cells (dPC) in L3. Recorded neurons were centrally located along the RC axis in sagittal slices of APC. VGAT-ChR2 interneurons were stimulated using restricted spots (~70 μm diameter) of blue light in 4x5 grid surrounding the recorded cell (schematic, Figure 15A, D1) (Large, Vogler, et al. 2016). The strength of inhibition was quantified as the area (pA·s) under the first peak of the trial-averaged population IPSCs evoked at each stimulation site (Figure 15B1,C1,D2). To quantify inhibitory asymmetry, a bias index was calculated as the difference in average inhibition across caudal versus rostral stimulation sites, divided by the sum of the average inhibition from both sides (Figure 15B2, C2, D3). Thus, inhibition from solely caudal locations produces a bias value of +1 while a value of -1 corresponds to solely rostral inhibition. We found sPCs (L2) and dPCs (L3) received significant, caudally biased inhibition (sPC bias: 0.22 ± 0.08, p: 0.016, n=14, Figure 15C2; dPC bias: 0.19 ± 0.05; p: 0.0012, n=16, one sample t-test, Figure 15D3). However, inhibition was not significantly asymmetric in SL cells (bias: 0.08 ± 0.11, p: 0.49, n=13, Figure 15B2). Thus, inhibitory circuitry alone is sufficient to reproduce asymmetric inhibition of PCs along the RC-axis. Notably, inhibition of sPCs was significantly weaker than dPCs (Large, Vogler, et al. 2016). For this reason, we focused the remainder of our experiments on dPCs.

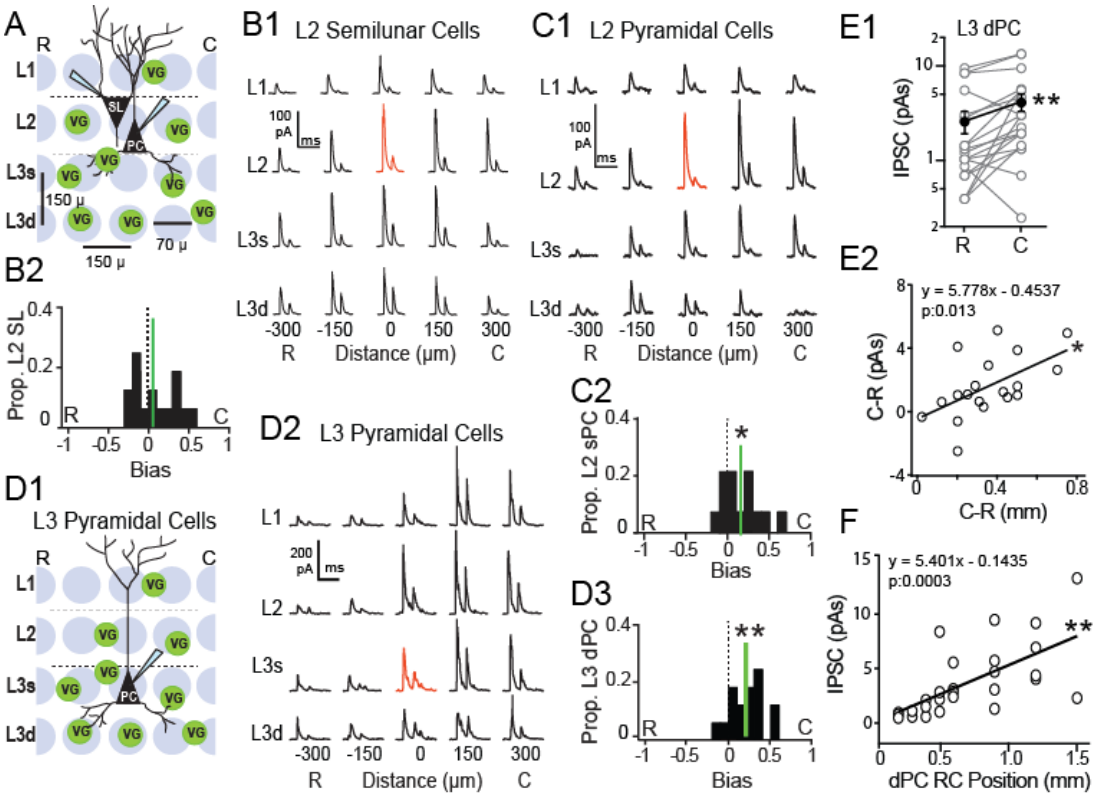

Figure 15. Asymmetric Inhibition onto Principal Cells

(A) Schematic of optogenetic experiments in layer 2. Grey circles: location and size of light stimulus. SL: semilunar cell. PC: Pyramidal Cell. VG: VGAT-ChR2 cell. (B) Analysis of Layer 2 semilunar cells. (B1) example IPSC traces onto semilunar cells across layers at each rostrocaudal position. Red trace when light is presented at the soma (B2) Distribution of bias metrics across layer 2 semilunar cells. Dashed line at zero. Green line at mean. (C) Analysis of Layer 2 pyramidal cells. (C1, C2) As in B1 and B2, for layer 2 pyramidal cells. (D1) schematic of optogenetic experiments for layer 3. Notation same as A. (D2, D3) as in B1 and B2, for layer 3 pyramidal cells. (E) Analysis of inhibitory strength between pairs of layer 3 pyramidal cells. (E1) Comparison of inhibition a pair of layer 3 pyramidal cells – one caudal and one rostral. Error bars: S.E.M. (E2) Scatter plot of difference in rostrocaudal position between two pyramidal cells and the difference in inhibitory strength between the same pyramidal cells. (F) Scatterplot of inhibitory strength onto layer 3 pyramidal cells against the rostrocaudal position of each pyramidal cell. *: $p<0.05$, **: $p<0.01$

One interpretation of these findings is that caudally located PCs receive stronger inhibition than rostral PCs. To investigate this possibility, we compared local inhibitory strength in dPC pairs (n=19) separated by (100-1000 μm) distances along the ~1.5 mm RC-axis. On average, the caudal neuron of the pair received significantly more inhibition (4.18 ± 0.90 pA·s) than the rostral neuron (2.60 ± 0.68 pA·s, p: 0.002, paired t-test, Figure 15E1). Moreover, as the distance between the rostral and caudal neuron increases, the difference in inhibitory strength increases (slope: 5.8 ± 2.1 pA·s/mm, p: 0.013, Figure 15E2). Finally, across a population of dPCs, inhibitory strength increased with soma location relative to the rostral start of the LOT (slope: 5.6 ± 1.6 pA·s/mm, p: 0.0017, n=23, Figure 15F). Thus, there is a gradient of increasing inhibition onto dPCs with a spatial scale that extends >1.0 mm of the RC axis of APC.

What circuit mechanisms might underlie this increasing RC gradient of inhibition? To test if stronger caudal inhibition is general feature of APC we investigated inhibition of L2 and L3 YFP(+) interneurons using grid stimulation of vGAT-ChR2 interneurons (Figure 16A). L2 interneurons did not receive significantly asymmetric inhibition (bias: 0.04 ± 0.07, p: 0.11, n=18, Figure 16B1,2). However, surprisingly, L3 interneurons received stronger inhibition from rostral sites rather than caudal locations (bias: -0.13 ± 0.05, p: 0.013, Figure 16C1,2). Overall, L3 interneurons received much stronger inhibition (7.02 ± 0.92 pA·s) than L2 interneurons (3.42 ± 0.5 pA, p: 0.0043) but comparable inhibition to L3 dPCs (8.63 ± 0.84, p: 0.239) (Figure 16D). The bias indices of L3 interneurons significantly differed from dPCs (p: 0.0001, t-test, Figure 16E). Thus, dPCs and L3 interneurons have opposing spatial profiles of inhibition- dPCs receive stronger inhibition from caudal sites versus rostral sites (0.63 ± 0.034, p: 0.003, paired t-test) and L3 interneurons receive significantly more inhibition from rostral sites versus caudal (0.54 ± 0.033, p: 0.008, paired t-test Figure 16F).

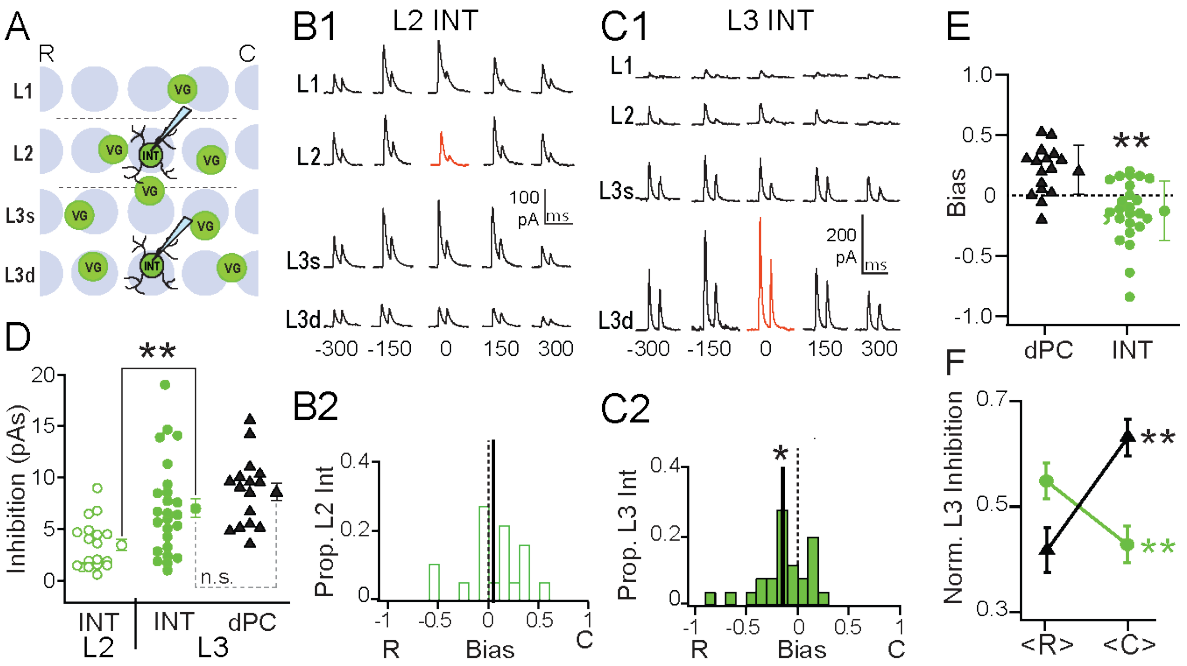

Figure 16. Asymmetric Inhibition onto Interneurons.

(A) Schematic of optogenetic experiments. INT: interneuron VG: VGAT-ChR2 neuron. (B) Analysis of inhibition onto layer 2 interneurons. (B1) example IPSC traces across layers at each rostrocaudal position. Red trace indicated light presented at soma (B2) distribution of spatial bias in layer 2 interneurons. Dashed line at zero. Black line at sample mean. (C) Analysis of inhibition onto layer 3 interneurons. (C1, C2) as in B1, B2 for layer 3 interneurons. (D) comparison of inhibitory strength between layer 2 interneurons, layer 3 interneurons, and layer 3 pyramidal cells. (E) comparison of inhibitory bias between layer 3 pyramidal cells and interneurons. (F) Normalized inhibition in layer 3 between rostral and caudal sites for layer 3 pyramidal cells (black) and layer 3 interneurons (green). Error bars: S.E.M. *: $p<0.05$, **: $p<0.01$

How do inhibitory circuits implement opposing RC inhibitory asymmetries and what is the functional role of this opposition? The simplest mechanism for an increasing gradient of inhibition is to increase the number of interneurons along the RC axis. In vGAT-ChR2 mice all interneurons express YFP, but interneurons can show great specificity with respect postsynaptic targets. The majority (~85%) of PC-targeting interneurons in L3 express parvalbumin (PV),

somatostatin (SOM) and/or calbindin (CB) (Suzuki and Bekkers 2010a). To quantify the densities of the different interneuron classes along the RC axis, identified interneurons were counted in L3 of alternate sections (100 µm increments) along 1 mm of the RC axis. All densities were normalized to the most rostral section (~2.46 mm from Bregma, Paxinos). For each animal, normalized density versus RC distance was linearly fit to obtain the slope corresponding to the proportional change in density per mm^{-1}. SOM cells were identified as tdTom(+) cells in SOM-Ai14 mice (n=7 mice) while PV and CB cells were identified using anti-CB (n=6 mice) or anti-PV immunochemistry (n=7 mice). As previously shown (Suzuki and Bekkers 2010a), the average densities (cells/mm2) of SOM (235 ± 14) and CB cells (174 ± 27) were greater than PV cells (109 ± 9.0, p: 0.0054, KW-test, Figure 17A). Contrary to our expectations, the density of SOM interneurons consistently decreased along the RC axis in all animals. In the majority of mice (5/7), SOM cell densities had significantly negative slope values (filled blue circles, Figure 17B) and the distribution slopes significantly differed from 0 (p: 0.002, MW-test, Figure 17B). In addition, the average normalized density across all animals significantly decreased along the RC axis (slope: -0.25 ± 0.03, $p<0.0001$, Figure 17C). In contrast, CB and PV interneuron densities did not consistently vary along the RC axis. CB cell RC distributions were highly variable with individual mice showing significant increases (n=2), decreases (n=1) (filled green circles, Figure 17B) or no change (n=3) along the RC axis. The distribution of CB slopes did not differ from zero (p: 0.37, MW-test) and the average normalized density did not change with RC distance (slope: 0.07 ± 0.14, p: 0.61, Figure 17D). In 2/7 animals, PV cell density decreased significantly along the RC axis (filled black circles, Figure 17B) and strongly weighted the average normalized density across all animals resulting in a significant decrease (-0.25 ± 0.11, p: 0.048, Figure 17E). However, since the majority of mice

showed no change in RC distribution and the distribution of slopes did not differ from zero (p: 0.20, MW-test, Figure 17B), we conclude that PV cell density does not vary along the RC axis. Thus, it is unlikely that stronger caudal inhibition of PCs arises from a RC increase in the density of inhibitory interneurons.

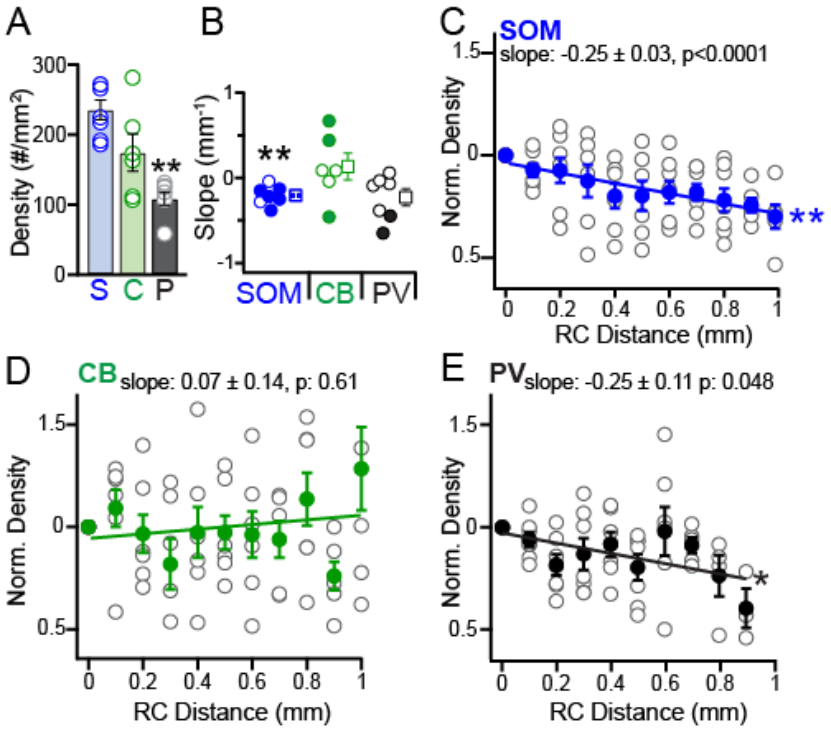

Figure 17. Distribution of Interneuron Subtypes along the Rostrocaudal Axis in Layer 3.

(A) Density of somatostatin, calbindin, and parvalbumin-positive interneurons in APC. (B) Distribution of slopes across each mouse and cell type for the distribution of cell density along the rostrocaudal axis in layer 3. (C) Density of somatostatin cells along the rostrocaudal axis across animals. Line indicated best fit. Points are sample mean for each position (D) As C, for calbindin cells. (E) As C, for parvalbumin cells. Error bars: S.E.M. *: p<0.05, **: p<0.01

Rather, it appears that a higher rostral density of SOM cells would provide stronger, rostrally-biased inhibition. We have previously shown that SST-cells inhibit both dPCs as well as the majority of L3 interneurons in APC (Large, Kunz, et al. 2016). Thus, SST cells could

underlie the rostrally-biased inhibition of L3 interneurons. To test this, we selectively expressed ChR2 in SST interneurons and repeated grid stimulation while recording IPSCs in L3 interneurons and dPCs (Figure 18A). As expected SST-cells provided rostrally-biased inhibition to the majority (73%) of L3 interneurons (bias: -0.11 ± 0.04, p: 0.02, n=22, Figure 18B1,2). Moreover, the average bias value did not significantly differ between VGAT-ChR2 and SOM-ChR2 animals (p: 0.69, unpaired t-test). Likewise, average rostral inhibition was significantly greater than caudal inhibition and was comparable in SST-ChR2 and VGAT-ChR2 mice (Figure 18D). Thus, activating solely SST-cells is sufficient to reproduce rostrally-biased inhibition in L3 interneurons, consistent with the higher density of SST cells in rostral APC. A lack of CB/PV activation had no apparent effect on RC biases in L3 interneurons.

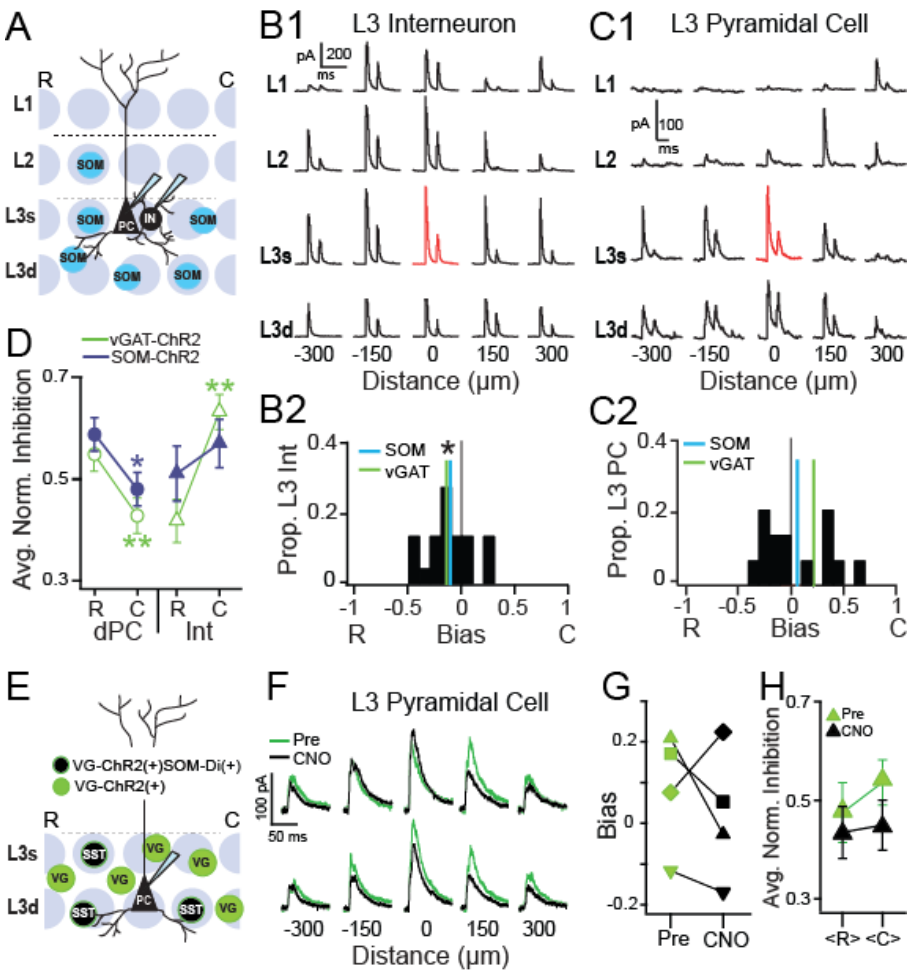

Figure 18. Somatostatin Cells Mediate Asymmetric Inhibition

(A) Schematic of experiment to optogenetically stimulate somatostatin cells. PC: Pyramidal Cell. IN: Interneuron. SOM: somatostatin cell. (B) responses in L3 interneurons. (B1) example IPSC traces. Red trace indicates stimulation at interneuron soma. (B2) distribution of bias values. Black line at zero. Blue line indicates mean bias under SOM-ChR2. Green line indicates mean bias under VGAT-ChR2. (C) As in B, for L3 pyramidal cells. (D) Comparison of rostral and caudal inhibition for L3 pyramidal cells and interneurons under VGAT-ChR2 and SOM-ChR2 (E) Schematic of experiment to optogenetically stimulate interneurons while chemogenetically silence somatostatin cells. VG: VGAT-ChR2 cell (F) example traces of a layer 3 pyramidal cells before (green) and after (black) CNO application. (G) Comparison of bias values before and after CNO application. (H) comparison of average rostral and caudal inhibition before and after CNO application. * $p<0.05$; ** $p<0.01$ Error Bars: S.E.M.

Stimulation of solely SST cells increased the percentage of PCs receiving rostrally-biased inhibition to 50% (n=7/14, Figure 18C1) compared to only ~13% (n=2/16) when all inhibition was recruited in vGAT-ChR2 animals. Across the dPC population, the spatial profile of inhibition was not coherently asymmetric with SOM-ChR2 activation (compare Figure 18C2 with Figure 15D3) and the distribution of bias values did not differ from zero (0.06 ± 0.08, p: 0.45, one sample t-test, Figure 18C2). Compared to inhibitory network recruitment in VGAT-ChR2 mice, rostral inhibition increases and caudal inhibition decreases such that rostral and caudal inhibition does not significantly differ (Figure 18D). These findings are consistent with both the preferential recruitment of higher rostral densities of SST cells and a lack of CB/PV inhibition.

It is interesting to note that the strength of SST-mediated inhibition in L3 interneurons did not significantly differ (6.82 ± 1.4 pA·s) from that in vGAT-ChR2 animals (7.02 ± 0.92 pA·s, p: 0.91, unpaired t-test). Although one should be cautious when comparing between transgenic lines due to different ChR2 expression regimes, one interpretation is that interneurons receive predominantly SST-mediated inhibition. Alternatively, inhibition of dPCs was significantly weaker (4.77 ± 0.89 pA·s) in SST-ChR2 mice than in vGAT-ChR2 (8.63 ± 0.84 pA·s, p: 0.003, unpaired t-test). This finding is expected if SST cells are only a subset of the interneurons providing inhibition to dPCs in vGAT-ChR2 animals. Thus, if SST-cells provide rostrally-biased inhibition to dPCs in VGAT-ChR2 mice, there must be mechanism by which other interneurons are able to provide sufficient caudally biased inhibition to dominate the network response.

One possibility is that SOM cells provide rostrally biased inhibition to interneurons and thus, rostrally disinhibit dPCs. To investigate this possibility, we bred triple transgenic animals (VGAT-ChR2::SOM:hDMi) in which all interneurons express ChR2 but only SOM cells express

the inhibitory DREADD, hm4Di (Figure 18E). This allows us to test the function of the inhibitory network in the absence of SST-cells when the DREADD agonist CNO (20 μM) is added to the bath. We performed grid stimulation while recording IPSCs in dPCs in the absence or presence CNO. Under normal conditions, the full inhibitory network is intact and dPCs receive caudally biased inhibition (bias: +0.08 ± 0.07, n=4, Figure 18F,G). Upon application of CNO, inhibition decreased at all sites consistent with a loss of SOM mediated inhibition. In the majority of dPCs, the loss of SOM-cell activity shifted bias values from caudal to neutral (Figure 18G) due to a greater reduction in caudal inhibition versus rostral inhibition (Figure 18H). Given the rostral bias in SOM-cell density and inhibition of dPCs, it is surprising that rostral inhibition is preserved in CNO. This suggests that rostral interneurons are normally suppressed by SOM cells but rebound during CNO application. Overall, these findings suggest a mechanism by which SOM cells inhibit interneurons and consequently disinhibit dPCs in a rostrally-biased manner. As the proportion of SOM cells decreases along the RC axis, a loss of disinhibition leads to an increase in direct inhibition of dPCs in caudal APC.

4.3.2 Rostral-caudal spatial profiles of neural activity

What role might RC patterning of inhibition play in olfactory processing? Odor evoked activity is distributed along the RC extent of the APC, but few studies have investigated RC patterning (Illig and Haberly 2003; Sugai et al. 2005; Stettler and Axel 2009; Rennaker et al. 2007). We measured the spatial distribution of neural activity in the APC in three conditions: exploration of a novel environment with novel odor (NEO), home cage with novel odor (HCO) or home cage no odor (HC) (Figure 19A). Briefly, FosCreERT2 mice were crossed with Ai14 mice to produce offspring that express a tamoxifen-dependent cre-recombinase under the promoter for the

activity dependent, immediate early gene c-fos (ref). In the presence of hydroxytamoxifen (4-OHT, 50 mg/kg), active neurons undergo recombination and are "tagged" by red fluorescent protein, tdTomato. The HC (n=6) and HCO (n=6) mice were given a single dose of 4-OHT and then returned immediately to the home cage. HCO mice could rest for 30 min, then exposed to odor in the home cage for 30 min. NEO mice (n=6) were given 4-OHT, rested for 30 min, then allowed to explore a novel environment plus odor for 30 min before being returned to the home cage. We find that mice were highly active during exploration the novel environment (Figure 19A2, schematic far right) and sampled both non- and odorized sides of the chamber throughout the 30 min exposure period (Figure 19A3). The majority of mice were exposed to isoamyl acetate (1:100 dilution in mineral oil) but one cohort of mice, (n=1 HC, n=2 HCO, n=1 NEO) were exposed to ethyl-butyrate. Animal behavior and neural activity patterns did not differ between odors and consequently, results were grouped. Following 4-OHT and odor exposure, all mice remained undisturbed in their home cages in the dark for 12 hours. Mice were sacrificed 5 days later for tissue sectioning. Neural activity was quantified as the density of tdTom(+) in laminar regions of interest (L2, L3 ROIs, Figure 19B) located directly under the LOT. Neurons were counted in alternate coronal sections corresponding to ~1.5 mm of the RC axis of APC and densities were normalized to the most rostral section for linear regression analysis. RC spatial patterning of active neurons was quantified as described for interneuron densities (Figure 17).

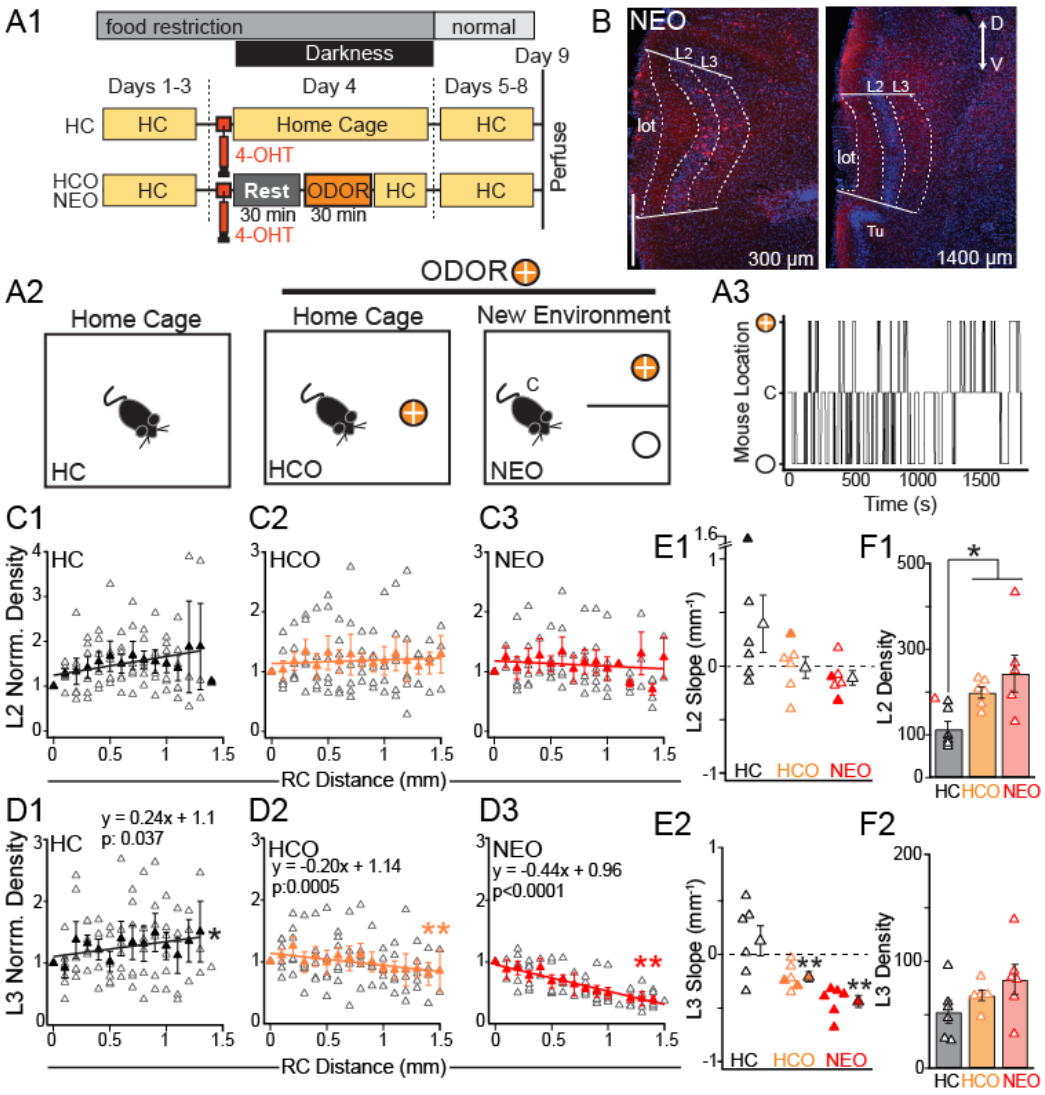

Figure 19. The Distribution of Active Neurons depends on Context.

(A) Experimental set up. (A1) Timeline of procedure. (A2) Diagram of environments for each condition. Open circle: chamber without odor. Circle with plus sign: chamber with an odor (A3) Mouse activity when inside the novel environment. (B) Histological sections showing expression of tdtomato from a mouse exposed to a novel environment with an odor. Blue staining: DAPI. (C) Normalized density of tdtomato-labeled cells in layer 2 along the rostrocaudal axis across animals for each condition. (D) As C, but for layer 3. (E) Distribution of slopes fit between tdtomato density and rostrocaudal distance for each condition in layer 2 (E1) and layer 3 (E2). (F) Distribution of average density for each condition in layer 2 (F1) and layer 3 (F2). Error Bars: S.E.M.

We found laminar differences in density as well as the RC spatial pattern of activity with odor exposure. In L2, the average density (cells/mm2) of tdTom(+) neurons was significantly greater in odor-exposed animals (NEO: 243 ± 43; HCO: 199 ± 13) than HC animals (113 ± 18 cells/mm2, p: 0.013 KW-test, Figure 19F1). Average density did not vary with condition in L3 (HC: 52 ± 11; HCO: 68 ± 5, and NEO: 83 ± 14 cells/mm2 , p: 0.149 KW-test, Figure 19F2). In contrast, the spatial patterning of tdtom(+) neurons along the RC-axis changed with odor exposure in L3 but not in L2 (Figure 19C,D,E). In L2, the spatial profile of neural activity was approximately uniform along the RC axis (Figure 19C). The distributions of slope values for individual animals did not significantly differ from zero (HC: 0.39 ± 0.27; HCO: -0.01 ± 0.10; NEO: -0.11 ± 0.07 mm-1, p: 0.065 - 0.38, MWU-test) or between conditions (p: 0.104 KW-test, Figure 19E1). However, in L3 there was significant RC patterning of neural activity that further differed between HC, HCO and NEO conditions (Figure 19D, E2). In the absence of novel odor, HC animals show inconsistent spatial patterning. The average normalized density across HC animals increased significantly with RC distance (slope 0.24 ± 0.10; p: 0.037, linear regression, Figure 19D1). However, in individual animals, linear regression slopes were positive (n=3), negative (n=2) or neutral (n=1) and the distribution of slopes did not significantly differ from zero (slope: 0.13 ± 0.14 mm-1, Figure 19E2). In odor-exposed animals (HCO and NEO), neural activity consistently decreased along the RC axis (Figure 19D2, D3). In animals exposed to odor in the home cage (HCO), the RC decrease in density was significant at the population level. The average normalized density across animals decreased significantly with RC distance (slope<0; p: 0.0005, linear regression, Figure 19D2). Likewise, the distribution of slope values was significantly non-zero (-0.21 ± 0.14 mm-1, **p: 0.005, MWU-test). But RC decreases were rarely significant in individual animals (n=2, filled orange triangles, Figure 19E2). In contrast, all

mice that experienced odor while exploring a novel environment (NEO) showed a significant decrease in activity along the RC axis (filled red triangles, slope distribution $\neq$ 0: -0.44 $\pm$ 0.14 mm-1, **p: 0.005, MWU-test, Figure 19E2). Further, the distribution of slope values was significantly more negative in NEO mice than HCO or HC (**, p: 0.0046, KW-test). Importantly, the total number cells indicated by DAPI nuclear stain either increased (n=2) or did not change along the RC axis (n=3). To summarize, we show that odor exposure increases the density of active neurons in L2 but not L3, and significantly changes the RC spatial patterning of neural activity in L3 but not L2.

We find that odor evoked neural activity (fos, tdtom(+) cells) in L3 decreases from rostral to caudal APC over a spatial scale of millimeters (Figure 19D2,3). We also find that inhibition of L3 dPCs increases from rostral to caudal on a similar spatial scale (Figure 15F). In Figure 20A we plot the average proportional decrease in active neurons in NEO mice and the average proportional increase in inhibition. Because there are only two points at 1.5 mm in Figure 15F, inhibitory strength was normalized to a projected "maximum" strength (8.17 pA·s) at 1.6 mm, based on the linear fit to inhibitory strength (Figure 15F). The spatial scales of neural activity and inhibition are well matched with opposing slopes (NEO: slope -0.44 ± 0.03 mm-1, R: 0.97, p<0.0001; Inhibition: slope 0.67 ± 0.06 mm-1, R: 0.98, p: 0.0001). Thus, when inhibition is weakest, neural activity is maximal and vice versa.

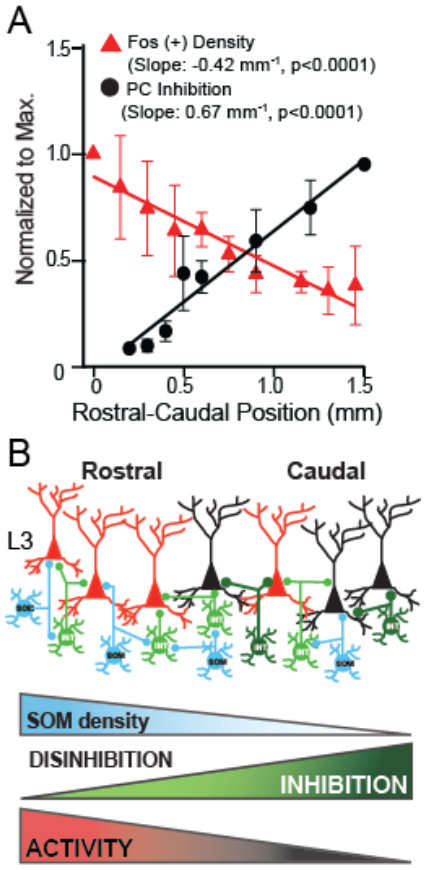

Figure 20. Summary.

(A) Comparison of change in inhibition onto pyramidal cells over rostrocaudal distance (black) with change in activity over rostrocaudal distance (red). (B) Circuit diagram summarizing findings (top) with schematic of opposing gradients (bottom).

In closing, we find that inhibition of dPCs in L3 increases along the rostral-caudal axis on the spatial scale of millimeters. This gradient of inhibition is supported by an opposing gradient of inhibition onto L3 interneurons mediated by SOM cells, which in turn, disinhibits rostral dPCs. We find that the spatial scales of inhibition are commensurate with RC decreases in the density of fos(+) neurons in L3 following odor exposure. These findings suggest that the recruitment of inhibitory gradients may underlie the RC patterning of neural activity in L3 of APC (Figure 20B). Further, the degrees of RC patterning may depend on the context of odor

exposure. Despite evidence for inhibitory gradients in L2 sPCs, the spatial profiles of neural activity are approximately uniform in L2 and only show odor evoked increases in average density of fos(+) neurons that do not seem to vary with odor context. Altogether, these laminar differences suggest spatially dependent and independent mechanisms work in parallel during odor processing in APC.

4.4 DISCUSSION

The APC extends ~2 mm along the ventral-lateral, rostral-caudal axis of the mouse brain. The APC is delineated from the PPC by the presence of the lateral olfactory tract (LOT) (Ekstrand et al. 2001). The LOT is comprised mitral (M) and tufted (T) cell afferents that carry odor information from the olfactory bulb. Individual MC axons give rise to collaterals along the extent of the LOT (Igarashi et al. 2012; Sosulski et al. 2011). Likewise, intracortical excitatory connections occur with uniform probability over mm distances within APC (Franks et al. 2011). These findings support distributed odor responses in piriform cortex (Stettler and Axel 2009; Poo and Isaacson 2011) and suggest excitatory circuits are homogeneous along the RC axis. Conversely, the efferent projections from the APC suggest a rostral PCs provide feedback to the OB and ascending input to the OFC (C.-F. F. Chen et al. 2014; Ekstrand et al. 2001; Padmanabhan et al. 2016), while caudal PCs project to the agranular insula. Finally, descending projections from entorhinal, OFC and AI are also spatially differentiated along the RC axis (Illig 2005; Lewis B. Haberly and Price 1978; Agster and Burwell 2009) These findings suggest additional organization exists within the APC that supports parallel pathways to higher and lower olfactory centers.

In this study, we use modern genetic approaches to demonstrate RC spatial patterning in inhibitory circuitry and the odor-evoked spatial profile of neural activity. Our findings reproduce earlier studies that have shown caudally-biased asymmetric inhibition of PCs in APC (Luna and Pettit 2010) and a RC decline in fos(+) neurons following odor exposure (Illig and Haberly 2003). However, the underlying circuit mechanisms and functional significance of these findings has yet to be determined. Here, we provide three significant advances. First, we delineate the inhibitory circuitry that underlies asymmetric inhibition in APC. Specifically, we find that SOM interneurons decrease in density along the RC-axis and provide strong rostrally-biased inhibition to L3 interneurons. This leads to the disinhibition of rostral PCs. Second, we show that RC patterning of neural activity is confined to L3 and differs with odor exposure in familiar (HCO) versus novel (NEO) contexts. Third, the decrease in active neurons along the RC axis following odor exposure is commensurate with increasing inhibition of dPCs. Specifically, rostral PCs are more active and receive significantly less inhibition whereas reduced caudal activity coincides with increased PC inhibition. Altogether, our findings provide new evidence for spatial organization within APC and a potential circuit mechanism for differentially regulating APC output to the OB and higher brain areas.

4.4.1 Spatial patterning of neural activity in APC.

The spatial patterning of population activity is technically difficult to investigate in vivo owing to the broad extent and ventral location of APC. Nearly all high-resolution methodologies, such as calcium imaging and unit recordings, under sample the RC-axis. Previous population calcium imaging shows minimal spatial variation in response to different odors or intensities, but only

samples ~300 μm of the RC axis limited to dorsal-caudal sites (Stettler and Axel 2009; Large, Vogler, et al. 2016; Suzuki and Bekkers 2011). Multi-site unit recordings broadly sample the RC axis and suggest RC variation in odor-evoked firing rates (Rennaker et al. 2007) but only sample a small proportion of neurons in a given region. Conversely, low-resolution intrinsic signal imaging or LFP recordings broadly sample the RC axis and suggest systematic variation along the RC-axis in concentration thresholds (Sugai et al. 2005) and oscillatory activity respectively (Freeman 1959). But these tools lack the spatial resolution to identify the underlying neurons and circuits contributing to these responses.

To investigate the spatial profiles neural activity in vivo, we used targeted recombination in active populations (TRAP) mice that link cre-recombinase expression to the immediate early gene, c-fos. This tool provides sufficient resolution and sampling to investigate the spatial profile of population activity along the entire RC axis at scales comparable to microcircuits within APC. TRAP-mice are advantageous because labeling does not depend on capturing a fleeting a nuclear fos signal. Rather, once released, cre-recombinase promotes continuous cytoplasmic expression of tdtom regardless of the initial strength of fos expression. The main limitation is that the temporal window for capturing activity is optimal within one hour of 4-OHT injection and declines significantly 6 hours post injection (Guenthner et al. 2013). Thus, neural densities are expected to be higher in TRAP animals due to enhanced labeling of weak responses and potential spurious labeling over long time windows. To minimize the latter, we inject mice 30 min before odor exposure and the animals are maintained undisturbed in the dark housing room for 10h following exposure. We surmise that fos(+) cells in HC animals represent baseline activity evoked by the HC environment, handling, injection and spurious activity.

Consistent with previous findings (Illig and Haberly 2003), the average density of fos(+) cells increases significantly in odor-exposed animals (HCO and NEO) compared to HC animals. However, we find changes in density are restricted to L2. In contrast, RC patterning of neural activity is solely found in L3 of HCO and NEO animals. A lack of RC patterning in L2 was initially surprising since L2 sPCs also receive caudally-biased inhibition. However, L2 sPCs receive weaker overall inhibition than L3 dPCs (Large, Vogler, et al. 2016) while L2 semilunar cells and interneurons do not receive asymmetric inhibition. This suggests that the distributed pattern of neural activity in L2 is inherited from the spatial profile of afferent and/or recurrent excitation rather than dictated by inhibition. In contrast, interneuron densities, particularly SOM cells, are greatest in L3 (Large, Kunz, et al. 2016; Suzuki and Bekkers 2010a). Individual L3 dPCs receive strong, caudally-biased inhibition but weak excitation (Large, Vogler, et al. 2016) while a majority L3 interneurons receive strong rostrally-biased inhibition from SOM-cells (Large, Kunz, et al. 2016). Moreover, we find that inhibition increases with the position L3 dPCs along the RC axis. These are ideal conditions for inhibition to dictate L3 RC activity patterns. These laminar differences in inhibition and RC patterning also coincide with layer-specific differences in projection to distinct target areas (Diodato et al. 2016), and further support the premise that parallel processing streams exist in APC.

Although a RC decrease in active L3 neurons was found in both groups of odor-exposed mice, spatial patterning of neural activity was strongest and most consistently found in animals exposed to a novel odor in all novel environment (NEO).

4.4.2 Disinhibition by Somatostatin Interneurons

Inhibition plays a critical role in the processing and representation of sensory information in the cortex (Isaacson and Scanziani 2011). In APC, inhibition balances excitation (Large, Vogler, et al. 2016; Sheridan et al. 2014; Suzuki and Bekkers 2012), narrows synaptic integration windows (Luna and Schoppa 2008; Suzuki and Bekkers 2012, 2010b; Franks et al. 2011; C. C. Stokes and Isaacson 2010), supports oscillatory activity (Atallah and Scanziani 2009), and sharpens odor tuning (Poo and Isaacson 2011; Sturgill and Isaacson 2015). Given the prominent role inhibition plays in shaping cortical responses, surprisingly few studies have focused on the circuits that modulate inhibition and potentially disinhibit pyramidal cells in APC. In neocortex, a number of disinhibitory circuits have been identified and implicated in the gating or tuning of cortical responses to sensory stimuli (Pfeffer et al. 2013; S. Lee et al. 2013; Xu et al. 2013; S.-H. Lee et al. 2012; Pi et al. 2013; Ibrahim et al. 2016; Muñoz et al. 2017). In particular, SOM cells inhibit a range of interneuron classes including fast spiking (FS) PV interneurons (Pfeffer et al. 2013; Xu et al. 2013). We, and others, have found that SOM-cells similarly inhibit FS interneurons (Large, Kunz, et al. 2016; Sturgill and Isaacson 2015) and other interneuron classes in APC (Large, Kunz, et al. 2016) and thus, potentially disinhibit PCs. In this study, we advance previous findings to show that SOM interneurons provide rostrally-biased inhibition to interneurons. We show that selective SOM activation or the removal of SOM cells from network inhibition neutralizes the caudally biased inhibitory gradient onto dPCs. In particular, chemogenetic inhibition of SOMs lead to rebound inhibition at rostral stimulation. These findings support a role for disinhibitory role for SOM cells in APC.

Recent studies have shown that SOM interneuron activity can be selectively enhanced by cholinergic modulation (N. Chen, Sugihara, and Sur 2015) or when an animal is running during

visual sensory stimulation (Cottam, Smith, and Häusser 2013). Moreover, one subclass of SOM cells, the fast-spiking, X94-like cells in L4 of S1 specifically increase firing rates when a mouse is actively whisking (Muñoz et al. 2017). These SOM cells are particularly interesting because they preferentially inhibit PV cells and potentially disinhibit PCs (Xu et al. 2013). We have recently found that nearly two-thirds of L3 SOM cells in APC are X94-like (Large, Kunz, et al. 2016). Moreover sniffing and whisking activity is strongly correlated (Kleinfeld, Deschênes, and Ulanovsky 2016; Ranade, Hangya, and Kepecs 2013). An intriguing possibility is that actively running, sniffing and whisking during exploration of a novel odor environment (NEO) strongly enhances SOM cell activity and gates RC patterning through SOM mediated disinhibition of dPCs.

4.4.3 Functional roles for RC asymmetries in olfactory processing

Given the seemingly uniform profile of excitation in APC, a surprising finding is that inhibitory strength increases along the rostral-caudal axis. Spatially asymmetric inhibition exists in other cortical areas (Beed et al. 2013). In entorhinal cortex, a dorsal-ventral inhibitory gradient coincides with an increase in PV interneuron density, changes in receptive field size and increased gamma oscillatory power. We find SOM cells rather than PV cells decrease in density along the RC axis. Since SOM cell inhibition has a subtractive effect on PC odor tuning (Sturgill and Isaacson 2015), it is possible that RC patterning of inhibition supports changes in odor response functions across the RC extent of APC. We propose that asymmetric inhibition via rostral disinhibition of PCs increases the density active neurons in the rostral APC while increased caudal inhibition decreases activity. Since spatial patterning of inhibition and neural activity is predominantly found in L3 dPCs that project out of APC (Diodato et al. 2016;

Padmanabhan et al. 2016; C.-F. F. Chen et al. 2014), an alternate role for RC patterning may be to dictate projection patterns out of the APC in different contexts. For example, higher rostral activity during exploration of a novel odor environment could preferentially increase feedback to the OB (Padmanabhan et al. 2016) or drive to the OFC (C.-F. F. Chen et al. 2014). Finally, it should be noted that there are other potential sources of RC patterning in neural activity in APC. For example, tufted cells projection from OB are limited to the rostral-ventral APC (Igarashi et al. 2012), descending inputs from frontal cortices (Ekstrand et al. 2001) and PPC (Neville and Haberly 2004) also show RC biases. It remains to be determined if the various sources of RC asymmetry work in concert during olfactory processing. Nonetheless, our study adds to a growing body of evidence that, despite the lack of a topographic code for odor identity, space is a relevant dimension for odor processing in of olfactory cortex.

5.0 CONCLUSION

5.1 DISTINCT MICROCIRCUITS IN PIRIFORM CORTEX

Our research has shown that the anterior piriform cortex has a high degree of functional heterogeneity. Rather than being a structure with homogenous connectivity (Igarashi et al. 2012; Franks et al. 2011) with a distributed, sparse coding scheme (Poo and Isaacson 2009; Stettler and Axel 2009), the APC seems to have a number of microcircuits, each potentially either own processing unit. To date, methodological limitations have prevented a comprehensive assessment of piriform cortex activity and circuitry. This is mainly due to the inconvenient location of the piriform cortex at the ventral surface of the mouse brain and its relatively large size. In vivo experiments, whether through extracellular recording or imaging studies, have a hard time sampling the entire extent of the piriform cortex. And even when they are able to record from piriform neurons, they would be biased toward layer 2 pyramidal cells, simply because layer 2 is the most cell dense layer. Therefore, these studies would attempt to assign a function to all of the APC based on the local configuration of layer 2 pyramidal cells. With the advent of the TRAP technology, we have been able to assess the activity of neurons during a defined time window and analyze the results post hoc. While the results are binary and we lose any temporal information, it still provides us with the ability to investigate activity across the rostrocaudal axis of the APC. In our results, layer 2 does not show a strong spatial bias of activity, with aligns well

with the homogenous piriform model established in the literature. Our electrophysiological results have shown that these L2 pyramidal cells primarily receive feedforward excitation. Therefore, from our data, L2 pyramidal cells look like they would represent odors as a reflection of the afferent input from the olfactory bulb. Layer 3 pyramidal cells, on the other hand, receive very little feedforward excitation, instead most of their input arrives from recurrent or feedback connections. Rather than lumping them with L2 pyramidal cells, it might be beneficial to consider that they are undergoing an additional layer of processing. Given that activity in layer 3 varies depending on the olfactory context, this seems to be a plausible hypothesis.

Not only do our results present intriguing ideas about the local processing units of the piriform cortex, it also highlights a possible mechanism by which the APC directs information flow to downstream cortices. This is not a novel idea – others have shown changes in projection patterns along the APC (Padmanabhan et al. 2016; C.-F. F. Chen et al. 2014; Diodato et al. 2016). While experiments were performed using anatomical tract tracing methods, demonstrating a physical connection between sections of piriform cortex and behaviorally relevant brain structures, we have approached this from the opposite angle and shown that behaviorally relevant contexts adjust the degree of activity in sections of piriform cortex. The piriform cortex does receive input from higher order brain structures, such as the OFC, insula, and entorhinal cortex (ILLIG 2005; Lewis B. Haberly and Price 1978; Agster and Burwell 2009; Chapuis et al. 2013; Linster and Cleland 2003), so it is highly likely there exists top-down modulation of piriform activity.

We have not only demonstrated laminar differences in microcircuitry in piriform cortex, we have also highlighted possibly distinct roles for somatostatin cells. It has been known that there are different subtypes of somatostatin cells (McGarry et al. 2010; Y. Ma et al. 2006), we

were interested in whether these subtypes exist in the APC. As in neocortex, we can broadly classify SST cells as either fast-spiking or regular-spiking. It has recently been shown that FS and RS SST cells perform different functions during whisking (Muñoz et al. 2017). In their research, they found that Martinotti (prototypical GIN) cells reduce their firing during whisking, while non-Martinotti cells in layer 4 increase their firing during whisking. This goes further, as Martinotti cells canonically inhibit pyramidal cells (Y. Ma et al. 2006), whereas the non-Martinotti cells target parvalbumin cells, ultimately disinhibiting pyramidal cells during whisking (Xu et al. 2013). While we find that somatostatin cells in APC target other interneurons, including other somatostatin cells, we do not yet know if there are subtype-specific projections and thus also provide distinct microcircuits.

Still, there is another question about microcircuitry: what regulates somatostatin cells? One of the most enticing possible regulators of somatostatin cells are interneurons expressing vasoactive intestinal peptide (VIP) (Muñoz et al. 2017; Pi et al. 2013; S.-H. Lee et al. 2012; S. Lee et al. 2013; Pfeffer et al. 2013; Jiang et al. 2015; Urban-Ciecko and Barth 2016). VIP cells have been shown to specifically target other interneurons, making them "dedicated disinhibitors." Of all of the postsynaptic targets for VIP neurons, SST cells seem to be their most common target (Pfeffer et al. 2013). However, much of this work has either been agnostic to differences in subtypes of somatostatin cells or specially target GIN cells. Fitting in the connection between VIP and SST interneurons along with our results expands the range of conclusions we can draw about how the piriform cortex responds to odors. VIP cells seem to preferentially target GIN cells (Muñoz et al. 2017), meaning that our non-GIN cells could be the performing the activity gradient while the VIP cells are performing plasticity mechanisms, by way of GIN (or equivalent) cells. VIP cells are known to be upregulated by neuromodulators,

including acetylcholine and serotonin (S.-H. Lee et al. 2012; Poorthuis, Enke, and Letzkus 2014; Pakan et al. 2017; Y. Fu et al. 2014).. Both of these neuromodulators are associated with attentional processing (Klinkenberg, Sambeth, and Blokland 2011; Wingen et al. 2008). This means that VIP is tightly controlled by the behavioral state of the animal (Pakan et al. 2017). It would appear that increasing attention would upregulated VIP cell activity, resulting in a downregulation of somatostatin cell activity, ultimately disinhibiting pyramidal cells (S. Lee et al. 2013; Muñoz et al. 2017; Urban-Ciecko and Barth 2016; Pi et al. 2013; S.-H. Lee et al. 2012).

5.2 THE BIGGER PICTURE: THE ROLE OF PIRIFORM IN BEHAVIOR

An argument that can be made is that sensation is how an organism takes input about the world, assigns meaning to it, and then uses that meaning to perform some action. For a mouse, olfaction seems to be a critical sense – the sense of smell allows them to navigate through the world and recognize food, friends, and foes. Given this, it would stand to reason that the olfactory cortex would be sensitive to contextual cues. Moreover, given the relatively large size of the olfactory cortex, it would benefit the animal to develop functional subdomains within the cortex to improve parallel processing.

5.2.1 Beyond the Piriform: Top-Down Modulation of Olfactory Processing

It would be unextraordinary to claim that animals use sensory inputs in order to understand their environment and make decisions about their survival using those sensory inputs. That is

something embedded in the very definition of life itself. Taken this into account then, it should be no surprise that the brain's response to sensory experiences should vary based on situational context. In our data, we see that layer 3 interneurons show two different spatial patterns of activity: a homogenous one activity pattern in their home cage and a rostrally biased activity pattern in a novel odor environment. This novel odor environment is the combination of an unfamiliar odor in an unfamiliar setting with different tactile, auditory, and visual cues. The rostral bias of activity is greatly diminished if the animal is presented with an unfamiliar odor in its own home cage. This lends evidence that the anterior piriform cortex is not only representing olfactory stimuli in an inhomogeneous manner, but it is also considering the non-olfactory context. From an ethological standpoint, being in a novel environment should induce certain exploratory drives in an animal that would not be seen to the same extent in the familiar territory of its home. Putting these two thoughts together, and we can predict that behavioral would play a role in determining how information is propagated through the brain, but also the plasticity of these connections. Having functional subdomains of the APC would seem to be useful, although we don't yet know what exactly what processing may be going on in these areas. However, one way to address this is to investigate the downstream targets of the APC. It has been shown that rostral APC is more likely to send axons back to the bulb or to the OFC, whereas caudal is more likely to send axons to the agranular insula (Padmanabhan et al. 2016; C.-F. F. Chen et al. 2014). Unfortunately, attempting to ascribe function to prefrontal regions is even more dangerous than doing so in piriform cortex. Still, an ethologically-inspired interpretation would be that novel environments would be more stimulating for the animal and require greater investigation. This would mean further olfactory processing would be needed (hence the feedback to the bulb) as well as increased cognitive functioning. Since the agranular insula seems to be involved in

reward processing (Kesner and Gilbert 2007), a novel environment would not send any signal about an incoming reward, so that functional connection is not as strong. The idea that the piriform can reroute information, depending on where it is needed, is a very seductive proposition.

Another top-down realm worth discussing is the role of attention on olfactory processing. We have already discussed that neuromodulators may be key in understanding the APC. And since neuromodulators are associated with attention (Klinkenberg, Sambeth, and Blokland 2011; Wingen et al. 2008), we may have a way to speak towards attention on a neural circuit level. This has already been investigated in neocortex, especially in reference to regulation of VIP and SST neurons based on behavioral state (Y. Fu et al. 2014; S. Lee et al. 2013; Pakan et al. 2017; Poorthuis, Enke, and Letzkus 2014). Acetylcholine has been shown to be useful in promoting plasticity in olfactory cortex (D. A. Wilson 2001; Donald A. Wilson, Fletcher, and Sullivan 2004; Hasselmo et al. 1990). Since acetylcholine has been extensively studied in reference to learning, we will focus on that in the next subsection.

5.2.2 Implications for learning and memory

By using attention as a lens to view our circuit mapping results, we can see a few ways to link behavioral state, environmental context, and cortical processing. For instance, we have seen that the regulation of pyramidal cell activity is regulated by somatostatin cells. Furthermore, somatostatin cells are commonly inhibited by VIP cells. VIP cells, in turn, are upregulated by acetylcholine and serotonin, neuromodulators associated with attention. Thus, our findings also provide a way for us to possibly explain the role of attention on learning and memory.

One of the biggest questions in neuroscience is the location and mechanism of memory in the brain. The nature of memory has eluded philosophers, natural scientists, biologists, and psychologists for centuries. In fact, our notions of memory still bear a resemblance to those proposed by Aristotle, in which our brains are a blank slate, shaped by memories as if impressions onto wax (Gluck, Mercado, and Myers 2013). However, given that the brain exists in a physical space, some, such as Richard Semon, have argued that memory should a physical manifestation (Schacter 2001). He referred to this as the "engram" (Semon 1921). Several neuroscientists have made major contributions to the search for the engram. It should be noted that the word "memory" can be used in a couple different contexts: some use it in the phenomenological sense, as in the cognitive aspect of remembering, while others speak of biological memory of cells and synapses. Trying to link the two is beyond the scope of our research. For our purposes, we will focus on synaptic plasticity as a form of memory. Donald Hebb, proposed the idea that "neurons that fire together, wire together", implying if a stimulus were to co-activate a certain set of neurons, those neurons would become more strongly connected to each other (Hebb 2002). This is likely a major component for memory formation. Specifically, that the synaptic connections between neurons are plastic and the strength of these connections are readily modified as an experience-driven neural activity.

The piriform cortex is an excellent model for plasticity, as it does not represent odors de novo; instead the piriform represents odors as a sparse population code, with learning pushing a collection of neurons to increase association with each other, forming neuronal assemblies. (Choi et al. 2011; Shakhawat and Gheidi 2014; Donald A. Wilson 2009; Donald A. Wilson and Rennaker 2010; L. B. Haberly 2001; Bao et al. 2016; Földiak 2002; Poo and Isaacson 2009). Because of this, the piriform cortex is an excellent model of associative plasticity – that is,

increasing the strength of recurrent inputs between pyramidal cells such that they are more likely to fire together in the future (E. Kanter and Haberly 1993; E. D. Kanter, Kapur, and Haberly 1996; Barrionuevo and Brown 1983). In piriform cortex, it has been shown that associative plasticity is difficult to induce in vitro without either blocking GABA transmission (E. Kanter and Haberly 1993) or in the presence of acetylcholine agonists (Patil et al. 1998). These results may now be explained by our results. Given that acetylcholine targets VIP interneurons (Poorthuis, Enke, and Letzkus 2014; Pakan et al. 2017; Y. Fu et al. 2014) and VIP interneurons target a subtype of SST cells, reducing inhibition onto pyramidal cells (Pfeffer et al. 2013; Jiang et al. 2015; Urban-Ciecko and Barth 2016; S. Lee et al. 2013; Muñoz et al. 2017), this would be parsimonious explanation to the associative plasticity data. This is further supported by the fact that GABA blockade only needs to be at the pyramidal cell dendrite, suggesting that inhibition by somatostatin cells is gating plasticity in the APC (E. Kanter and Haberly 1993).

5.3 ALTERNATIVE EXPLANATIONS

It is important to note that while the interpretations we have provided here are parsimonious with our data, it is not to the exclusion of other possible explanations. The piriform cortex is host to several microcircuits, each with the potential to perform many possibly overlapping roles, and to ascribe a function to any given circuit in a one-to-one manner is somewhat myopic.

In terms of understanding the spatial properties of olfactory event coding in piriform cortex, we primarily focused on layer 3, briefly touching on layer 2. Because we find that the rostrocaudal gradient of activity and inhibition seems to be in layer 3, we chose not to dwell on apparent lack of gradient in layer 2. Regardless, this is not to say that layer 2 does not play a role in regulating

the activity in piriform cortex. Rather, we are claiming the role of layer 2 is likely invariant to the relative position of the cells along the rostrocaudal axis of the APC.

Furthermore, we have completely ignored layer 1 interneurons in this discussion. This is largely because layer 1 interneurons are mediated feedforward inhibition based on olfactory bulb input. However, this is not to say they may play a role in regulating the activity of APC pyramidal cells. Regardless of whether other inhibitory circuits are agnostic to a spatial axis in APC, they are undeniably mediating the activity of piriform pyramidal cells. Not only should we be careful to not ignore the possible contribution of other inhibitory circuits in regulating the activity of piriform pyramidal cells in an isolated sense, but we need to be especially careful in evaluating how these circuits interact with each other.

Finally, we have thus far discussed inhibitory circuitry in a framework whereby interneurons act as a gatekeeper for activity. While this framework has had long-standing support in the piriform cortex and in neuroscience in general, it is possible to ignore emergent properties of the network. As mentioned previously, these circuits interact with each other, in a manner that is dependent on spatial location, timing, and behavioral state. The interpretation of interneurons as a kind of toggle switch then is likely accurate to a first approximate, but may be more crude than we may think. Rather, there is some evidence that these types of circuits are better interpreted in a dynamical systems framework.

5.4 FUTURE DIRECTIONS

The results shown here form the foundation for what is sure to be a very exciting line of research. While our activity-related data shows that context matters for the space-dependent

recruitment of neurons in APC and our circuit-level data demonstrate a possible neural substrate for this spatial dependence, an obvious next step would be to demonstrate that the circuitry contributes to the spatial patterns of activity we witness. If we are to suppose that the gradient in inhibition we see in slice is responsible for the gradient in activity we see in the fos-TRAP data, then disrupting somatostatin activity during exposure to a novel olfactory environment should produce fos labelling similar to that of home cage controls. DREADDs technology is a relatively non-invasive way to disrupt the activity of a particular neuron class. We could then use DREADDs or another inhibitory molecule to prevent somatostatin activity and measure the distance-dependence of the resulting fos data.

Furthermore, one missing element in our research is applying the knowledge of specific subtypes of SST cells to our inhibitory gradient data. If we were to tie expression of channelrhodopsin to subtypes of SST, we may be able to understand which somatostatin cell is primarily responsible for generating the inhibitory gradient onto interneurons. This is especially important for understanding how VIP works, as it may be that VIP is specifically targeting SST cells that target pyramidal cells, and not SST cells that target other interneurons, as it seems to be in the neocortex (Muñoz et al. 2017).

As previously mentioned, the APC projects to several cortical regions in a spatially-dependent manner (Padmanabhan et al. 2016; N. Chen, Sugihara, and Sur 2015; Diodato et al. 2016). If we suspect that the fos-related activity is in some way related to information flow, we could combine our fos experiments with retrograde tracing and immunohistochemistry to measure the overlap between active neurons and their projection targets.

Finally, our experiments touched upon the role of situational context and behavioral state in the recruitment of APC neurons. Further investigation into this may prove to be very fruitful.

Given that our behavioral experiments were fairly unexciting for the animal, it would be extremely interesting to investigate if fos-related activity was task-dependent. If our model is correct and that the rostrocaudal variance in activity is due to recruitment of behaviorally relevant subdomains of piriform cortex, a task that involves valent stimuli, such as reward or punishment, or decision making, such as olfactory generalization or discrimination, should recruit the pertinent subdomains. By exploring a breadth of conditions would help elucidate how piriform may be representing odors. But more so than that, we can present several mice with the task, and measure fos activity at different time points along the task learning process. In such a way, we may be able to see whether these effects are learning-dependent and how the representations of odor across the rostrocaudal axis of the APC may change over learning.

Our results can lead to several different avenues in the future. Thanks to technological developments, we can finally start investigating the entirety of the piriform cortex, and at the same time determine how to divide it up. Our hope is that in the near future, we may understand what roles the piriform cortex is playing, and the neural substrates by which it carries out those roles.

BIBLIOGRAPHY

Adesnik, H., W. Bruns, H. Taniguchi, Z. J. Huang, and M. Scanziani. 2012. “A Neural Circuit for Spatial Summation in Visual Cortex.” *Nature* 490 (7419): 226–31.

Agster, Kara L., and Rebecca D. Burwell. 2009. “CORTICAL EFFERENTS OF THE PERIRHINAL, POSTRHINAL, AND ENTORHINAL CORTICES OF THE RAT.” *Hippocampus* 19 (12): 1159–86. doi:10.1002/hipo.20578.

Ascoli, Giorgio A., Lidia Alonso-Nanclares, Stewart A. Anderson, German Barrionuevo, Ruth Benavides-Piccione, Andreas Burkhalter, György Buzsáki, et al. 2008. “Petilla Terminology: Nomenclature of Features of GABAergic Interneurons of the Cerebral Cortex.” *Nature Reviews Neuroscience* 9 (7): 557–68. doi:10.1038/nrn2402.

Atallah, Bassam V., and Massimo Scanziani. 2009. “Instantaneous Modulation of Gamma Oscillation Frequency by Balancing Excitation with Inhibition.” *Neuron* 62 (4): 566–77. doi:10.1016/j.neuron.2009.04.027.

Bao, Xiaojun, Louise LG Raguet, Sydni M. Cole, James D. Howard, and Jay A. Gottfried. 2016. “The Role of Piriform Associative Connections in Odor Categorization.” *eLife* 5 (April): e13732. doi:10.7554/eLife.13732.

Bar-Ilan, Lital, Albert Gidon, and Idan Segev. 2013. “The Role of Dendritic Inhibition in Shaping the Plasticity of Excitatory Synapses.” *Frontiers in Neural Circuits* 6. doi:10.3389/fncir.2012.00118.

Barrionuevo, German, and Thomas H. Brown. 1983. “Associative Long-Term Potentiation in Hippocampal Slices.” *Proceedings of the National Academy of Sciences* 80 (23): 7347–51.

Bathellier, Brice, Troy W. Margrie, and Matthew E. Larkum. 2009. “Properties of Piriform Cortex Pyramidal Cell Dendrites: Implications for Olfactory Circuit Design.” *Journal of Neuroscience* 29 (40): 12641–52. doi:10.1523/JNEUROSCI.1124-09.2009.

Beed, Prateep, Anja Gundlfinger, Sophie Schneiderbauer, Jie Song, Claudia Böhm, Andrea Burgalossi, Michael Brecht, Imre Vida, and Dietmar Schmitz. 2013. “Inhibitory Gradient along the Dorsoventral Axis in the Medial Entorhinal Cortex.” *Neuron* 79 (6): 1197–1207. doi:10.1016/j.neuron.2013.06.038.

Bekkers, J. M., and N. Suzuki. 2013. “Neurons and Circuits for Odor Processing in the Piriform Cortex.” *Trends Neurosci* 36 (7): 429–38.

Biedenbach, M. A., and C. F. Stevens. 1969. “Synaptic Organization of Cat Olfactory Cortex as Revealed by Intracellular Recording.” *Journal of Neurophysiology* 32 (2): 204–14.

Biedenbach, M. A., and Charles F. Stevens. 1966. “Intracellular Postsynaptic Potentials and Location of Synapses in Pyramidal Cells of the Cat Olfactory Cortex.” *Nature* 212 (5060): 361–62. doi:10.1038/212361a0.

Birjandian, Z., C. Narla, and M. O. Poulter. 2013. “Gain Control of Gamma Frequency Activation by a Novel Feed Forward Disinhibitory Loop: Implications for Normal and Epileptic Neural Activity.” *Front Neural Circuits* 7: 183.

Buzsáki, György. 1984. “Feed-Forward Inhibition in the Hippocampal Formation.” *Progress in Neurobiology* 22 (2): 131–53. doi:10.1016/0301-0082(84)90023-6.

Cabezas, Carolina, Theano Irinopoulou, Bruno Cauli, and Jean Christophe Poncer. 2013. “Molecular and Functional Characterization of GAD67-Expressing, Newborn Granule Cells in Mouse Dentate Gyrus.” *Frontiers in Neural Circuits* 7 (April). doi:10.3389/fncir.2013.00060.

Casale, Amanda E., Amanda J. Foust, Thierry Bal, and David A. McCormick. 2015. “Cortical Interneuron Subtypes Vary in Their Axonal Action Potential Properties.” *The Journal of Neuroscience* 35 (47): 15555–67. doi:10.1523/JNEUROSCI.1467-13.2015.

Chapuis, Julie, Yaniv Cohen, Xiaobin He, Zhijan Zhang, Sen Jin, Fuqiang Xu, and Donald A. Wilson. 2013. “Lateral Entorhinal Modulation of Piriform Cortical Activity and Fine Odor Discrimination.” *Journal of Neuroscience* 33 (33): 13449–59. doi:10.1523/JNEUROSCI.1387-13.2013.

Chapuis, Julie, and Donald A. Wilson. 2012. “Bidirectional Plasticity of Cortical Pattern Recognition and Behavioral Sensory Acuity.” *Nature Neuroscience* 15 (1): 155–61. doi:10.1038/nn.2966.

Chattopadhyaya, Bidisha, Graziella Di Cristo, Hiroyuki Higashiyama, Graham W. Knott, Sandra J. Kuhlman, Egbert Welker, and Z. Josh Huang. 2004. “Experience and Activity-Dependent Maturation of Perisomatic GABAergic Innervation in Primary Visual Cortex during a Postnatal Critical Period.” *Journal of Neuroscience* 24 (43): 9598–9611. doi:10.1523/JNEUROSCI.1851-04.2004.

Chattopadhyaya, Bidisha, Graziella Di Cristo, Cai Zhi Wu, Graham Knott, Sandra Kuhlman, Yu Fu, Richard D. Palmiter, and Z. Josh Huang. 2007. “GAD67-Mediated GABA Synthesis and Signaling Regulate Inhibitory Synaptic Innervation in the Visual Cortex.” *Neuron* 54 (6): 889–903. doi:10.1016/j.neuron.2007.05.015.

Chen, Chien-Fu F., Dong-Jing Zou, Clara G. Altomare, Lu Xu, Charles A. Greer, and Stuart J. Firestein. 2014. “Nonsensory Target-Dependent Organization of Piriform Cortex.”

Proceedings of the National Academy of Sciences of the United States of America 111 (47): 16931–36. doi:10.1073/pnas.1411266111.

Chen, Naiyan, Hiroki Sugihara, and Mriganka Sur. 2015. "An Acetylcholine-Activated Microcircuit Drives Temporal Dynamics of Cortical Activity." *Nature Neuroscience* 18 (6): 892–902. doi:10.1038/nn.4002.

Chen, Simon X., An Na Kim, Andrew J. Peters, and Takaki Komiyama. 2015. "Subtype-Specific Plasticity of Inhibitory Circuits in Motor Cortex during Motor Learning." *Nature Neuroscience* 18 (8): 1109–15. doi:10.1038/nn.4049.

Chiu, Chiayu Q., Gyorgy Lur, Thomas M. Morse, Nicholas T. Carnevale, Graham CR Ellis-Davies, and Michael J. Higley. 2013. "Compartmentalization of GABAergic Inhibition by Dendritic Spines." *Science* 340 (6133): 759–62.

Choi, Gloria B., Dan D. Stettler, Benjamin R. Kallman, Shakthi T. Bhaskar, Alexander Fleischmann, and Richard Axel. 2011. "Driving Opposing Behaviors with Ensembles of Piriform Neurons." *Cell* 146 (6): 1004–15. doi:10.1016/j.cell.2011.07.041.

Cottam, James C. H., Spencer L. Smith, and Michael Häusser. 2013. "Target-Specific Effects of Somatostatin-Expressing Interneurons on Neocortical Visual Processing." *The Journal of Neuroscience* 33 (50): 19567–78. doi:10.1523/JNEUROSCI.2624-13.2013.

Cummings, SL, and Y Neuropeptide. 1997. "Somatostatin, and Cholecystokinin of the Anterior Piriform Cortex." *Cell Tissue Res* 289 (1): 39–51.

Davison, I. G., and M. D. Ehlers. 2011. "Neural Circuit Mechanisms for Pattern Detection and Feature Combination in Olfactory Cortex." *Neuron* 70 (1): 82–94.

Demir, Rezan, Lewis B. Haberly, and Meyer B. Jackson. 1998. "Voltage Imaging of Epileptiform Activity in Slices From Rat Piriform Cortex: Onset and Propagation." *Journal of Neurophysiology* 80 (5): 2727–42.

———. 2001. "Epileptiform Discharges With In-Vivo-Like Features in Slices of Rat Piriform Cortex With Longitudinal Association Fibers." *Journal of Neurophysiology* 86 (5): 2445–60.

Diodato, Assunta, Marion Ruinart de Brimont, Yeong Shin Yim, Nicolas Derian, Sandrine Perrin, Juliette Pouch, David Klatzmann, Sonia Garel, Gloria B. Choi, and Alexander Fleischmann. 2016. "Molecular Signatures of Neural Connectivity in the Olfactory Cortex." *Nature Communications* 7 (July): 12238. doi:10.1038/ncomms12238.

Ekstrand, Jeffrey J., Mark E. Domroese, Dawn M.G. Johnson, Sherry L. Feig, Susan M. Knodel, Mary Behan, and Lewis B. Haberly. 2001. "A New Subdivision of Anterior Piriform Cortex and Associated Deep Nucleus with Novel Features of Interest for Olfaction and Epilepsy." *The Journal of Comparative Neurology* 434 (3): 289–307. doi:10.1002/cne.1178.

Fino, E, and R Yuste. 2011. “Dense Inhibitory Connectivity in Neocortex.” *Neuron* 69 (6): 1188–1203. doi:10.1016/j.neuron.2011.02.025.

Földiak, Peter. 2002. *Sparse Coding In The Primate Cortex*.

Franks, K. M., M. J. Russo, D. L. Sosulski, A. A. Mulligan, S. A. Siegelbaum, and R. Axel. 2011. “Recurrent Circuitry Dynamically Shapes the Activation of Piriform Cortex.” *Neuron* 72 (1): 49–56.

Freeman, W. J. 1959. “Distribution in Time and Space of Prepyriform Electrical Activity.” *Journal of Neurophysiology* 22 (November): 644–65.

Fu, Y., J. M. Tucciarone, J. S. Espinosa, N. Sheng, D. P. Darcy, R. A. Nicoll, Z. J. Huang, and M. P. Stryker. 2014. “A Cortical Circuit for Gain Control by Behavioral State.” *Cell* 156 (6): 1139–52.

Fu, Yu, Megumi Kaneko, Yunshuo Tang, Arturo Alvarez-Buylla, and Michael P. Stryker. 2015. “A Cortical Disinhibitory Circuit for Enhancing Adult Plasticity.” *eLife* 4 (January): e05558. doi:10.7554/eLife.05558.

Gabernet, Laetitia, Shantanu P. Jadhav, Daniel E. Feldman, Matteo Carandini, and Massimo Scanziani. 2005. “Somatosensory Integration Controlled by Dynamic Thalamocortical Feed-Forward Inhibition.” *Neuron* 48 (2): 315–27.

Gavrilovici, Cezar, Sabrina D’Alfonso, Mathew Dann, and Michael O. Poulter. 2006. “Kindling-Induced Alterations in GABAA Receptor-Mediated Inhibition and Neurosteroid Activity in the Rat Piriform Cortex.” *European Journal of Neuroscience* 24 (5): 1373–84. doi:10.1111/j.1460-9568.2006.05012.x.

Gavrilovici, Cezar, Sabrina D’Alfonso, and Michael O. Poulter. 2010. “Diverse Interneuron Populations Have Highly Specific Interconnectivity in the Rat Piriform Cortex.” *The Journal of Comparative Neurology* 518 (9): 1570–88. doi:10.1002/cne.22291.

Giridhar, Sonya, Brent Doiron, and Nathaniel N. Urban. 2011. “Timescale-Dependent Shaping of Correlation by Olfactory Bulb Lateral Inhibition.” *Proceedings of the National Academy of Sciences of the United States of America* 108 (14): 5843–48. doi:10.1073/pnas.1015165108.

Gluck, Mark A., Eduardo Mercado, and Catherine E. Myers. 2013. *Learning and Memory: From Brain to Behavior*. Palgrave Macmillan.

Gottfried, Jay A., Joel S. Winston, and Raymond J. Dolan. 2006. “Dissociable Codes of Odor Quality and Odorant Structure in Human Piriform Cortex.” *Neuron* 49 (3): 467–79. doi:10.1016/j.neuron.2006.01.007.

Graupner, Michael, and Alex D. Reyes. 2013. “Synaptic Input Correlations Leading to Membrane Potential Decorrelation of Spontaneous Activity in Cortex.” *Journal of Neuroscience* 33 (38): 15075–85. doi:10.1523/JNEUROSCI.0347-13.2013.

Guenthner, Casey J., Kazunari Miyamichi, Helen H. Yang, H. Craig Heller, and Liqun Luo. 2013. “Permanent Genetic Access to Transiently Active Neurons via TRAP: Targeted Recombination in Active Populations.” *Neuron* 78 (5): 773–84. doi:10.1016/j.neuron.2013.03.025.

Haberly, L. B. 2001. “Parallel-Distributed Processing in Olfactory Cortex: New Insights from Morphological and Physiological Analysis of Neuronal Circuitry.” *Chem Senses* 26 (5): 551–76.

Haberly, L. B., and J. M. Bower. 1989. “Olfactory Cortex: Model Circuit for Study of Associative Memory?” *Trends Neurosci* 12 (7): 258–64.

Haberly, Lewis B., and Joseph L. Price. 1977. “The Axonal Projection Patterns of the Mitral and Tufted Cells of the Olfactory Bulb in the Rat.” *Brain Research* 129 (1): 152–57. doi:10.1016/0006-8993(77)90978-7.

———. 1978. “Association and Commissural Fiber Systems of the Olfactory Cortex of the Rat. I. Systems Originating in the Piriform Cortex and Adjacent Areas.” *The Journal of Comparative Neurology* 178 (4): 711–40.

Haberly, Lewis, and Mary Behan. 1983. “Structure of the Piriform Cortex of the Opossum. III. Ultrastructural Characterization of Synaptic Terminals of Association and Olfactory Bulb Afferent Fibers.” *The Journal of Comparative Neurology* 219 (4): 448–60. doi:10.1002/cne.902190406.

Hagiwara, Akari, Sumon K. Pal, Tomokazu F. Sato, Martin Wienisch, and Venkatesh N. Murthy. 2012. “Optophysiological Analysis of Associational Circuits in the Olfactory Cortex.” *Frontiers in Neural Circuits* 6 (April). doi:10.3389/fncir.2012.00018.

Hansel, David, and Carl van Vreeswijk. 2012. “The Mechanism of Orientation Selectivity in Primary Visual Cortex without a Functional Map.” *Journal of Neuroscience* 32 (12): 4049–64. doi:10.1523/JNEUROSCI.6284-11.2012.

Hasselmo, M. E., M. A. Wilson, B. P. Anderson, and J. M. Bower. 1990. “Associative Memory Function in Piriform (Olfactory) Cortex: Computational Modeling and Neuropharmacology.” *Cold Spring Harb Symp Quant Biol* 55: 599–610.

Hebb, D. O. 2002. *The Organization of Behavior: A Neuropsychological Theory*. Taylor & Francis.

Hu, Hang, John Z. Cavendish, and Ariel Agmon. 2013. “Not All That Glitters Is Gold: Off-Target Recombination in the somatostatin–IRES-Cre Mouse Line Labels a Subset of Fast-Spiking Interneurons.” *Frontiers in Neural Circuits* 7. doi:10.3389/fncir.2013.00195.

Hu, Hua, Jian Gan, and Peter Jonas. 2014. “Fast-Spiking, Parvalbumin+ GABAergic Interneurons: From Cellular Design to Microcircuit Function.” *Science* 345 (6196): 1255263. doi:10.1126/science.1255263.

Ibrahim, Leena A., Lukas Mesik, Xu-ying Ji, Qi Fang, Hai-fu Li, Ya-tang Li, Brian Zingg, Li I. Zhang, and Huizhong Whit Tao. 2016. “Cross-Modality Sharpening of Visual Cortical Processing through Layer-1-Mediated Inhibition and Disinhibition.” *Neuron* 89 (5): 1031–45. doi:10.1016/j.neuron.2016.01.027.

Igarashi, Kei M., Nao Ieki, Myungho An, Yukie Yamaguchi, Shin Nagayama, Ko Kobayakawa, Reiko Kobayakawa, et al. 2012. “Parallel Mitral and Tufted Cell Pathways Route Distinct Odor Information to Different Targets in the Olfactory Cortex.” *Journal of Neuroscience* 32 (23): 7970–85. doi:10.1523/JNEUROSCI.0154-12.2012.

Illig, K. R., and L. B. Haberly. 2003. “Odor-Evoked Activity Is Spatially Distributed in Piriform Cortex.” *J Comp Neurol* 457 (4): 361–73.

ILLIG, KURT R. 2005. “Projections from Orbitofrontal Cortex to Anterior Piriform Cortex in the Rat Suggest a Role in Olfactory Information Processing.” *The Journal of Comparative Neurology* 488 (2): 224–31. doi:10.1002/cne.20595.

Isaacson, Jeffry S., and Massimo Scanziani. 2011. “How Inhibition Shapes Cortical Activity.” *Neuron* 72 (2): 231–43. doi:10.1016/j.neuron.2011.09.027.

Jiang, Xiaolong, Shan Shen, Cathryn R. Cadwell, Philipp Berens, Fabian Sinz, Alexander S. Ecker, Saumil Patel, and Andreas S. Tolias. 2015. “Principles of Connectivity among Morphologically Defined Cell Types in Adult Neocortex.” *Science* 350 (6264): aac9462. doi:10.1126/science.aac9462.

Johnson, D., K. Illig, M. Behan, and L. Haberly. 2000. “New Features of Connectivity in Piriform Cortex Visualized by Intracellular Injection of Pyramidal Cells Suggest That ‘primary’ olfactory Cortex Functions Like ‘association’ cortex in Other Sensory Systems.” *The Journal of Neuroscience : The Official Journal of the Society for Neuroscience* 20 (18): 6974–82.

Kanter, E. D., A. Kapur, and L. B. Haberly. 1996. “A Dendritic GABAA-Mediated IPSP Regulates Facilitation of NMDA-Mediated Responses to Burst Stimulation of Afferent Fibers in Piriform Cortex.” *J Neurosci* 16 (1): 307–12.

Kanter, E., and L. Haberly. 1993. “Associative Long-Term Potentiation in Piriform Cortex Slices Requires GABAA Blockade.” *The Journal of Neuroscience : The Official Journal of the Society for Neuroscience* 13 (6): 2477–82.

Kapur, A., R. A. Pearce, W. W. Lytton, and L. B. Haberly. 1997. “GABAA-Mediated IPSCs in Piriform Cortex Have Fast and Slow Components with Different Properties and Locations on Pyramidal Cells.” *J Neurophysiol* 78 (5): 2531–45.

Karnani, Mahesh M., Jesse Jackson, Inbal Ayzenshtat, Azadeh Hamzehei Sichani, Kasra Manoocheri, Samuel Kim, and Rafael Yuste. 2016. “Opening Holes in the Blanket of Inhibition: Localized Lateral Disinhibition by VIP Interneurons.” *Journal of Neuroscience* 36 (12): 3471–80. doi:10.1523/JNEUROSCI.3646-15.2016.

Kawaguchi, Y., and Y. Kubota. 1996. “Physiological and Morphological Identification of Somatostatin- or Vasoactive Intestinal Polypeptide-Containing Cells among GABAergic Cell Subtypes in Rat Frontal Cortex.” *Journal of Neuroscience* 16 (8): 2701–15.

Kawaguchi, Y, and Y Kubota. 1997. “GABAergic Cell Subtypes and Their Synaptic Connections in Rat Frontal Cortex.” *Cereb Cortex* 7 (6): 476–86.

Kay, Rachel B., and Peter C. Brunjes. 2014. “Diversity among Principal and GABAergic Neurons of the Anterior Olfactory Nucleus.” *Frontiers in Cellular Neuroscience* 8 (April). doi:10.3389/fncel.2014.00111.

Kesner, Raymond P., and Paul E. Gilbert. 2007. “The Role of the Agranular Insular Cortex in Anticipation of Reward Contrast.” *Neurobiology of Learning and Memory* 88 (1): 82–86. doi:10.1016/j.nlm.2007.02.002.

Ketchum, K. L., and L. B. Haberly. 1993. “Membrane Currents Evoked by Afferent Fiber Stimulation in Rat Piriform Cortex. II. Analysis with a System Model.” *J Neurophysiol* 69 (1): 261–81.

Kleinfeld, David, Martin Deschênes, and Nachum Ulanovsky. 2016. “Whisking, Sniffing, and the Hippocampal θ-Rhythm: A Tale of Two Oscillators.” *PLOS Biology* 14 (2): e1002385. doi:10.1371/journal.pbio.1002385.

Klinkenberg, Inge, Anke Sambeth, and Arjan Blokland. 2011. “Acetylcholine and Attention.” *Behavioural Brain Research*, The cholinergic system and brain function, 221 (2): 430–42. doi:10.1016/j.bbr.2010.11.033.

Kubota, Y., and Y. Kawaguchi. 1994. “Three Classes of GABAergic Interneurons in Neocortex and Neostriatum.” *The Japanese Journal of Physiology* 44 Suppl 2: S145-148.

Kubota, Yoshiyuki. 2014. “Untangling GABAergic Wiring in the Cortical Microcircuit.” *Current Opinion in Neurobiology*, SI: Inhibition: Synapses, Neurons and Circuits, 26 (June): 7–14. doi:10.1016/j.conb.2013.10.003.

Kubota, Yoshiyuki, and Yasuo Kawaguchi. 2000. “Dependence of GABAergic Synaptic Areas on the Interneuron Type and Target Size.” *Journal of Neuroscience* 20 (1): 375–86.

Kubota, Yoshiyuki, Naoki Shigematsu, Fuyuki Karube, Akio Sekigawa, Satoko Kato, Noboru Yamaguchi, Yasuharu Hirai, Mieko Morishima, and Yasuo Kawaguchi. 2011. “Selective Coexpression of Multiple Chemical Markers Defines Discrete Populations of Neocortical GABAergic Neurons.” *Cerebral Cortex* 21 (8): 1803–17. doi:10.1093/cercor/bhq252.

Kuhlman, Sandra J., and Z. Josh Huang. 2008. “High-Resolution Labeling and Functional Manipulation of Specific Neuron Types in Mouse Brain by Cre-Activated Viral Gene Expression.” *PLOS ONE* 3 (4): e2005. doi:10.1371/journal.pone.0002005.

Large, Adam M., Nicholas A. Kunz, Samantha L. Mielo, and Anne-Marie M. Oswald. 2016. “Inhibition by Somatostatin Interneurons in Olfactory Cortex.” *Frontiers in Neural Circuits* 10. doi:10.3389/fncir.2016.00062.

Large, Adam M., Nathan W. Vogler, Samantha Mielo, and Anne-Marie M. Oswald. 2016. “Balanced Feedforward Inhibition and Dominant Recurrent Inhibition in Olfactory Cortex.” *Proceedings of the National Academy of Sciences of the United States of America* 113 (8): 2276–81.

Lee, Seung-Hee, Alex C. Kwan, Siyu Zhang, Victoria Phoumthipphavong, John G. Flannery, Sotiris C. Masmanidis, Hiroki Taniguchi, et al. 2012. “Activation of Specific Interneurons Improves V1 Feature Selectivity and Visual Perception.” *Nature* 488 (7411): 379–83. doi:10.1038/nature11312.

Lee, Soohyun, Illya Kruglikov, Z. Josh Huang, Gord Fishell, and Bernardo Rudy. 2013. “A Disinhibitory Circuit Mediates Motor Integration in the Somatosensory Cortex.” *Nat Neurosci* 16 (11): 1662–70.

Letzkus, Johannes J., Steffen B. E. Wolff, and Andreas Lüthi. 2015. “Disinhibition, a Circuit Mechanism for Associative Learning and Memory.” *Neuron* 88 (2): 264–76. doi:10.1016/j.neuron.2015.09.024.

Leung, L. Stan, and Pascal Peloquin. 2006. “GABAB Receptors Inhibit Backpropagating Dendritic Spikes in Hippocampal CA1 Pyramidal Cells in Vivo.” *Hippocampus* 16 (4): 388–407. doi:10.1002/hipo.20168.

Linster, Christiane, and Thomas Cleland. 2003. “Central Olfactory Structures.” In *Handbook of Olfaction and Gustation*, edited by Richard Doty. CRC Press. doi:10.1201/9780203911457.ch8.

Litwin-Kumar, Ashok, and Brent Doiron. 2012. “Slow Dynamics and High Variability in Balanced Cortical Networks with Clustered Connections.” *Nature Neuroscience* 15 (11): 1498–1505. doi:10.1038/nn.3220.

Litwin-Kumar, Ashok, Anne-Marie M. Oswald, Nathaniel N. Urban, and Brent Doiron. 2011. “Balanced Synaptic Input Shapes the Correlation between Neural Spike Trains.” *PLOS Computational Biology* 7 (12): e1002305. doi:10.1371/journal.pcbi.1002305.

Luna, V. M., and D. L. Pettit. 2010. “Asymmetric Rostro-Caudal Inhibition in the Primary Olfactory Cortex.” *Nat Neurosci* 13 (5): 533–35.

Luna, V. M., and N. E. Schoppa. 2008. “GABAergic Circuits Control Input-Spike Coupling in the Piriform Cortex.” *J Neurosci* 28 (35): 8851–59.

Luskin, Marla B., and Joseph L. Price. 1982. “The Distribution of Axon Collaterals from the Olfactory Bulb and the Nucleus of the Horizontal Limb of the Diagonal Band to the Olfactory Cortex, Demonstrated by Double Retrograde Labeling Techniques.” *The Journal of Comparative Neurology* 209 (3): 249–63. doi:10.1002/cne.902090304.

Ma, Limei, Qiang Qiu, Stephen Gradwohl, Aaron Scott, Elden Q. Yu, Richard Alexander, Winfried Wiegraebe, and C. Ron Yu. 2012. “Distributed Representation of Chemical Features and Tunotopic Organization of Glomeruli in the Mouse Olfactory Bulb.” *Proceedings of the National Academy of Sciences* 109 (14): 5481–86. doi:10.1073/pnas.1117491109.

Ma, Yunyong, Hang Hu, Albert S. Berrebi, Peter H. Mathers, and Ariel Agmon. 2006. “Distinct Subtypes of Somatostatin-Containing Neocortical Interneurons Revealed in Transgenic Mice.” *The Journal of Neuroscience : The Official Journal of the Society for Neuroscience* 26 (19): 5069–82. doi:10.1523/JNEUROSCI.0661-06.2006.

Madisen, L., T. Mao, H. Koch, J. M. Zhuo, A. Berenyi, S. Fujisawa, Y. W. Hsu, et al. 2012. “A Toolbox of Cre-Dependent Optogenetic Transgenic Mice for Light-Induced Activation and Silencing.” *Nat Neurosci* 15 (5): 793–802.

Markram, Henry, Maria Toledo-Rodriguez, Yun Wang, Anirudh Gupta, Gilad Silberberg, and Caizhi Wu. 2004. “Interneurons of the Neocortical Inhibitory System.” *Nature Reviews Neuroscience* 5 (10): 793–807. doi:10.1038/nrn1519.

Marlin, Joseph J., and Adam G. Carter. 2014. “GABA-A Receptor Inhibition of Local Calcium Signaling in Spines and Dendrites.” *Journal of Neuroscience* 34 (48): 15898–911. doi:10.1523/JNEUROSCI.0869-13.2014.

McCollum, Jonn, John Larson, Tim Otto, Frank Schottler, Richard Granger, and Gary Lynch. 1991. “Short-Latency Single Unit Processing in Olfactory Cortex.” *Journal of Cognitive Neuroscience* 3 (3): 293–99. doi:10.1162/jocn.1991.3.3.293.

McGarry, Laura M., Adam M. Packer, Elodie Fino, Volodymyr Nikolenko, Tanya Sippy, and Rafael Yuste. 2010. “Quantitative Classification of Somatostatin-Positive Neocortical Interneurons Identifies Three Interneuron Subtypes.” *Frontiers in Neural Circuits* 4 (May). doi:10.3389/fncir.2010.00012.

Merzenich, Michael M., Jon H. Kaas, and G. Linn Roth. 1976. “Auditory Cortex in the Grey Squirrel: Tonotopic Organization and Architectonic Fields.” *The Journal of Comparative Neurology* 166 (4): 387–401. doi:10.1002/cne.901660402.

Miles, Richard, Katalin Tóth, Attila I. Gulyás, Norbert Hájos, and Tamas F. Freund. 1996. “Differences between Somatic and Dendritic Inhibition in the Hippocampus.” *Neuron* 16 (4): 815–23.

Miura, K., Z. F. Mainen, and N. Uchida. 2012. “Odor Representations in Olfactory Cortex: Distributed Rate Coding and Decorrelated Population Activity.” *Neuron* 74 (6): 1087–98.

Mombaerts, Peter, Fan Wang, Catherine Dulac, Steve K. Chao, Adriana Nemes, Monica Mendelsohn, James Edmondson, and Richard Axel. 1996. “Visualizing an Olfactory Sensory Map.” *Cell* 87 (4): 675–86. doi:10.1016/S0092-8674(00)81387-2.

Muñoz, William, Robin Tremblay, Daniel Levenstein, and Bernardo Rudy. 2017. “Layer-Specific Modulation of Neocortical Dendritic Inhibition during Active Wakefulness.” *Science* 355 (6328): 954–59. doi:10.1126/science.aag2599.

Murphy, Brendan K., and Kenneth D. Miller. 2009. “Balanced Amplification: A New Mechanism of Selective Amplification of Neural Activity Patterns.” *Neuron* 61 (4): 635–48. doi:10.1016/j.neuron.2009.02.005.

Nassar, Mérie, Jean Simonnet, Roxanne Lofredi, Ivan Cohen, Etienne Savary, Yuchio Yanagawa, Richard Miles, and Desdemona Fricker. 2015. “Diversity and Overlap of Parvalbumin and Somatostatin Expressing Interneurons in Mouse Presubiculum.” *Frontiers in Neural Circuits* 9. doi:10.3389/fncir.2015.00020.

Neske, Garrett T., Saundra L. Patrick, and Barry W. Connors. 2015. “Contributions of Diverse Excitatory and Inhibitory Neurons to Recurrent Network Activity in Cerebral Cortex.” *Journal of Neuroscience* 35 (3): 1089–1105. doi:10.1523/JNEUROSCI.2279-14.2015.

Neville, Kevin R., and Lewis B. Haberly. 2004. “Olfactory Cortex.” In *The Synaptic Organization of the Brain*, edited by Gordon M. Shepherd, 415–54. Oxford University Press. doi:10.1093/acprof:oso/9780195159561.003.0010.

Neville KR, and Haberly L. 2004. “Olfactory Cortex.” In *The Synaptic Organization of the Brain*, 415–54. New York: Oxford University Press.

Nowak, Lionel G., Rony Azouz, Maria V. Sanchez-Vives, Charles M. Gray, and David A. McCormick. 2003. “Electrophysiological Classes of Cat Primary Visual Cortical Neurons In Vivo as Revealed by Quantitative Analyses.” *Journal of Neurophysiology* 89 (3): 1541–66. doi:10.1152/jn.00580.2002.

Oliva, Anthony A., Minghui Jiang, Trang Lam, Karen L. Smith, and John W. Swann. 2000. “Novel Hippocampal Interneuronal Subtypes Identified Using Transgenic Mice That Express Green Fluorescent Protein in GABAergic Interneurons.” *Journal of Neuroscience* 20 (9): 3354–68.

Olshausen, Bruno A, and David J Field. 2004. “Sparse Coding of Sensory Inputs.” *Current Opinion in Neurobiology* 14 (4): 481–87. doi:10.1016/j.conb.2004.07.007.

Oswald, Anne-Marie M., and Alex D. Reyes. 2011. “Development of Inhibitory Timescales in Auditory Cortex.” *Cerebral Cortex (New York, NY)* 21 (6): 1351–61. doi:10.1093/cercor/bhq214.

Oswald, Anne-Marie M., and Nathaniel N. Urban. 2012. “Interactions between Behaviorally Relevant Rhythms and Synaptic Plasticity Alter Coding in the Piriform Cortex.” *The Journal of Neuroscience* 32 (18): 6092–6104.

Ozeki, Hirofumi, Ian M. Finn, Evan S. Schaffer, Kenneth D. Miller, and David Ferster. 2009. “Inhibitory Stabilization of the Cortical Network Underlies Visual Surround Suppression.” *Neuron* 62 (4): 578–92. doi:10.1016/j.neuron.2009.03.028.

Padmanabhan, Krishnan, Fumitaka Osakada, Anna Tarabrina, Erin Kizer, Edward M. Callaway, Fred H. Gage, and Terrence J. Sejnowski. 2016. “Diverse Representations of Olfactory Information in Centrifugal Feedback Projections.” *Journal of Neuroscience* 36 (28): 7535–45. doi:10.1523/JNEUROSCI.3358-15.2016.

Pakan, Janelle MP, Scott C Lowe, Evelyn Dylda, Sander W Keemink, Stephen P Currie, Christopher A Coutts, and Nathalie L Rochefort. 2017. “Behavioral-State Modulation of Inhibition Is Context-Dependent and Cell Type Specific in Mouse Visual Cortex.” *eLife* 5. Accessed March 27. doi:10.7554/eLife.14985.

Patil, M. M., C. Linster, E. Lubenov, and M. E. Hasselmo. 1998. “Cholinergic Agonist Carbachol Enables Associative Long-Term Potentiation in Piriform Cortex Slices.” *J Neurophysiol* 80 (5): 2467–74.

Pehlevan, Cengiz, and Haim Sompolinsky. 2014. “Selectivity and Sparseness in Randomly Connected Balanced Networks.” *PLOS ONE* 9 (2): e89992. doi:10.1371/journal.pone.0089992.

Pfeffer, C. K., M. Xue, M. He, Z. J. Huang, and M. Scanziani. 2013. “Inhibition of Inhibition in Visual Cortex: The Logic of Connections between Molecularly Distinct Interneurons.” *Nat Neurosci* 16 (8): 1068–76.

Pi, H. J., B. Hangya, D. Kvitsiani, J. I. Sanders, Z. J. Huang, and A. Kepecs. 2013. “Cortical Interneurons That Specialize in Disinhibitory Control.” *Nature* 503 (7477): 521–24.

Poo, C., and J. S. Isaacson. 2009. “Odor Representations in Olfactory Cortex: ‘sparse’ coding, Global Inhibition, and Oscillations.” *Neuron* 62 (6): 850–61.

———. 2011. “A Major Role for Intracortical Circuits in the Strength and Tuning of Odor-Evoked Excitation in Olfactory Cortex.” *Neuron* 72 (1): 41–48.

Poorthuis, Rogier B, Leona Enke, and Johannes J Letzkus. 2014. “Cholinergic Circuit Modulation through Differential Recruitment of Neocortical Interneuron Types during Behaviour.” *The Journal of Physiology* 592 (Pt 19): 4155–64. doi:10.1113/jphysiol.2014.273862.

Porter, James T., Bruno Cauli, Keisuke Tsuzuki, Bertrand Lambolez, Jean Rossier, and Etienne Audinat. 1999. “Selective Excitation of Subtypes of Neocortical Interneurons by Nicotinic Receptors.” *The Journal of Neuroscience* 19 (13): 5228–35.

Price, Joseph L. 1973. “An Autoradiographic Study of Complementary Laminar Patterns of Termination of Afferent Fibers to the Olfactory Cortex.” *The Journal of Comparative Neurology* 150 (1): 87–108. doi:10.1002/cne.901500105.

Ranade, Sachin, Balázs Hangya, and Adam Kepecs. 2013. “Multiple Modes of Phase Locking between Sniffing and Whisking during Active Exploration.” *The Journal of Neuroscience : The Official Journal of the Society for Neuroscience* 33 (19): 8250–56. doi:10.1523/JNEUROSCI.3874-12.2013.

Rennaker, Robert L., Chien-Fu F. Chen, Andrea M. Ruyle, Andrew M. Sloan, and Donald A. Wilson. 2007. “Spatial and Temporal Distribution of Odorant-Evoked Activity in the Piriform Cortex.” *The Journal of Neuroscience : The Official Journal of the Society for Neuroscience* 27 (7): 1534–42. doi:10.1523/JNEUROSCI.4072-06.2007.

Ressler, Kerry J., Susan L. Sullivan, and Linda B. Buck. 1994. “Information Coding in the Olfactory System: Evidence for a Stereotyped and Highly Organized Epitope Map in the Olfactory Bulb.” *Cell* 79 (7): 1245–55. doi:10.1016/0092-8674(94)90015-9.

Rubin, Daniel B., Stephen D. Van Hooser, and Kenneth D. Miller. 2015. “The Stabilized Supralinear Network: A Unifying Circuit Motif Underlying Multi-Input Integration in Sensory Cortex.” *Neuron* 85 (2): 402–17. doi:10.1016/j.neuron.2014.12.026.

Rudy, Bernardo, Gordon Fishell, SooHyun Lee, and Jens Hjerling-Leffler. 2011. “Three Groups of Interneurons Account for Nearly 100% of Neocortical GABAergic Neurons.” *Developmental Neurobiology* 71 (1): 45–61. doi:10.1002/dneu.20853.

Schacter, D. L. 2001. *Forgotten Ideas, Neglected Pioneers: Richard Semon and the Story of Memory*. Philadelphia: Psychology Press. http://www.amazon.com/Forgotten-Ideas-Neglected-Pioneers-Richard/dp/184169052X/ref=sr_1_1?s=books&ie=UTF8&qid=1313936664&sr=1-1.

Schummers, James, Jitendra Sharma, and Mriganka Sur. 2005. “Bottom-up and Top-down Dynamics in Visual Cortex.” In , edited by BT - Progress in Brain Research, 149:65–81. Cortical Function: A View from the Thalamus. Elsevier. doi:10.1016/S0079-6123(05)49006-8.

Scott, J. W. 1981. “Electrophysiological Identification of Mitral and Tufted Cells and Distributions of Their Axons in Olfactory System of the Rat.” *Journal of Neurophysiology* 46 (5): 918–31.

Semon, Richard Wolfgang. 1921. *The Mneme*. G. Allen & Unwin Limited.

Seybold, Bryan A., Elizabeth A. K. Phillips, Christoph E. Schreiner, and Andrea R. Hasenstaub. 2015. “Inhibitory Actions Unified by Network Integration.” *Neuron* 87 (6): 1181–92. doi:10.1016/j.neuron.2015.09.013.

Shakhawat, A. M., and A. Gheidi. 2014. “Visualizing the Engram: Learning Stabilizes Odor Representations in the Olfactory Network” 34 (46): 15394–401.

Shakhawat, A. M., C. W. Harley, and Q. Yuan. 2014. “Arc Visualization of Odor Objects Reveals Experience-Dependent Ensemble Sharpening, Separation, and Merging in Anterior Piriform Cortex in Adult Rat.” *J Neurosci* 34 (31): 10206–10.

Shepherd, Gordon M., ed. 2004. *The Synaptic Organization of the Brain*. Oxford University Press. doi:10.1093/acprof:oso/9780195159561.001.1.

Sheridan, D. C., A. R. Hughes, F. Erdélyi, G. Szabó, S. T. Hentges, and N. E. Schoppa. 2014. "Matching of Feedback Inhibition with Excitation Ensures Fidelity of Information Flow in the Anterior Piriform Cortex." *Neuroscience* 275 (September): 519–30. doi:10.1016/j.neuroscience.2014.06.033.

Sosulski, Dara L., Maria Lissitsyna Bloom, Tyler Cutforth, Richard Axel, and Sandeep Robert Datta. 2011. "Distinct Representations of Olfactory Information in Different Cortical Centres." *Nature* 472 (7342): 213–16. doi:10.1038/nature09868.

Soucy, Edward R., Dinu F. Albeanu, Antoniu L. Fantana, Venkatesh N. Murthy, and Markus Meister. 2009. "Precision and Diversity in an Odor Map on the Olfactory Bulb." *Nature Neuroscience* 12 (2): 210–20. doi:10.1038/nn.2262.

Stettler, Dan D., and Richard Axel. 2009. "Representations of Odor in the Piriform Cortex." *Neuron* 63 (6): 854–64. doi:10.1016/j.neuron.2009.09.005.

Stokes, C. C., and J. S. Isaacson. 2010. "From Dendrite to Soma: Dynamic Routing of Inhibition by Complementary Interneuron Microcircuits in Olfactory Cortex." *Neuron* 67 (3): 452–65.

Stokes, Caleb C. A., Corinne M. Teeter, and Jeffry S. Isaacson. 2014. "Single Dendrite-Targeting Interneurons Generate Branch-Specific Inhibition." *Frontiers in Neural Circuits* 8 (November). doi:10.3389/fncir.2014.00139.

Stryker, Michael P. 2014. "A Neural Circuit That Controls Cortical State, Plasticity, and the Gain of Sensory Responses in Mouse." *Cold Spring Harbor Symposia on Quantitative Biology* 79 (January): 1–9. doi:10.1101/sqb.2014.79.024927.

Sturgill, James F., and Jeffry S. Isaacson. 2015. "Somatostatin Cells Regulate Sensory Response Fidelity via Subtractive Inhibition in Olfactory Cortex." *Nature Neuroscience* 18 (4): 531–35. doi:10.1038/nn.3971.

Sugai, T., T. Miyazawa, M. Fukuda, H. Yoshimura, and N. Onoda. 2005. "Odor-Concentration Coding in the Guinea-Pig Piriform Cortex." *Neuroscience* 130 (3): 769–81.

Suzuki, N., and J. M. Bekkers. 2006. "Neural Coding by Two Classes of Principal Cells in the Mouse Piriform Cortex." *J Neurosci* 26 (46): 11938–47.

———. 2010a. "Inhibitory Neurons in the Anterior Piriform Cortex of the Mouse: Classification Using Molecular Markers." *J Comp Neurol* 518 (10): 1670–87.

———. 2010b. "Distinctive Classes of GABAergic Interneurons Provide Layer-Specific Phasic Inhibition in the Anterior Piriform Cortex." *Cereb Cortex* 20 (12): 2971–84.

———. 2011. "Two Layers of Synaptic Processing by Principal Neurons in Piriform Cortex." *J Neurosci* 31 (6): 2156–66.

———. 2012. “Microcircuits Mediating Feedforward and Feedback Synaptic Inhibition in the Piriform Cortex.” *J Neurosci* 32 (3): 919–31.

Swadlow, Harvey A. 2003. “Fast-Spike Interneurons and Feedforward Inhibition in Awake Sensory Neocortex.” *Cerebral Cortex* 13 (1): 25–32. doi:10.1093/cercor/13.1.25.

Taniguchi, H., M. He, P. Wu, S. Kim, R. Paik, K. Sugino, D. Kvitsiani, et al. 2011. “A Resource of Cre Driver Lines for Genetic Targeting of GABAergic Neurons in Cerebral Cortex.” *Neuron* 71 (6): 995–1013.

Tootell, R. B., M. S. Silverman, E. Switkes, and RL De Valois. 1982. “Deoxyglucose Analysis of Retinotopic Organization in Primate Striate Cortex.” *Science* 218 (4575): 902–4. doi:10.1126/science.7134981.

Urban-Ciecko, Joanna, and Alison L. Barth. 2016. “Somatostatin-Expressing Neurons in Cortical Networks.” *Nature Reviews Neuroscience* 17 (7): 401–9. doi:10.1038/nrn.2016.53.

Urban-Ciecko, Joanna, Erika E. Fanselow, and Alison L. Barth. 2015. “Neocortical Somatostatin Neurons Reversibly Silence Excitatory Transmission via GABAb Receptors.” *Current Biology : CB* 25 (6): 722–31. doi:10.1016/j.cub.2015.01.035.

Valley, Matthew T., and Stuart Firestein. 2008. “A Lateral Look at Olfactory Bulb Lateral Inhibition.” *Neuron* 59 (5): 682–84. doi:10.1016/j.neuron.2008.08.018.

Vassar, Robert, Steve K. Chao, Raquel Sitcheran, Jennifer M. Nun˜ez, Leslie B. Vosshall, and Richard Axel. 1994. “Topographic Organization of Sensory Projections to the Olfactory Bulb.” *Cell* 79 (6): 981–91. doi:10.1016/0092-8674(94)90029-9.

Wessa, P, URL Education, DA Wilson, and RM Sullivan. 2011. *Hierarchical Clustering (v1.0.3) in Free Statistics Software (v1.1.). Office for Research Development and Http://Www.wessa.net/Rwasp_hierarchicalclustering.wasp/. and Cortical Processing of Odor Objects*. Vol. 72.

Wiegand, Hauke F., Prateep Beed, Michael HK Bendels, Christian Leibold, Dietmar Schmitz, and Friedrich W. Johenning. 2011. “Complementary Sensory and Associative Microcircuitry in Primary Olfactory Cortex.” *The Journal of Neuroscience* 31 (34): 12149–58.

Wilson, D. A. 2001. “Scopolamine Enhances Generalization between Odor Representations in Rat Olfactory Cortex.” *Learn Mem* 8 (5): 279–85.

Wilson, D. A., and M. Leon. 1987. “Evidence of Lateral Synaptic Interactions in Olfactory Bulb Output Cell Responses to Odors.” *Brain Research* 417 (1): 175–80. doi:10.1016/0006-8993(87)90196-X.

Wilson, Donald A. 2001. “Receptive Fields in the Rat Piriform Cortex.” *Chemical Senses* 26 (5): 577–84. doi:10.1093/chemse/26.5.577.

———. 2009. “Pattern Separation and Completion in Olfaction.” *Annals of the New York Academy of Sciences* 1170 (July): 306–12. doi:10.1111/j.1749-6632.2009.04017.x.

Wilson, Donald A., Max L. Fletcher, and Regina M. Sullivan. 2004. “Acetylcholine and Olfactory Perceptual Learning.” *Learning & Memory* 11 (1): 28–34. doi:10.1101/lm.66404.

Wilson, Donald A., and Robert L. Rennaker. 2010. “Cortical Activity Evoked by Odors.” In *The Neurobiology of Olfaction*, edited by Anna Menini. Frontiers in Neuroscience. Boca Raton (FL): CRC Press/Taylor & Francis. http://www.ncbi.nlm.nih.gov/books/NBK55970/.

Wilson, Donald A., and Regina M. Sullivan. 2011. “Cortical Processing of Odor Objects.” *Neuron* 72 (4): 506–19. doi:10.1016/j.neuron.2011.10.027.

Wilson, Nathan R., Caroline A. Runyan, Forea L. Wang, and Mriganka Sur. 2012. “Division and Subtraction by Distinct Cortical Inhibitory Networks in Vivo.” *Nature* 488 (7411): 343–48.

Wingen, Marleen, Kim P.C. Kuypers, Vincent van de Ven, Elia Formisano, and Johannes G. Ramaekers. 2008. “Sustained Attention and Serotonin: A Pharmaco-fMRI Study.” *Human Psychopharmacology: Clinical and Experimental* 23 (3): 221–30. doi:10.1002/hup.923.

Wixted, John T., Larry R. Squire, Yoonhee Jang, Megan H. Papesh, Stephen D. Goldinger, Joel R. Kuhn, Kris A. Smith, David M. Treiman, and Peter N. Steinmetz. 2014. “Sparse and Distributed Coding of Episodic Memory in Neurons of the Human Hippocampus.” *Proceedings of the National Academy of Sciences* 111 (26): 9621–26. doi:10.1073/pnas.1408365111.

Xu, Han, Hyo-Young Jeong, Robin Tremblay, and Bernardo Rudy. 2013. “Neocortical Somatostatin-Expressing GABAergic Interneurons Disinhibit the Thalamorecipient Layer 4.” *Neuron* 77 (1): 155–67. doi:10.1016/j.neuron.2012.11.004.

Yang, Weiguo, Yarimar Carrasquillo, Bryan M. Hooks, Jeanne M. Nerbonne, and Andreas Burkhalter. 2013. “Distinct Balance of Excitation and Inhibition in an Interareal Feedforward and Feedback Circuit of Mouse Visual Cortex.” *Journal of Neuroscience* 33 (44): 17373–84. doi:10.1523/JNEUROSCI.2515-13.2013.

York, George K., and David A. Steinberg. 2011. “Hughlings Jackson’s Neurological Ideas.” *Brain* 134 (10): 3106–13. doi:10.1093/brain/awr219.

Young, Andrew, and Qian-Quan Sun. 2009. “GABAergic Inhibitory Interneurons in the Posterior Piriform Cortex of the GAD67–GFP Mouse.” *Cerebral Cortex* 19 (12): 3011–29. doi:10.1093/cercor/bhp072.

Zhan, Cheng, and Minmin Luo. 2010. “Diverse Patterns of Odor Representation by Neurons in the Anterior Piriform Cortex of Awake Mice.” *Journal of Neuroscience* 30 (49): 16662–72. doi:10.1523/JNEUROSCI.4400-10.2010.

Zhao, S., J. T. Ting, H. E. Atallah, L. Qiu, J. Tan, B. Gloss, G. J. Augustine, et al. 2011. “Cell Type-Specific Channelrhodopsin-2 Transgenic Mice for Optogenetic Dissection of Neural Circuitry Function.” *Nat Methods* 8 (9): 745–52.

Zhao, Yan, Zizhen Zhang, Xiuping Liu, Colin Xiong, Zhongju Xiao, and Jun Yan. 2015. “Imbalance of Excitation and Inhibition at Threshold Level in the Auditory Cortex.” *Frontiers in Neural Circuits* 9 (March). doi:10.3389/fncir.2015.00011.

Zhu, Hu, Dipendra K. Aryal, Reid H.J. Olsen, Daniel J. Urban, Amanda Swearingen, Stacy Forbes, Bryan L. Roth, and Ute Hochgeschwender. 2016. “Cre-Dependent DREADD (Designer Receptors Exclusively Activated by Designer Drugs) Mice.” *Genesis* 54 (8): 439–46. doi:10.1002/dvg.22949.